RUPRECHT-KARLS-UNIVERSITÄT HEIDELBERG

Damir Raßloff

Installation, Commissioning and Calibration of the ATLAS Level-1 Calorimeter Trigger in Run 3

Dissertation

HD-KIP-23-96

KIRCHHOFF-INSTITUT FÜR PHYSIK

Dissertation

submitted to the

Combined Faculty of Mathematics, Engineering and

Natural Sciences

of Heidelberg University, Germany

for the degree of

Doctor of Natural Sciences

Put forward by

Damir Fabrice Raßloff

born in: Heilbronn

Oral examination: December 13th, 2023

Installation, Commissioning and Calibration of the ATLAS Level-1 Calorimeter Trigger in Run 3

Referees: Prof. Dr. Hans-Christian Schultz-Coulon
Prof. Dr. Loredana Gastaldo

Zusammenfassung

Als Vorbereitung für Run 3, wenn der LHC bei höheren Energien und instantaner Luminosität betrieben wird, erfuhr der hardwarebasierte ATLAS Level-1 Kalorimeter Trigger eine Reihe von Verbesserungen.
Darunter sind drei neue Identifikationssysteme, die digitalisierte Daten mit höherer Granularität aus dem neuen Phase-1 LAr-Kalorimetersystem in verbesserten Algorithmen verwenden, um Ereignisse mit physikalischen Objekten von Interesse zu identifizieren. Diese Identifikationssysteme erhalten weiterhin vom alten Run 2 Legacy Level-1 Kalorimeter Trigger System über dem neu eingeführten TREX Modul Daten vom Tile Kalorimeter.
Unter anderem führte dieser Einschnitt in das Legacy System, welches während der andauernden Inbetriebnahme des neuen L1Calo Systems am Anfang des Run 3 die frühe Datennahme übernommen hat, dazu, dass dieses neu kalibriert und in Betrieb genommen werden musste. In dieser Arbeit wird ein allgemeiner Überblick über die Zeit von der Entwicklung sowie Installation der neuen Level-1 Kalorimeter Trigger Hardware über die erneute Kalibrierung und Inbetriebnahme des Legacy System mit dem neuen TREX Modul bis zu den Studien gegeben, die zum Wechsel des Einzel-Elektron Triggers vom Legacy System zum neuen Run 3 System führten.

Abstract

In preparation for Run 3, when the LHC will operate at higher energies and instantaneous luminosity, the hardware-based ATLAS Level-1 calorimeter trigger underwent a number of improvements. Among them are three new identification systems that use already digitised data with higher granularity from the new Phase-1 LAr calorimeter system in improved algorithms to identify events with physics objects of interest. These identification systems continue to receive data from the Tile calorimeter from the old Run 2 legacy Level-1 calorimeter trigger system via the newly introduced TREX module.
Among other things, this intervention in the legacy system, which took over early data taking during the ongoing commissioning of the new L1Calo system at the start of Run 3, required it to be recalibrated and commissioned. This thesis gives a general overview of the time from the development and installation of the new Level-1 calorimeter trigger hardware, via the recalibration and commissioning of the legacy system with the new TREX module, to the studies that led to the change of the single electron trigger from the legacy system to the new Run 3 system.

Contents

1 Introduction

The Large Hadron Collider (LHC) mostly accelerates and collides protons at high centre-of-mass energies of $\sqrt{s} = 13.6\,\mathrm{TeV}$ and a collision frequency of $40\,\mathrm{MHz}$ within the four interaction points, where the large experiments are positioned.
At one of these points, the general-purpose ATLAS detector is located, which is designed to study a wide range of physics. The ATLAS detector is arranged in an onion-like structure with a variety of different detector technologies around the interaction point, to detect the products resulting from the proton-proton collisions.
The LHC's high event rate of $40\,\mathrm{MHz}$ leads to an amount of data that cannot be handled by the ATLAS detector's storage system, which is why a two-stage trigger system was implemented in the ATLAS experiment to identify events of interest. The first stage of the trigger system is the hardware-based ATLAS Level-1 trigger, which can be divided into a Level-1 calorimeter (L1Calo) and a Level-1 muon trigger and reduces the event rate from $40\,\mathrm{MHz}$ to about $100\,\mathrm{kHz}$.
The L1Calo trigger uses the information from the ATLAS LAr and Tile calorimeters to search for electron, photon, τ and jet candidates. In addition, the system calculates the missing transverse energy $E_{\mathrm{T}}^{\mathrm{miss}}$ and the total transverse energy $E_{\mathrm{T}}^{\mathrm{tot}}$ for the selection of events of interest.
With the higher centre-of-mass energies as well as higher instantaneous luminosity introduced in the ongoing data taking of Run 3, and the resulting harsher data taking conditions, the L1Calo trigger faces the challenge of maintaining its excellent performance of Run 1 and Run 2. For this reason, the L1Calo system underwent an immense upgrade, namely the Phase-1 upgrade, taking advantage of the new LAr calorimeter electronics for Run 3. This implements a forwarding of digitized signals with 10 $\times$ higher granularity to the newly introduced FPGA-based Feature Extractor (FEX) modules of the L1Calo system. The FEXes use the higher granularity information to continue to find interesting events in the harsher environment with new advanced algorithms and excellent performance.
The Tile calorimeter has not received any upgrade for Run 3, so it continues to send analogue signals to the L1Calo system via the legacy L1Calo path. To provide these to the new FEXes, the Tile Rear Extension (TREX) module was introduced as a physical extension of the legacy Run 2 PreProcessor Module (PPM). In addition, the introduction of the TREX allows the legacy Run 2 system to run in parallel with the new on the FEX modules based Phase-1 system. This was exploited to trigger the first data taking period of Run 3

with the legacy system, while still testing and commissioning the Phase-1 system.
This thesis first gives an overview of the LHC and the ATLAS detector in Chapter 2, after which the Trigger and Data Acquisition (TDAQ) system of the ATLAS experiment is explained in Chapter 3 with special regard to the L1Calo trigger. Chapter 4 then introduces the Phase-1 upgrade of the L1Calo system. The next two chapters address the TREX module, with a brief overview of the TREX system in Chapter 5 and a detailed explanation of its monitoring in Chapter 6. Subsequently, Chapter 7 introduces the L1Calo online and offline software. The following Chapter 8 deals with the recalibration and recommissioning of the legacy L1Calo system, continued by the commissioning of the Phase-1 system in Chapter 9. The final Chapter 10, before the conclusion in Chapter 11, is an overview of various eFEX parameter studies.

Author's Contribution

The work presented here as part of the ATLAS experiment and in particular the ATLAS Level-1 calorimeter trigger group benefited greatly from the dedicated work of many different people in developing hardware, firmware, and software. This provided the author with all the support he needed to achieve the goals of his work and gave him access to a range of software, calibrations, and other helpful tools.
The author's first contribution to the ATLAS collaboration was to develop test software and firmware for early versions of the TREX module. The results are not further detailed in the thesis and mainly included configuration firmware for the FPGAs of the TREX module and test software for commissioning the TREX.
With gained experience with the TREX module, the author implemented the TREX online simulation into the existing L1Calo online simulation framework, including the simulation of the real-time path to the new FEX systems and the readout path to the FELIX-SW ROD system.
In parallel, the author was developing the TREX Detector Control System (DCS) backend as a part of the ATLAS DCS. Based on the hardware design and the already implemented DCS of the legacy L1Calo system, a completely fully functional own TREX project running in the ATLAS DCS was created by the author. In addition, as part of the L1Calo DCS team, the author contributed to the foundations, such as a common panel design, for the other Phase-1 systems.
A large part of the author's work consisted of installing and operating the L1Calo system on site at CERN. As part of the L1Calo installation team, the author performed a large number of installations for the Phase-1 system in the electronic caverns of the ATLAS

experiment. This included several infrastructural related installations, such as the cabling of hardware components or the installation of servers, and the contribution to the installation and initial tests of the new TTC system, the FOXes, the TopoFOX, the TREX or also the eFEX modules.
As part of the L1Calo operations team, the author was involved in several system relevant tests for the legacy and Phase-1 system and thus was included in the activities during the milestone weeks, splashes, pilot run, and ramp up of the LHC as an expert especially for the legacy system.
This time was also used for recalibration and recommissioning of the legacy system. The author took the main responsibility for the recalibration of the Tile calorimeter signals. In addition, he was involved in ensuring the functionality of the LAr and Tile calorimeter calibrations after the upgrade of the ATLAS TTC system.
A lot of work of the author was generally invested in preparing the legacy L1Calo system with inputs from both calorimeters as best as possible for the upcoming first data taking, including for example the identification of problematic and noisy trigger towers (TTs), but also the subsequent required technical interventions.
During the recalibration and commissioning of the legacy L1Calo system, the author supported the development of data access tools in the online and offline software for the legacy as well as Phase-1 data.
Having established the data access, the author conducted several analyses throughout the Phase-1 commissioning process, including comparisons between the legacy and Phase-1 systems with input data, TOBs, and trigger efficiencies. Additionally, the author developed analyses focused on noise, triggers, and parameter investigations. The tools created were merged into a software framework by the author and subsequently shared with the L1Calo community for further analyses.

2 The ATLAS Experiment at the Large Hadron Collider

To understand the components of the universe, discover new unknown particles and processes, and observe rare particle interactions, high-energy particles are collided in an experimental environment. For this purpose, the *Large Hadron Collider* (LHC) [1] was built on the grounds of the European Organisation for Nuclear Research (CERN[1]) near Geneva, Switzerland. It is presently the world's most powerful particle accelerator, with the capability to collide two beams of particles at four different interaction points. The LHC will be described in detail in Section 2.1.
On each of the four interaction points of the LHC an experiment is located. One of them is the *A Toroidal LHC Apparatus* (ATLAS) [2] experiment, for which the studies and developments described in this thesis were made. The detector will be highlighted in Section 2.2.

2.1 The Large Hadron Collider

The LHC [1] has been conceived as a circular particle accelerator, featuring a circumference spanning $26.7\,\mathrm{km}$, which is located in an underground tunnel with depths ranging from $45\,\mathrm{m}$ to $170\,\mathrm{m}$. It is constructed to accelerate and collide oppositely travelling beams of protons and heavy ions at high energies.
Radiofrequency cavities take over the task of accelerating the two beams, while several dipole, quadrupole and corrector electromagnets guide the particles around the circular ring and focus them to high-intensity beams in front of the interaction points. The two focused beams collide at the four interactions points of the LHC, while the resulting decay products are detected by the experiments located around them.
Two of the four main experiments at the LHC, ATLAS and the *Compact Muon Solenoid* (CMS) [3], are general-purpose detectors. Both were built to investigate a broad spectrum of physics, with a particular emphasis on probing *proton-proton* (p-p) collisions. The *A Large Ion Collider Experiment* (ALICE) [4], on the other hand, specialises in heavy ion collisions and their properties. The fourth experiment, the *Large Hadron Collider beauty* (LHCb) [5] is a forward spectrometer, which concentrates on bottom quark physics. Figure 2.1 indicates the position of the four experiments at the LHC.

[1] Conseil Européen pour la Recherche Nucléaire

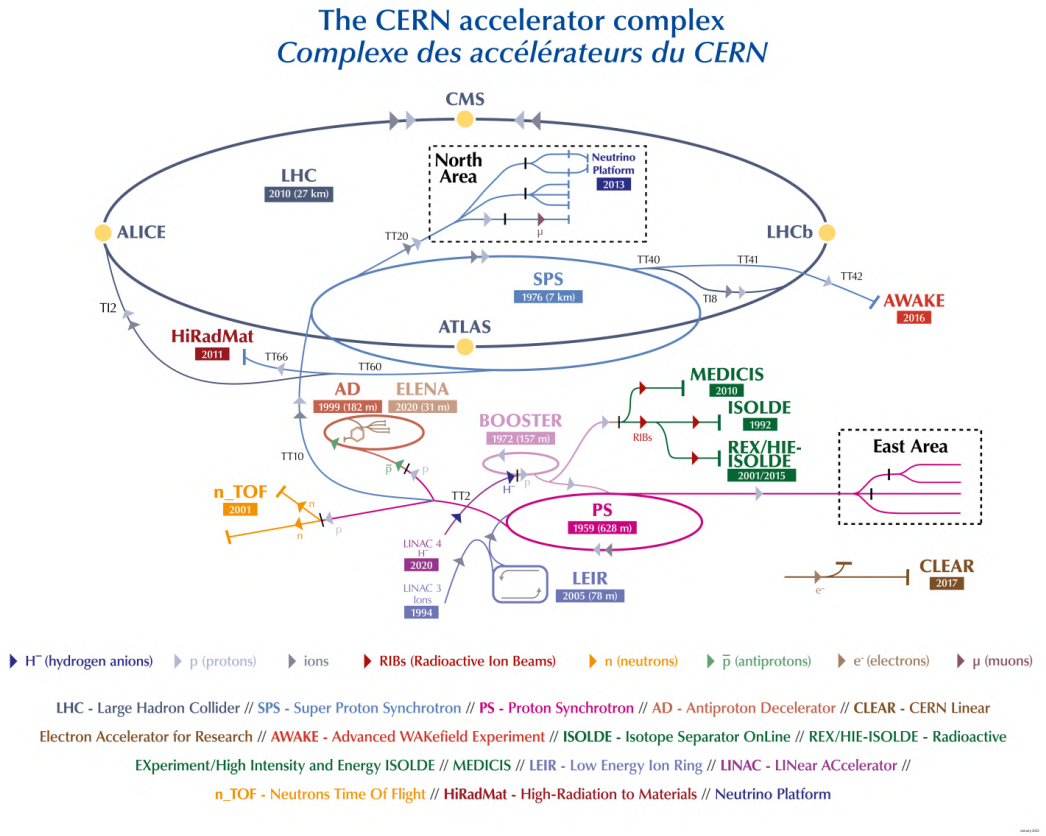

Figure 2.1: The CERN accelerator complex. The sequence of the pre-acceleration process starts with negatively charged hydrogen atoms H^- and the LINAC4 linear accelerator. Inside the following circular accelerators, namely the PSB, the PS and finally, before injection into the LHC, the SPS, the protons get pre-accelerated to an energy of $450\,\mathrm{GeV}$. The injected protons are then collided in the four experiments, ATLAS, CMS, ALICE, and LHCb. Taken from [8].

In addition, the whole CERN accelerator complex is shown, which pre-accelerates the particles on their way to the LHC and ultimately to the collision in the experiments. The starting point for p-p collisions are negatively charged hydrogen atoms H^- that are accelerated to an energy of $160\,\mathrm{MeV}$ in the *Linear Accelerator 4* (LINAC4) [6]. During the injection into the next stage the hydrogen ions are stripped of their two electrons only leaving protons to enter the *Proton Synchrotron Booster* (PSB) [7]. The PSB accelerates the protons to an energy of $2\,\mathrm{GeV}$ and injects them to the next pre-accelerator in the sequence, the *Proton Synchrotron* (PS). The PS increases the energy of the beam to $26\,\mathrm{GeV}$, which leads to the last stage of the complex, the *Super Proton Synchrotron* (SPS). There, the particles are accelerated to an energy of $450\,\mathrm{GeV}$ and then get injected in the available slots of the LHC following the rules of the LHC beam structure.

2.1.1 The LHC Beam Structure

The beams consist of so-called *bunches*, each containing up to 10^{11} protons, which can be filled into 3564 possible bunch slots. To ensure stable as well as secure beam operations and in order to enable ramping up the kicker magnets for the beam dump, the maximum possible amount of filled slots by design is 2808 bunches. The bunches circulate with a revolution frequency of f_{rev}=11.245 kHz around the *orbit* of the LHC. They are separated by $25\,\text{ns}$, which leads to a possible collision every $25\,\text{ns}$ due to a crossing of the two beams, also called *Bunch Crossing* (BC), and a collision frequency of $40.08\,\text{MHz}$. According to the number of possible bunch slots, there are 3564 BCs, each of which is given a unique number, the so-called *BC Identification* (BCID), between 0 and 3563.
In normal data taking, the beam is arranged in a *train*-like structure, which means that filled BCs alternate with empty BCs. The filled parts of the train consist of *paired* BCs, where the bunches of both beams are filled. These parts are separated by *unpaired* or *empty* BCs, where either the bunch of one of the two beams is filled or both are empty. The LHC beam structure determines the luminosity and the pile-up of the LHC [9–11].

2.1.2 Luminosity and Pile-up

A particle accelerator has two main performance parameters. The first is the centre-of-mass energy $\sqrt{s}$, which determines the total collision energy and therefore the energy range of the observed physics processes. The second is the instantaneous luminosity $\mathcal{L}$ [12], which describes the amount of particle collisions per area and time. The instantaneous luminosity for two colliding beams with an equal Gaussian profile is defined as [12]

$$\mathcal{L} = \frac{N_1 N_2 f_{\text{rev}} N_b}{4\pi\sigma_x\sigma_y}, \tag{2.1}$$

with the number of particles N_1 and N_2 in the colliding bunches of each beam, the already mentioned revolution frequency f_{rev}, the number of filled bunches N_b, and the beam widths σ_x and σ_y in x and y direction.
The integrated luminosity $\mathcal{L}_{\text{int}}$ is a measure for the number of collisions in a time span $\mathrm{d}t$ and therefore for the size of a dataset. It can be expressed through

$$\mathcal{L}_{\text{int}} = \int_0^T \mathcal{L}(t')\mathrm{d}t'. \tag{2.2}$$

The integrated luminosity can be used to calculate the number of events N for a certain physics process with a cross section σ:

$$N = \sigma \mathcal{L}_{\text{int}}. \tag{2.3}$$

Therefore, one of the main goals of the LHC is to increase the instantaneous and integrated luminosity in order to obtain huge amounts of statistics for many interesting physics processes.
The pursuit of this goal, however, forces the experiments to tackle the challenge of the so-called *pile-up*. The *in-time pile-up* describes the overlap of events, originating from multiple simultaneously p-p interactions. A measure for the pile-up is the mean number of p-p interactions per BC μ, which can be expressed through [13]

$$\mu = \frac{\mathcal{L}\sigma_{\text{tot}}}{N_b f_{\text{rev}}}, \tag{2.4}$$

with the instantaneous luminosity $\mathcal{L}$, the total p-p cross section σ_{tot}, the number of filled bunches N_b, and the revolution frequency f_{rev}. Additional to this in-time pile-up that originates from collisions of the same BC, the *out-of-time pile-up* exists that originates from collisions from previous BCs and is therefore directly linked to the filling scheme of the LHC orbit.
With the increasing luminosity of the LHC to reach larger datasets, the pile-up developed to one of the main challenges for the experiments, which leads to several upgrade programs for the detectors [10, 11].

2.1.3 LHC Runs and Upgrades

The first data-taking period of the LHC, called *Run 1*, started in 2010 with p-p collisions at a centre-of-mass energy of $\sqrt{s} = 7\,\text{TeV}$, which was increased in 2012 to $8\,\text{TeV}$. Run 1 ended at the end of 2012, with the LHC delivering a total integrated luminosity of $29.24\,\text{fb}^{-1}$ and a peak instantaneous luminosity of $7.7 \times 10^{33}\,\text{cm}^{-2}\,\text{s}^{-1}$ [14].
Between 2013 and 2015 the LHC entered the *Long Shutdown 1* (LS1) to upgrade and maintain the machine. The experiments also took advantage of the downtime and the ATLAS experiment, for instance, carried out the *Phase-0 upgrade* of the detector.
In 2015, *Run 2* started with centre-of-mass energies of $\sqrt{s} = 13\,\text{TeV}$ and lasted till 2018. During this time span, the LHC delivered an integrated luminosity of $160\,\text{fb}^{-1}$ with a peak instantaneous luminosity of $2.05 \times 10^{34}\,\text{cm}^{-2}\,\text{s}^{-1}$ [15], which is more than twice the LHC design luminosity of $1 \times 10^{34}\,\text{cm}^{-2}\,\text{s}^{-1}$.

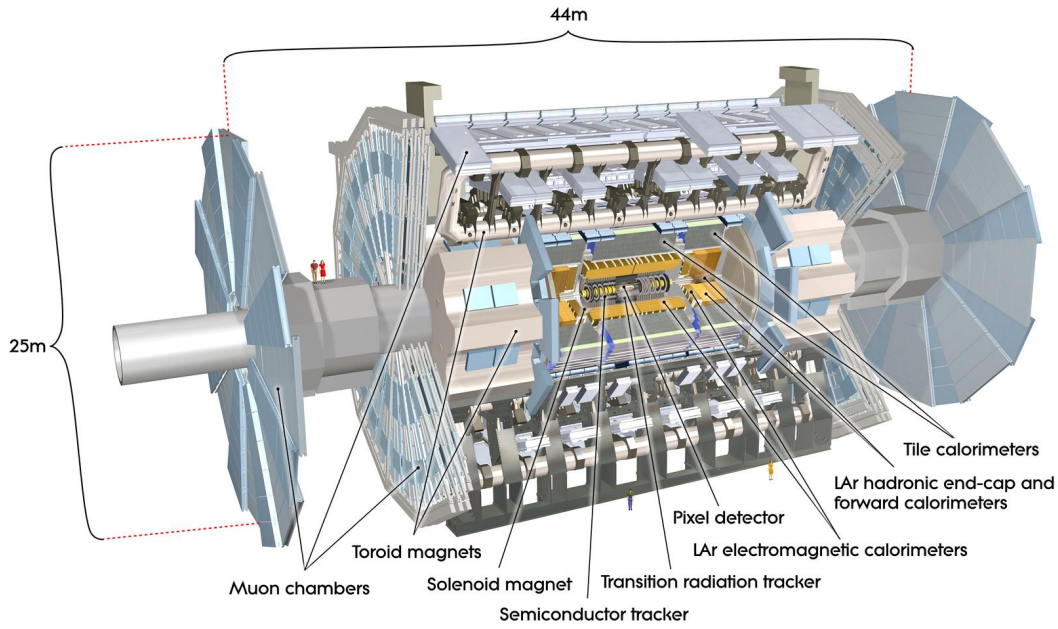

Figure 2.2: Schematic overview of the ATLAS detector. The sub-components from the inside out are the ID, the solenoid, the calorimeters, the toroid magnets and the muon spectrometer. Taken from [16].

Run 2 was followed by the *Long Shutdown 2* (LS2) from 2018 to 2022. The downtime was used for several upgrades on the accelerators and experiments. The ATLAS experiment, for example, performed the *Phase-1 upgrade* of the detector, which is partly described in Chapter 4.
The downtime was followed by *Run 3*, for which the centre-of-mass energy $\sqrt{s}$ was increased from $13\,\mathrm{TeV}$ to $13.6\,\mathrm{TeV}$. The run started in July 2022, and is planned to last until the end of 2025 [11].

2.2 The ATLAS Experiment

The ATLAS [2] detector is one of the two general-purpose detectors located approximately $100\,\mathrm{m}$ below ground in an experimental cavern at the LHC. It weighs around $7000\,\mathrm{t}$ and extends over a height of $25\,\mathrm{m}$ and a length of $44\,\mathrm{m}$. The detector consists of a cylindrical barrel symmetrically located around the collision point and is terminated by two endcaps on the sides. It has an onion-like structure with several different sub-systems as layers. An overview of the detector is shown in Figure 2.2. In the following, the coordinate system and the sub-systems of the ATLAS detector from inside out will be highlighted.

2.2.1 Coordinate System

The origin of the coordinate system [2] used in ATLAS is the nominal interaction point itself. The z-axis points in the beam direction, while the x- and y-axes span the transverse plane to it. The positive x-axis points to the centre of the LHC, the positive y-axis points upwards to the surface. In the x-y plane, the component of the particle momentum is called the *transverse momentum* p_{T}.
The ATLAS detector can be divided into two parts due to its symmetry. The *A-side* of the detector describes the part in positive z-direction, whereas the part in negative z-direction is called the *C-side*. Additionally, the azimuthal angle ϕ around the beam pipe and the polar angle θ with respect to the beam direction are defined. Instead of the polar angle θ to describe the angle relative to the beam line, the pseudorapidity η is commonly used in particle detectors. It is expressed through [2]

$$\eta = -\ln\left(\tan\frac{\theta}{2}\right). \tag{2.5}$$

The vertical direction to the z-axis corresponds to a pseudorapidity of 0, while it approaches $\pm\infty$ when closing in on to the beam line. To specify distances in the η-ϕ plane, the quantity $\Delta R = \sqrt{(\Delta\eta)^2 + (\Delta\phi)^2}$ is defined.

2.2.2 Inner Detector

The ATLAS *Inner Detector* (ID) [17] is the innermost detector sub-system of the ATLAS experiment. The main objective of the sub-system is to detect charged particles in several layers of the ID, using the collected information to reconstruct the particle trajectories and identify the primary collision vertex. Additionally, the ID is immersed in a $2\,\mathrm{T}$ magnetic field parallel to the beam axis, generated by a superconducting solenoid magnet that surrounds the inner detector. The magnetic field bends the tracks of the charged particles, which allows their charge and momentum to be determined from their trajectories.
The ID consists of three sub-detectors, the *Pixel Detector*, the *Semiconductor Tracker* (SCT), and the *Transition Radiation Tracker* (TRT), which are shown in Figure 2.3. The Pixel Detector and the SCT are covering a pseudorapidity range of $|\eta| < 2.5$, while the TRT is covering the range of $|\eta| < 2.0$.
The Pixel Detector is the innermost system of the ID with the goal of achieving a highly precise measurement of the particle position to ensure an excellent vertex resolution and reconstruction of tracks. For this purpose, small silicon pixels with high granularity close to the interaction point are used.

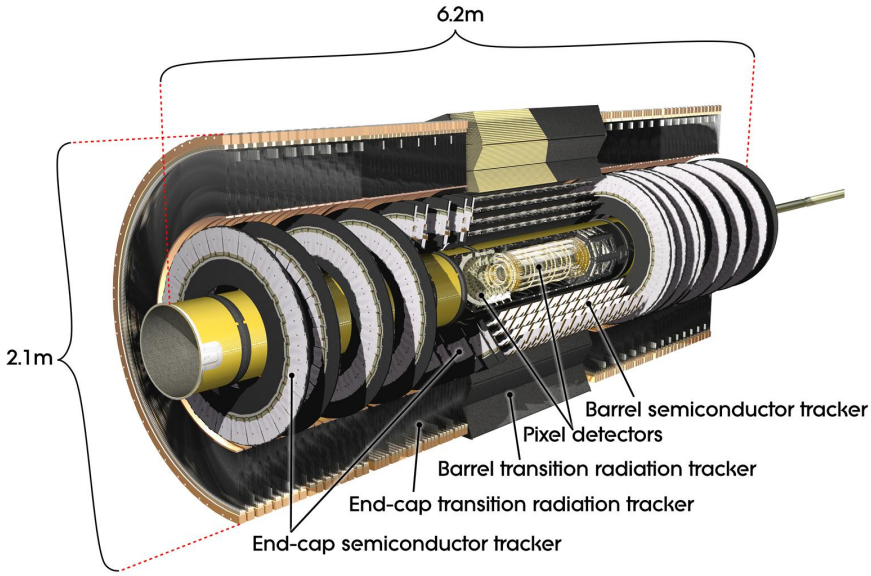

Figure 2.3: Schematic overview of the ATLAS inner detector. The inner detector is divided into three sub-detectors, the Pixel Detector, the SCT, and the TRT. Taken from [18].

The Pixel Detector's original design implemented for Run 1 consists of three layers of silicon pixel detectors in the barrel region and additional three discs of pixels in the endcaps. Approximately $90\,\%$ of the pixels have a size of $50\,\mu\mathrm{m} \times 400\,\mu\mathrm{m}$, with the remaining pixels located in the endcap discs having a size of $50\,\mu\mathrm{m} \times 600\,\mu\mathrm{m}$. The total number of pixels in the Run 1 setup was about 80 million [19].
In the Phase-0 upgrade of the ATLAS detector, a new innermost fourth pixel layer was added in the barrel region, which reduced the distance of the first pixel layer to the beam pipe from $5.05\,\mathrm{cm}$ to $3.27\,\mathrm{cm}$. The pixels of the new layer have a size of $50\,\mu\mathrm{m}$ x $250\,\mu\mathrm{m}$ resulting in an improved resolution of the track reconstruction in z-direction and are boosting the total amount of pixels to 92 million [20].
The second sub-detector of the ID in a radial distance of around $30\,\mathrm{cm}$-$51\,\mathrm{cm}$ from the beam line is the SCT [21]. It is one of the main components for measuring the transverse momentum of charged particles and plays an important role in the track reconstruction despite its lower granularity compared to the Pixel Detector. The SCT consists of two-sided modules with silicon-strip sensors on each side, organized in four separate layers in the barrel region and in nine discs in the endcaps. It contains six million individual channels in total.
The last and outermost sub-detector of the ID is the TRT [22], which consists of around $300\,000\,\mathrm{t}$hin-walled drift tubes. The tubes are filled with a Xe-CO_2-O_2 gas mixture and

use a thin gold-plated tungsten wire placed in the middle of the tube as their anode. The ionisation of the gas mixture by a particle is used to provide track information. Additionally, the transition radiation effect is used by the TRT to contribute to the particle identification.
The ID is designed to achieve a transverse momentum resolution of [23]

$$\frac{\sigma_{p_\mathrm{T}}}{p_\mathrm{T}} = 0.05\% p_\mathrm{T}\mathrm{GeV} \oplus 1\%. \tag{2.6}$$

2.2.3 Calorimeters

The calorimeter system of the ATLAS experiment is encompassing the further inside positioned ID and superconducting solenoid. It measures the energy and position of charged and neutral particles. In addition, the shape of the particle showers in the calorimeters is used for particle identification.
Figure 2.4 shows an overview of the ATLAS calorimeter system. It comprises an electromagnetic calorimeter and a hadronic calorimeter, jointly covering the region of $|\eta| < 4.9$ and the full ϕ range of 2π. The electromagnetic calorimeter is specialized for the precise measurement and absorption of energy from electrons and γ particles due to their electromagnetic interactions. Furthermore, it captures a fraction of the energy from passing hadrons, which are entirely absorbed by the subsequent hadronic calorimeter. The latter primarily measures energy from hadrons via strong and electromagnetic interactions.
The calorimeter systems are constructed as sampling calorimeters, featuring alternating layers of dense absorbing and active material. The traversing particles interact with the absorber, losing some of their energy while producing a shower of secondary particles through either electromagnetic interactions, such as pair production and bremsstrahlung, or hadronic interactions, such as nuclear spallation, evaporation, or fission. The less energetic secondary particles are then measured with the active material. The collected position and energy information of the secondary particle showers are used to reconstruct the energy, track, and shower shape of the traversing, primary particle.
Sampling calorimeters can be produced more cheaply and compactly, since the absorber allows the traversing particles to be completely absorbed more quickly. Furthermore, they usually have a higher spatial resolution due to a fine segmentation of the different layers, which leads to a more accurate reconstruction of the shower shape and thus to a better particle identification. Conversely, sampling calorimeters exhibit a drawback of poorer energy resolution, in contrast to homogeneous calorimeters consisting only of active material, due to the energy loss in the absorber.

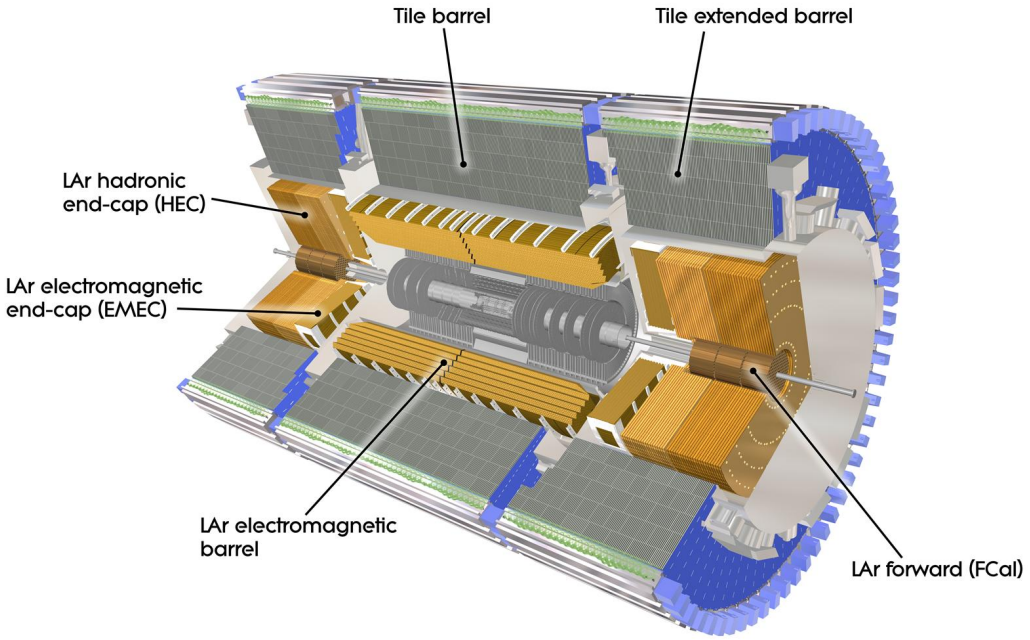

Figure 2.4: Schematic overview of the ATLAS calorimeter. The calorimeter is divided into an electromagnetic and a hadronic part. These can be further divided into the LAr electromagnetic barrel (EMB), the Tile barrel (LB), and the Tile extended barrel (EB) for the calorimeter barrel region, EMEC and HEC for the endcaps, and the FCAL systems for the forward regions. Taken from [24].

The Liquid Argon Calorimeter

The *Liquid Argon* (LAr) calorimeter [25] can be divided into four different parts, the *Electromagnetic Barrel* (EMB), the *Electromagnetic Endcap* (EMEC), the *Hadronic Endcap* (HEC), and the *Forward Calorimeter* (FCAL).

The EMB covers the range of $|\eta| < 1.475$ and is organised in layers of accordion-shaped lead absorber plates, which ensure a full-ϕ coverage, while the volume between them is filled with liquid argon as the active material, which is ionised by the secondary particles. In the middle of the volume of two lead absorber plates, a Kapton electrode is placed that gathers the ionisation charges, which leads to an electrical signal of the calorimeter cells. The EMB is organised in three layers (*frontlayer*, *middlelayer*, and *backlayer*) with an additional fourth *presampler* layer in front.

The EMEC covers the range of $1.375 < |\eta| < 3.2$ and is arranged in two wheels, one on each side of the EMB. It uses the same technical structure and functionality as the barrel, but the number of layers varies with $|\eta|$. In the range of $1.5 < |\eta| < 2.5$ the EMEC

has still three layers, but the presampler only covers a range of $1.5 < |\eta| < 1.8$. In the regions $1.375 < |\eta| < 1.5$ and $2.5 < |\eta| < 3.2$ only two layers are installed, without any presampler coverage [26]. The energy resolution for electrons achieved by the EMB and EMEC is [2]

$$\frac{\sigma_E}{E} = \frac{10\%}{\sqrt{E(\text{GeV})}} \oplus 0.17\%. \tag{2.7}$$

The HEC is following the EMEC in both endcaps and is covering a similar range of $1.5 < |\eta| < 3.2$. Instead of accordion-shaped lead absorbers, it uses flat-plate copper as the absorbing material and has three electrodes, with the middle electrode serving as the collector for the ionised particles, while the other two provide the high voltage. The volume between the absorbers is again filled with LAr as active material and divided into four separate drift zones by the electrodes.
LAr is also deployed as an active material in the FCAL. It covers the high η range of $3.1 < |\eta| < 4.9$ and is divided into three parts, one electromagnetic module (FCal1) and two hadronic modules (FCal2 and FCal3). FCal1 is the innermost layer and mainly consists out of copper plates as an absorber. The absorber material is perforated with holes parallel to the z-axis, which are filled with tubes, containing a copper rod, an electrode, and the active material.
FCal2 and FCal3 follow FCal1 and use the same structure and functionality except for tungsten rods instead of copper to realise a higher absorption length. The measured energy resolutions of the HEC and the FCals with pions resulted in [2]

$$(\frac{\sigma_E}{E})_{\text{HEC}} = \frac{70.6\%}{\sqrt{E(\text{GeV})}} \oplus 5.8\% \quad \text{and} \quad (\frac{\sigma_E}{E})_{\text{FCal}} = \frac{94.2\%}{\sqrt{E(\text{GeV})}} \oplus 7.5\%. \tag{2.8}$$

The Tile Calorimeter

The Tile calorimeter [27] is the hadronic calorimeter in the barrel region of the ATLAS experiment. It is positioned behind the EMB, and can be divided in the *Long Barrel* (LB) with a coverage of $|\eta| < 0.8$ and the *Extended Barrel* (EB) in the range of $0.8 < |\eta| < 1.7$. Both parts can be separated radially into three layers, and are constructed with steel absorbers and tile scintillators as the active material.
The secondary particles in the showers produced by the traversing particles are resulting in scintillating light in the tiles. The light is collected by wavelength-shifting fibres and passed on to *Photomultiplier Tubes* (PMTs). The PMTs transform the forwarded light into an electrical signal that is amplified and proportional to the energy collected in the scintillator.

For the Tile calorimeter, the energy resolution was measured with the use of pions and resulted in [28]

$$\frac{\sigma_E}{E} = \frac{52.7\%}{\sqrt{E(\text{GeV})}} \oplus 5.7\%. \tag{2.9}$$

2.2.4 Muon Spectrometer

Muons are minimally ionising particles and can therefore penetrate large amounts of material, namely the calorimeters, without complete absorption of their energy. In order to address this challenge, the *Muon Spectrometer* (MS) [29] as the last layer of the ATLAS detector was designed. Its purpose is the precise track and momentum measurement of the muons, which is achieved by two sub-detectors, namely *Monitored Drift Tubes* (MDTs) and *Cathode Strip Chambers* (CSCs). In addition, the *Resistive Plate Chambers* (RPCs) and the *Thin Gap Chambers* (TGCs) enable a trigger system, which is based on the collected muon information.
An overview of the spectrometer with all the sub-detectors is shown in Figure 2.5. Additionally, the three superconducting toroid magnets, one for the barrel and one for each endcap, are displayed. They provide a magnetic field of up to $3.5\,\mathrm{T}$ for the momentum measurement of the muons. The detection principle of all sub-detectors of the MS is similar and is based on the ionisation of a gas mixture by traversing charged particles. The resulting ions drift to an installed electrode and lead to an electrical signal.
The MDT chambers contain three to eight drift tubes that are filled with an Ar/CO_2 gas mixture and use a centrally positioned tungsten-rhenium wire as an electrode. The chambers are organised in three layers covering the region of $|\eta| < 2.7$, except for the first layer, which is replaced by CSCs in the range of $2.0 < |\eta| < 2.7$.
The CSCs are multi-wire proportional chambers with radially oriented wires and with two cathode plates separated into strips. The strips of one of the cathodes are aligned parallel to the wires, while the others have a horizontal arrangement. The structure of the CSCs leads to a higher granularity in relation to the MDTs, which are needed for the increased rates and background in the larger $|\eta|$ region. The CSCs use gold-plated tungsten-rhenium wires, copper cathodes, and also an Ar-CO_2 gas mixture but with slightly different concentration than the MDTs.
For the muon trigger system, RPCs are used in the barrel region of $|\eta| < 1.05$ and TGCs in the endcaps with a coverage of $1.05 < |\eta| < 2.4$. Both systems have to provide precise timing measurements for the identification of the correct BC and the determination of the BCID, from which the traversing muon originates. In addition, a fast track and pulse information must be provided in order to make a correct trigger decision. The complete

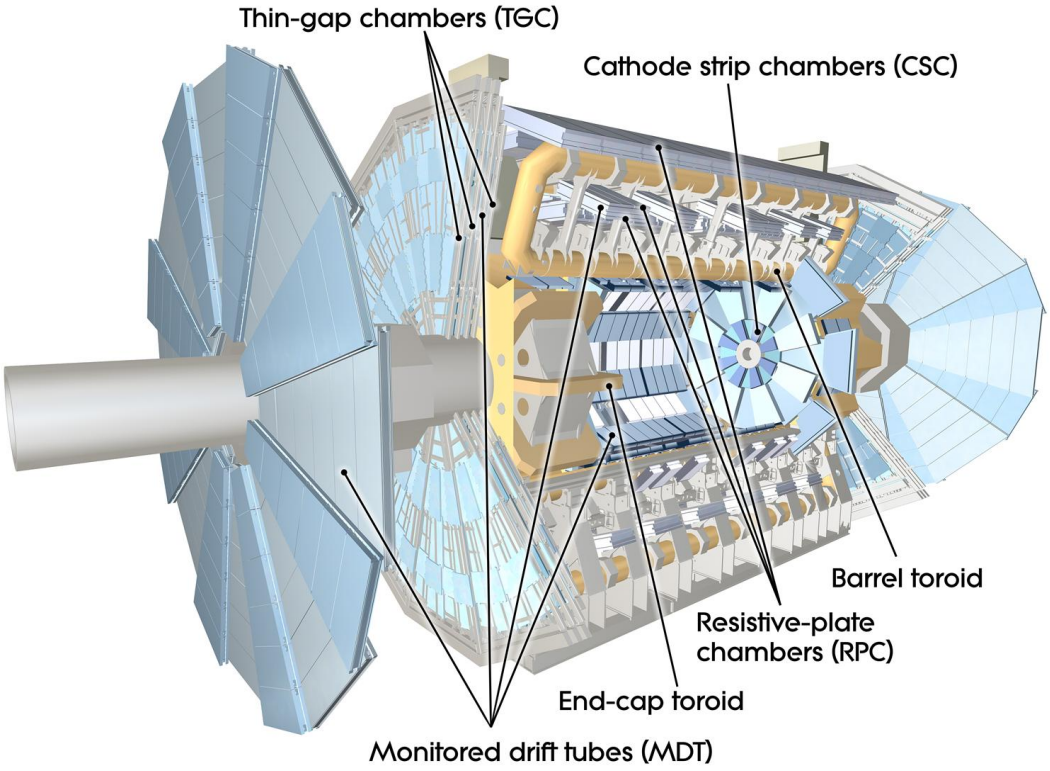

Figure 2.5: Schematic overview of the ATLAS Muon Spectrometer. The muon system consists of four major sub-detectors, the MDTs and CSCs for precise track and momentum measurements and the RPCs as well as the TGCs for trigger purposes. Taken from [30].

muon trigger system is separated into 208 trigger sections.

The RPCs consist of pairs of resistive plates with a gap of $2\,\mathrm{mm}$, which is filled with a complex gas mixture. The electrodes are placed on the outside of the resistive plates.

The TGCs in the endcaps are multi-wire proportional chambers, characterised by the smaller wire-to-cathode distance of $1.4\,\mathrm{mm}$. They are filled with a CO_2/n-C_5H_{12} gas mixture and use gold-plated tungsten wires.

3 The Trigger and Data Acquisition System of the ATLAS Experiment

The *Trigger and Data Acquisition* (TDAQ) [2, 10] system is responsible for processing the large amount of data produced by all sub-detectors of the ATLAS experiment at a rate of $40\,\mathrm{MHz}$ and with an event size of about $1.6\,\mathrm{MB}$ [31]. In order to cope with the data, a two-stage trigger was implemented that searches for possible physics events of interest while reducing the data rate to one that can be handled by the detector's readout and storage system. The first stage is the hardware-based *Level-1* (L1) trigger, the second the software-based *High-Level-Trigger* (HLT). Besides the two trigger stages, the TDAQ system generally consists of two additional parts, the *Detector Read-Out* and the *DataFlow*, which is shown in Figure 3.1.

The sub-detectors are equipped with buffers that are filled with the event data at the rate of $40\,\mathrm{MHz}$. The buffer size corresponds approximately to the time period of $2.5\,\mu\mathrm{s}$, often referred to as the fixed *latency* of the L1 system. To avoid data loss, the final L1 trigger decision on whether an event is of interest must be made within this time frame. This decision is based on the information the *Central Trigger Processor* (CTP) receives as an input from the L1 sub-systems. If the CTP reaches a positive trigger decision, it sends a so-called *Level-1 Accept* (L1A) to the various sub-detectors and the L1 sub-systems, which leads to the readout of the corresponding event data from the buffers. The maximum L1A rate in normal operations is around $100\,\mathrm{kHz}$, which reduces the event rate by a factor of 400.

The event data of possible interesting events are read out and subsequently forwarded by the *Data Acquisition* (DAQ) system to the HLT. Afterwards, the HLT performs advanced software algorithms to further reduce the event rate to about $1.5\,\mathrm{kHz}$ and thereupon store the data of the selected interesting events [32].

The components described are examined in more detail in this chapter, with the focus on the Level-1 Trigger System in Section 3.1 and specifically the Level-1 Calorimeter Trigger in Section 3.1.1.

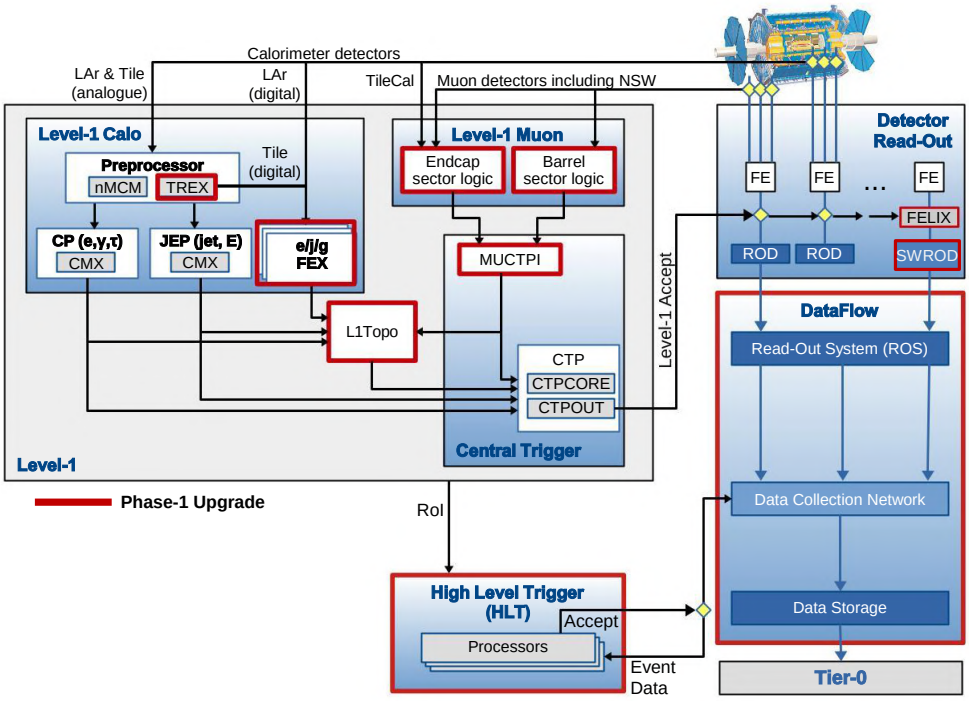

Figure 3.1: Overview of the ATLAS TDAQ system. The components introduced or modified during the LS2 in the course of the Phase-1 upgrade are outlined in red. Taken and modified from [11, 33].

3.1 The Level-1 Trigger System

The Level-1 trigger system searches for interesting physics signatures using data from all calorimeters and the two muon trigger systems, RPCs and TGCs. The muon systems provide information to identify signatures from muons, while the calorimeter data are used to search for electrons, photons, jets, and τ candidates, as well as to find events with large missing transverse energy $E_{\mathrm{T}}^{\mathrm{miss}}$ and total transverse energy $E_{\mathrm{T}}^{\mathrm{tot}}$.
The L1 system can be divided into four main components: the *Level-1 Calorimeter* (L1Calo) trigger and the *Level-1 Muon* (L1Muon) trigger, which process the calorimeter data and the muon data, respectively, the *Level-1 Topological* (L1Topo) trigger and the *Central Trigger*. All sub-systems are explained in more detail below.

3.1.1 The Level-1 Calorimeter Trigger

The L1Calo [34] trigger receives 7168 analogue signals so-called *Trigger Tower* (TT) with a typical dimension of $\Delta\eta \times \Delta\phi = 0.1 \times 0.1$ and a coarser resolution above $|\eta| > 2.5$. This input stems from the calorimeters, where the TTs are summed from the about

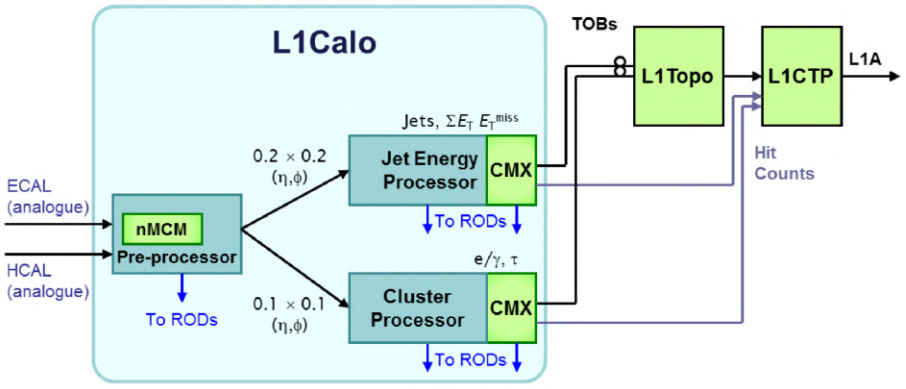

Figure 3.2: Legacy L1Calo Run 2 system architecture. New components introduced in the course of the Phase-0 upgrade during the LS1 are shown in green. Taken from [36].

190 000 existing calorimeter cells [35], to search in the L1Calo system for electron, photon, τ, and jet candidates. Additionally, the L1Calo trigger computes the missing transverse energy $E_{\mathrm{T}}^{\mathrm{miss}}$ and the total transverse energy $E_{\mathrm{T}}^{\mathrm{tot}}$. The number of physics object candidates is counted and passed to the CTP. In addition, the L1Topo system receives trigger information of the candidates in form of so-called *Trigger Objects* (TOBs).
The L1Calo trigger mainly consist of three components: the *PreProcessor* (PPr), the *Cluster Processor* (CP), and the *Jet Energy Processor* (JEP). The illustration in Figure 3.2 shows the so-called *legacy* L1Calo system, which was used in Run 1 and Run 2. The components marked in green were part of the Phase-0 upgrade of L1Calo trigger and added new functionalities to the Run 2 system. Furthermore, the legacy system is used in Run 3 and runs parallel to the new Phase-1 L1Calo trigger system, which is described in more detail in Chapter 4.

3.1.1.1 Analogue Input

An overview of the analogue input signal path [34, 37, 38] is given in Figure 3.3. The 7168 analogue TT signals are transmitted from the detector via 616 16-way twisted-pair cables to the electronics caverns, namely *USA15*, which house the L1Calo system. The cables are routed to minimise their length in order to reduce the introduced delay, resulting in cables in the range of 30 m for the shortest from LAr EMB to 70 m for the longest from Tile EB.
The long Tile EB cables also contain the information for the L1Muon system, which are separated from the Tile information intended for L1Calo in the *Tile Calorimeter Patch Panels* (TCPPs). The remaining Tile TT information are forwarded to the receivers, which

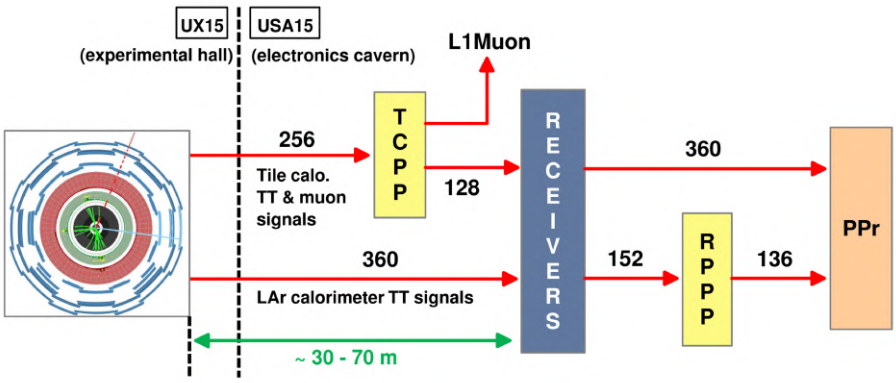

Figure 3.3: Overview of the analogue TT signal path from the calorimeters to the L1Calo system. The numbers shown in the figure represent the number of cables used in the respective path. Taken from [37].

additionally receive the LAr calorimeter TT signals.

The receivers include *Variable Gain Amplifiers* (VGAs) [39] that scale the incoming analogue signals. They convert the hadronic and forward TT signals from raw energy E by multiplication with $\frac{1}{\cosh(\eta)}$ to transverse energy E_{T}, while the signals from EMB and EMEC are already converted to E_{T} in the LAr front-end electronics. In addition, the VGAs compensate for attenuation in the long cables and set the E_{T} calibration for all TT signals via raw energy calibration gains provided by the energy calibration, which is the subject of Section 8.1.3. Furthermore, the VGAs use two other parameters, with one being the *Pulser-to-Physics* (P2P) corrections. These corrections compensate for differences between the pulses used during the calibration process and the signals during normal physics data taking. For instance, the calibration system generates wider pulses compared to the signals produced by particles. The second parameter is only used for the LAr system and compensates for changes in the high voltage of the LAr calorimeters. All factors are combined and used in the VGAs as an overall receiver gain.

In addition, the receiver system rearranges the incoming signals so that typically a 16-way twisted-pair cable contains the signals of a 0.4×0.4 region in the η-ϕ space.

Furthermore, in two cases, analogue signals are summed in the receivers. The first is the so-called *overlap* region in the range of $1.375 < |\eta| < 1.475$, in which the EMB and EMEC cover the same η-ϕ region and must be combined accordingly. The second are the hadronic forward FCal2 and FCal3 regions, where the neighbouring TTs are summed up to reduce the number of input channels to the PPr. The receivers also introduce a monitoring possibility to check analogue trigger tower signals via an oscilloscope, which was used during investigations of problematic TTs described in Section 8.2.6.

Most of the receiver's calibrated TT output signals are routed directly to the PPr system, but some TT signals from special regions take an intermediate step for additional rearrangement in the *Receiver to PreProcessor Patch Panels* (RPPPs) [38, 40] before entering the PPr.

3.1.1.2 PreProcessor

The PreProcessor [10, 41] is the first processing stage of the L1Calo Trigger System, which consists of 124 *PreProcessor Modules* (PPMs) inside of eight VME[2] crates. Six of them are responsible for processing the analogue TT signals from the LAr calorimeter, the other two are handling the signals from the Tile calorimeter.
An overview of the PPM and its functionality is given in Figure 3.4. Each PPM receives a total of 64 TT signals via four input cables carrying 16 differential analogue signals each. The input cables are connected to the PPMs through four input connectors mounted on the module. The differential signals are forwarded to *Analogue Input* (AnIn) boards, where they are first converted into single-ended signals and then further prepared for digitisation. The preparation step also includes adding a programmable analogue signal from the *Digital-to-Analogue Converter* (DAC) located on the AnIn board to the input signal. The additional offset can be modified in $2.4\,\mathrm{mV}$ DAC steps and allows the baseline of the signal, also called *pedestal*, to be set, to ensure that the signal is in the digitisation window and also that all PPM channels have the same baseline. The DAC value is determined in the DAC scans described in Section 8.1.1.
The output of the AnIn board is used as input for 16 *Multichip Modules* (MCMs) mounted on the PPM. The original design in Run 1 contained an ASIC[3]-based MCM, which was upgraded in Run 2 to a *new MCM* (nMCM) with a FPGA[4] called the *Calorimeter Information PreProcessor* (CALIPPR) FPGA, which took over the task of the Run 1 ASIC and added more functionality.
Each nMCM, which is the main processor unit of the PPM, is supplied with four TT signals prepared for digitisation with a typical coverage of 0.1×0.1 in the η-ϕ space from the AnIn boards. The first nMCM step is the digitisation of the four incoming TT signals, which is done by two dual-channel 10-bit *Analogue-to-Digital Converters* (ADCs) with a sampling frequency of $80\,\mathrm{MHz}$. The $80\,\mathrm{MHz}$ clock is provided by the CALIPPR FPGA, whereby the clock phase can be set in steps of $1.042\,\mathrm{ns}$ relative to the $40\,\mathrm{MHz}$ LHC clock. This process is called *fine-timing* and is necessary to ensure that the peak position of the

[2] Versa Module Europa
[3] *Application Specific Integrated Circuit*
[4] *Field Programmable Gate Array*

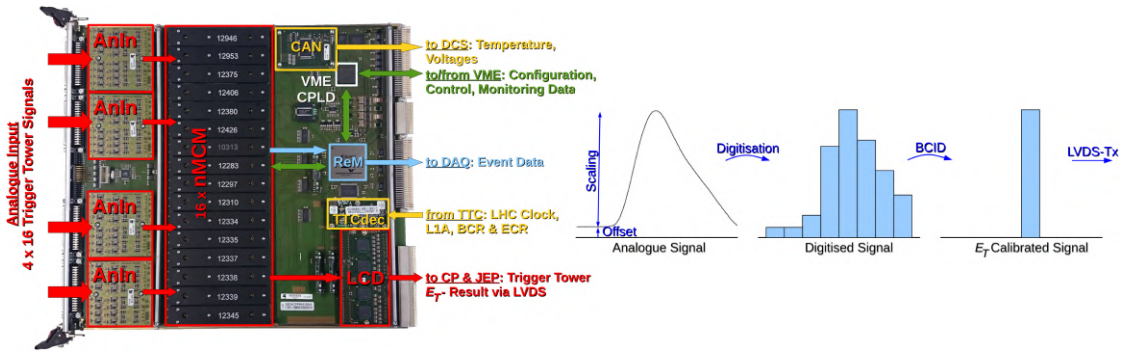

(a) PreProcessor Module (PPM) **(b)** PPM Functional Overview

Figure 3.4: Overview of the PreProcessor Module (PPM). Figure (a) shows the PPM with all components used in Run 2, while Diagram (b) gives an overview of the PPM functionality. Both images were taken and modified from [10].

analogue signal is sampled at the highest point to ensure optimal performance of the following processor chain.

The sampled signals enter a *First-In-First-Out* (FIFO) memory buffer with maximum programmable depth of 16 BCs, after the digitisation via the ADCs. The depth can be adjusted in steps of one BC depending on the position of the TT within the detector. This allows to compensate for varying cable lengths and the different time-of-flight of the particles from the interaction point to the calorimeter to ensure that the incoming TT signals are aligned and thus originate from the same BC. This procedure is referred to as *coarse-timing*. The adjustment of the fine- and coarse-timing are discussed in Section 8.2.3 and 8.2.7.1.

The synchronised digitised signals are then processed by the Bunch Crossing Identification (BCID) algorithm on the CALIPPR FPGA, which associates a certain BC to a significant energy deposition within the calorimeters, whose analogue pulses extend over several BCs. First, the algorithm uses a *Finite Impulse Response* (FIR) filter that increases the signal-to-noise ratio of the digitized ADC samples. The FIR filter determines the filter output f_i by summing five weighted consecutive ADC samples - two before the considered BC i and two after. The summation is conducted at a frequency of $40\,\mathrm{MHz}$, employing every alternate ADC sample from the digitisation process. The calculation is implemented as [10]

$$f_i = \sum_{j=0}^{5} c_j A_{i-2+j}, \tag{3.1}$$

with the filter coefficient weights c_j, which are previously determined in a special analysis, and the digital ADC sample A_i at the given BC i. The second step of the BCID algorithm

is the *Peak Finder*. It uses the filter output f_i to search for a local maximum to identify the peak of the digitised calorimeter signal. On the occurrence of the condition [10]

$$f_{i-1} < f_i \geq f_{i+1} \tag{3.2}$$

in BC i, the output of the Peak Finder algorithm for i is set to 1, resulting in the filter output f_i being fixed as the amplitude of the calorimeter signal and used in the following processing chain. For all other cases, the Peak Finder output is set to 0, which also means that the output of the BCID logic of the following BC is discarded [10, 42].
The last step implemented in the CALIPPR FPGA comprises the *Look-Up Tables* (LUTs), which are typically implemented as linear functions and convert the output of the BCID algorithm into a calibrated 8-bit E_T value before transmitting it to the CP and JEP systems. This final E_T calibration is complemented by a pedestal subtraction, a noise suppression, and the disabling of noisy as wells as problematic TTs.
The LUT for the CP systems convert the FIR output to an E_T value in the range of $0\,\mathrm{to}$ $127.5\,\mathrm{GeV}$ with a resolution of $500\,\mathrm{MeV}$, while the LUT for the JEP systems has a range from $0\,\mathrm{to}\,255\,\mathrm{GeV}$, with the *Least Significant Bit* (LSB) corresponding to $1\,\mathrm{GeV}$.
To implement the pedestal subtraction in the LUTs, the linear functions are extended by an offset, whereby for the noise suppression only digital filter values above a configurable noise cut are assigned a non-zero E_T value. For noisy and problematic TT, the LUT output can be permanently set to $0\,\mathrm{GeV}$ and thus the corresponding TT can be *masked*. This procedure is mentioned again in Section 8.2.6.
The resulting E_T values are then further processed and packed into the data formats shown in Figure 3.5. Electrical *Low-Voltage Differential Signals* (LVDS) are used to transmit the packed signals to the CP and JEP system, with two LVDS links to the CP and one LVDS link to the JEP system for each nMCM. The required data formats of both processor systems use 12-bit words with a *start* and *stop* bit, leaving 10-bit for the actual data content.
The CP system requires the 8-bit E_T information from all TTs, but this would result in the need of four LVDS links for the four processed TT of a nMCM to transmit all the information. However, only two links to the CP system are available per nMCM, so a multiplexing method called *Bunch-Crossing Multiplexing* (BCMUX), shown in Figure 3.5, is used to reduce the total number of links required to two. The BCMUX procedure exploits the fact that after a positive BCID decision, the following BC is empty and uses it to forward the E_T information of a second nMCM channel over the same LVDS link. In addition, a *BcMux* bit is added to the data packet to indicate which channel has just been

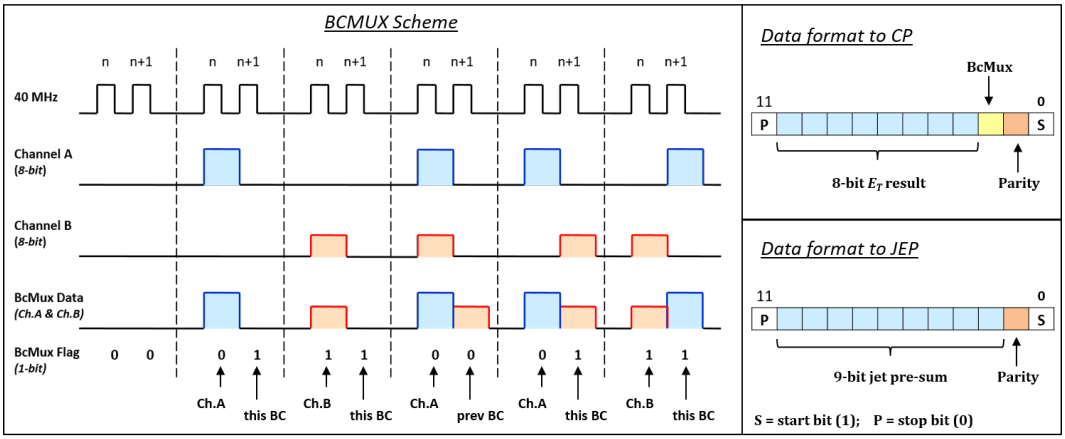

Figure 3.5: The Bunch Crossing Multiplexing (BCMUX) scheme with all possible configurations is shown. In addition, the 12-bit LVDS data formats for the JEP and CP system are displayed. Taken from [43].

forwarded. Besides the start and stop bit, the 8-bit E_T value and the BcMux bit, an odd *parity* bit is sent to the processor systems as part of the data transmission. This bit is set to 1 if the number of non-zero bits of the 10-bit data content is odd, and is compared by the receiving systems with a self-calculated parity value to check the data integrity.
The JEP system uses only 0.2×0.2 *jet sums* instead of the full 0.1×0.1 (η-ϕ) information of each TT. Therefore, the four 8-bit E_T values per nMCM are combined in the first step to a 10-bit sum and converted to a 9-bit sum in the second step by truncating the most or least significant bit. This again leaves space in the 12-bit data word for an odd parity bit.
The described LVDS outputs of the PPMs are forwarded to the TREX in the real-time path after the Phase-1 upgrade of the two Tile calorimeter crates, which is described in more detail in Section 5.2. In addition, the PPMs of both crates were adjusted to be compatible with the new Phase-1 hardware. This is discussed in more detail in Section 5.1. Furthermore, the simulated LVDS outputs play a crucial role in the implemented TREX simulation, which is highlighted in Section 7.2.
After a positive trigger decision of the CTP, the PPM also receives an L1A and initiates the readout of the PPM digital ADC and LUT E_T values. The data is packed on the *Readout Manager* (ReM) FPGA of the PPM in the so-called legacy *G-Link* format, which, in addition to a variable amount of ADC and LUT values for multiple BCs, consists of a header that contains information about the read out event, such as BC or the event number. More details about the data format used can be found in [10].
The typical readout configuration of the PPM in normal data taking is 5 read out ADC values, two values before and two after the peak, with 1 LUT read out value, also called "5+1" configuration. Other readout configurations used for mostly calibration purposes

are "7+1", "11+1" or even "15+1" readout, which is used for example for the Phos4 scans described in Section 8.1.2. The larger number of ADC slices read out maps a wider range of the pulse and thus allows a more detailed analysis of the signals. Another configuration that allows a more sophisticated analysis of the obtained signal is to use the original sampling frequency of $80\,\mathrm{MHz}$ and not to discard every second ADC sample. This allows a representation of the signal with higher resolution, which is very useful for the timing analyses described in Section 8.2.2.1 and 8.2.7.1.

3.1.1.3 Cluster Processor

The CP system [34] consists of four crates, each covering one ϕ quadrant and containing 14 *Cluster Processor Modules* (CPMs), resulting in a total number of 56 CPMs. The CPMs receive the 8-bit E_{T} results from the PPMs in the range of $|\eta| < 2.5$ with the resolution of 0.1 $\times$ 0.1 in the η-ϕ space, which corresponds to the best available resolution of one TT. Two algorithms are executed in the CPMs, one for the identification of electrons and photons (e/γ) and the other for hadronically decaying τ particles. Both algorithms use a *sliding window*, which corresponds to a 4 $\times$ 4 TT window in the electromagnetic and hadronic layer that scans the entire region covered by the CP system by moving the window one TT at a time in η or ϕ. The 4 $\times$ 4 window consists of a 2 $\times$ 2 core region and a surrounding isolation ring, which is shown in Figure 3.6. As indicated in the image, four different E_{T} sums are formed from the 1 $\times$ 2 or 2 $\times$ 1 neighbouring TTs in the core region.
In the e/γ algorithm, also called *EM* algorithm, the four E_{T} sums are compared to a programmable threshold, where only one of the four sums needs to exceed it for a e/γ candidate to be determined. In addition, two isolation parameters are implemented to ensure unique identification of the e/γ candidates by taking advantage of two characteristic properties. The first is the electromagnetic isolation that requires narrow showers, which is characteristic for e/γ particles. For this purpose, the sum of the 12 TTs surrounding the core region is calculated and compared again to a programmable threshold. The second parameter is the hadronic isolation of the e/γ algorithm, which is computed by summing the E_{T} values of the 4 TTs in the 2 $\times$ 2 hadronic inner core to ensure the characteristic complete energy deposition of e/γ candidates in the electromagnetic layer. The E_{T} sum of the hadronic inner core is again compared to an adjustable threshold.
The τ algorithm uses the same four E_{T} sums of the electromagnetic layer, but adds the 2 $\times$ 2 hadronic core sum to account for the additional hadronic energy deposition of a τ particle, and then compares the combined sums to a programmable threshold.

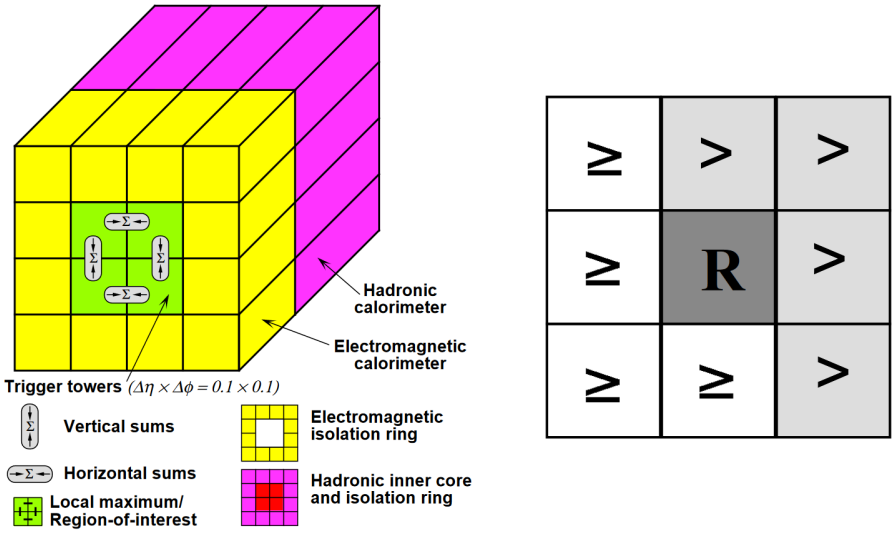

Figure 3.6: An illustration of the CP algorithm with the core region and isolation criteria is shown on the left, while the RoI definition and the comparison with the eight neighbouring regions is illustrated on the right. Taken from [2].

For the electromagnetic isolation, the τ algorithm uses the same sum of the 12 TTs surrounding the core region as the e/γ algorithm. The sum of the isolation ring around the inner core of the hadronic layer is calculated and then compared against a threshold to form the hadronic isolation.
In the course of forming trigger objects of the identified candidates, an additional procedure, shown in Figure 3.6, is implemented to prevent the same trigger object from being counted multiple times by the sliding window algorithm. During the procedure, the sums of the core region of the electromagnetic and hadronic layer are compared with the sums of the eight overlapping core regions of the neighbouring windows to search for a local maximum. The core with the local maximum is called the *Region of Interest* (RoI), whose η-ϕ coordinates are included in the RoI information transmitted to the HLT. Additionally, the *Common Merger Modules Extended* (CMXs), explained in Section 3.1.1.5, receive the type, position, and energy of the identified candidates in form of TOBs.

3.1.1.4 Jet Energy Processor

The JEP system [34] is composed of two VME crates housing 16 *Jet Energy Processor Modules* (JEMs) each, resulting in a total number of 32 JEMs. The JEMs receive the complete calorimeter information in the range up to $|\eta| < 4.9$ in the form of 9-bit jet sums from the PPr system, which have a coarser resolution of typically 0.2 $\times$ 0.2 in the

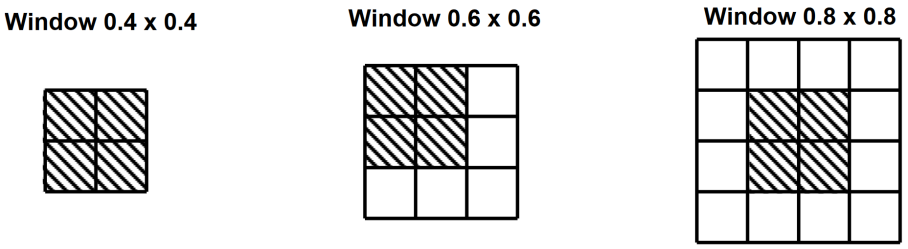

Figure 3.7: The three sizes of the sliding windows of the JEP algorithm and their respective RoI position as the shaded area. Taken from [2].

η-ϕ space except for jet sums in the endcap region of $2.9 < |\eta| < 3.2$ with a resolution of 0.3 $\times$ 0.2. The JEMs form so-called 10-bit *jet elements* by adding up the jet sums of the electromagnetic and hadronic calorimeters within the same η-ϕ coordinates.
The JEMs perform trigger algorithms to identify jet candidates, to determine the transverse energy for the jet elements E_{T}, and compute E_x and E_y, the jet energy components along the x and y directions, to calculate the missing transverse energy $E_{\mathrm{T}}^{\mathrm{miss}}$ and the total transverse energy $E_{\mathrm{T}}^{\mathrm{tot}}$ for trigger purposes.
The jet trigger algorithm is based on the jet elements and, similar to the CP system, uses a sliding window algorithm that scans the entire region covered by the JEP system by moving the window one jet element at a time in η or ϕ. Unlike the CP algorithms, the window size can be varied depending on the desired jet candidates with possible settings of 2 $\times$ 2, 3 $\times$ 3 or 4 $\times$ 4 jet elements [34], corresponding to 0.4 $\times$ 0.4, 0.6 $\times$ 0.6, and 0.8 $\times$ 0.8 in the η-ϕ space, which is shown in Figure 3.7. For each window, the contained transverse energy is calculated and then compared with variable thresholds to identify a jet candidate. Additionally, a similar procedure to the CP algorithms is performed to prevent multiple counting of the same object and to find a local maximum, i.e. the RoI with a size of 0.4 $\times$ 0.4 in η-ϕ. For the 2 $\times$ 2 and 4 $\times$ 4 window, the four central jet elements are defined as the RoI. For the 3 $\times$ 3, however, the window with the highest E_{T} sum is identified as the RoI, which is forwarded to the HLT.
All the jet elements are also used to determine the respective jet element energy sums of E_{T} and its projections E_x and E_y. The energy sums are then forwarded to the CMXs. In addition, the CMXs receive the jet candidates determined by the jet algorithm in the form of TOBs.

3.1.1.5 Common Merger Module Extended

The Run 1 *Common Merger Module* (CMM) [34] was replaced by the *Common Merger Module Extended* (CMX) [36, 44] as part of the Phase-0 upgrade of the L1Calo trigger system.
Instead of receiving the *trigger multiplicity* of objects above certain programmable E_{T} thresholds directly from the CPMs or JEMs as in Run 1 and adding them up to the system-wide multiplicity results for the CTP, the CMXs receive in Run 2 TOBs from both processor systems and calculate the total multiplicity results themselves. For this purpose, the system-wide TOB energies received are compared with programmable thresholds and the number of TOB energies within a threshold is counted. Afterwards, the counted values are forwarded as the total trigger multiplicity results to the CTP system.
In addition, the CMXs act as an interface to the L1Topo system introduced in Run 2 with the purpose of forwarding the received TOBs to it.
Another responsibility is the system-wide calculation of the missing transverse energy $E_{\mathrm{T}}^{\mathrm{miss}}$ and the total transverse energy $E_{\mathrm{T}}^{\mathrm{tot}}$ using the received E_{T}, E_x and E_y energy sums by the JEMs. The calculated values are compared again with various thresholds and the resulting information is forwarded to the CTP.

3.1.2 The Level-1 Muon Trigger

The L1Muon trigger [36] uses the information provided by the RPCs and TGCs to search for muon candidates in the 208 trigger sections, calculate their transverse momenta p_{T}, and assign them to the correct BC. In addition, the p_{T} values of the candidates are compared with six programmable thresholds, whereupon the information is forwarded to the *Muon-to-CTP Interface* (MUCTPI). The MUCTPI counts the amount of candidates within each p_{T} threshold, similar to the CMXs, and sends the trigger multiplicity information to the CTP system. Additionally, the L1Muon trigger uses Tile calorimeter information to improve the rejection of muon triggers fired by other physics objects in the η range of $1.0 < |\eta| < 1.3$.
During the Phase-1 upgrade, the Muon Trigger System received several improvements. Two major ones are the installation of the *New Small Wheels* (NSWs) [45] in the endcaps of the Muon Spectrometer, which are designed to handle the high background rate with increasing instantaneous luminosity, while maintaining the trigger efficiency, and the new MUCTPI [46], which should be compatible with the new inputs from the NSWs and provide higher granularity muon information to the L1Topo.

3.1.3 The Level-1 Topological Trigger

The L1Topo trigger [47] was introduced as a new system in the course of the Phase-0 upgrade. It receives the TOBs from the CMXs and from the L1Muon system to run several topological algorithms using the combined information to identify events of interest based on the event topology. The algorithm results are then forwarded to the CTP system for the L1 trigger decision.

3.1.4 The Central Trigger Processor

The CTP [10, 48] forms the final component in the Level-1 trigger chain and receives the output of L1Topo in addition to the multiplicity results of the L1Calo and of the L1Muon system. The incoming signals of all systems are then compared with the requirements of *trigger items*, which are defined in the *L1 trigger menu*. In total, the L1 trigger menu consists of 512 possible trigger items, whereby only the requirements of a single trigger item have to be fulfilled in order to achieve a positive trigger decision by the CTP and to issue an L1A.
The trigger menu contains several low energy trigger items that need to be controlled in order not to exceed the maximum L1A rate of $100\,\mathrm{kHz}$. For this purpose, the trigger items can be given a prescale factor n, which means that only every n-th triggered event issues an L1A. However, prescaling a trigger item leads to a statistical bias in the trigger selection. For this reason, unprescaled triggers have an important role, especially the low-energy unprescaled trigger items are of great importance for physics data analysis.
In addition to the final trigger decision and the distribution of the L1A signal to all sub-detectors and Level-1 sub-systems, the CTP has the central task of transmitting various timing signals, such as the $40.08\,\mathrm{MHz}$ LHC clock, via the *Timing and Trigger Control* (TTC) system. In the course of the Phase-1 upgrade of the ATLAS detector, the TTC system also received significant changes, which are described in detail in Section 4.2.3.

3.2 The Data Acquisition System and the High Level Trigger

After the L1 system reaches a positive final trigger decision, the *Readout Drivers* (RODs) collect the event data from all the sub-systems and transmit them to the *Data Acquisition* (DAQ) system. The data are received on the *Readout system* (ROS), where they are stored again in the *Readout Buffers* (ROBs) and made available to the HLT via the *Data Collection Network*.
The HLT [32] describes the software-based second layer of the trigger system, which runs

on a large computer farm. It reduces the event rate further to about $1.5\,\mathrm{kHz}$ with the help of the RoI information received from the L1 system and more complex selection algorithms. After an event passed the HLT, it is written to mass storage.
During the Phase-1 upgrade of the ATLAS detector, the DAQ system and the HLT underwent certain modifications. In the readout, the new *FELIX* [49] board is introduced, linking the new Run 3 systems to the Data Collection Network. In addition, the new *Software Readout Driver* (SW ROD) [49] is implemented, which aggregates, buffers and processes the sub-system data before transmitting it to the HLT. The HLT has also received massive improvements, especially in the optimisation of the performance due to the switch to multithreaded software.

4 The Phase-1 Upgrade of the Level-1 Calorimeter Trigger

In preparation for Run 3, in which the LHC is operated at higher energy and instantaneous luminosity, the L1Calo trigger system underwent an extensive program of upgrades as part of the LS2. The new hardware, consisting among other things of a system of FPGA-based *Feature Extractor* (FEX) modules, is presented in Section 4.2. Before the installation of the new hardware in the electronic caverns of the ATLAS experiment, which will be described in Section 4.4, it was tested in the test rigs explained in Section 4.3. Besides this, the physics motivation of the upgrade will be discussed in the following, which is adopted from [36].

4.1 Physics Motivation

It is expected that by the end of Run 3, the ATLAS experiment will obtain a huge data set, larger than that of Run 1 and Run 2 combined, with an integrated luminosity of $300\,\mathrm{fb}^{-1}$. This offers, on the one hand, a large phase space for the search for physics *Beyond the Standard Model* (BSM) and, on the other hand, the possibility to improve the precision measurements of Higgs production and many other *Standard Model* (SM) processes. In order to provide suitable triggered events for this, the L1 trigger must first ensure a large variety for the search for BSM processes, with a high efficiency of the triggers needed for Higgs production as well as SM physics.
The trigger phase space is mostly occupied by the decays of electroweak particles, such as the W, Z, and Higgs bosons with masses between $80\,\mathrm{and}\,125\,\mathrm{GeV}$. The electroweak bosons decay mainly into leptons and jets, which lead to detected objects with a transverse momentum p_T larger than $30\,\mathrm{GeV}$. The most useful trigger items to search for these decay products are isolated single electron and muon triggers.
Accordingly, in order to continue to trigger these decay products with high efficiency during Run 3 at increased instantaneous luminosity, higher energies, and with the continued maximum L1A rate of $100\,\mathrm{kHz}$, the low-p_T L1 trigger thresholds of the respective single electron and muon triggers must be maintained, in addition to general improvements of the system during the Phase-1 upgrade. Keeping these unprescaled low-p_T L1 trigger items increases the datasets for high-precision as well as new physics measurements and will lead to high quality physics results with small systematic uncertainties.

The second main goal of the Phase-1 upgrade is to keep the ability to trigger electroweak particles that hadronically decay into τ leptons, jets or lead to a significant amount of missing transverse energy $E_{\mathrm{T}}^{\mathrm{miss}}$. In order to reliably trigger on the decayed particles, it is necessary to combine several trigger objects of the L1 system, since the signatures of the decay products are not as distinct as those of electrons and muons. In addition, the combination achieves manageable rates for the ATLAS TDAQ system, since the decay products could contain, for example, very low-p_{T} electrons, which would lead to a very high L1A rate when considered alone. To have sufficient bandwidth for the combined trigger items in the L1 system, it must be ensured that the single electron and muon trigger item rates are low with little loss of efficiency [36]. This goal of a low rate at high efficiency was targeted in the various studies for the first unprescaled single electron trigger of the Phase-1 system described in Chapter 10.

4.2 The Run 3 Level-1 Calorimeter Trigger

The legacy L1Calo system has successfully triggered on various objects in Run 1 and Run 2 and has significantly influenced the ATLAS data taking. With the expected higher instantaneous luminosities, higher centre-of-mass energies, the resulting harsher pile-up environment, and the still constant L1A rate of $100\,\mathrm{kHz}$ in the future, the system with its 7168 analogue input TTs needs to be upgraded to maintain the excellent performance of the L1Calo system in Run 1 and Run 2.

The approach taken in the upgrade was to increase the granularity of the information obtained by L1Calo, resulting in a higher resolution and the access to the lateral as well as longitudinal shower shapes. The additional information is then used in more advanced algorithms to improve the performance of the L1Calo trigger.

In order to achieve this, the front-end electronics of the LAr calorimeter was upgraded [50]. Apart from the pre-existing analogue path, the LAr calorimeter will deliver digital information to the new system of the L1Calo trigger with $10\times$ higher granularity in the form of so-called *Supercells* (SCs). As shown in Figure 4.1, a legacy TT with the coverage of $\Delta\eta \times \Delta\phi = 0.1 \times 0.1$ will be replaced for the EMB and the EMEC up to $|\eta| < 2.5$ generally by 10 SCs, except for the EMEC area without presampler coverage in which only 9 SCs are sent. In the Layer-0 (presampler) and in Layer-3 (backlayer) a region of 0.1×0.1 in the η-ϕ space will still be covered by one SC. In Layer-1 (frontlayer) and Layer-2 (middlelayer), the range of $\Delta\eta \times \Delta\phi = 0.025 \times 0.1$ is covered by one SC, resulting in four SCs each for one TT.

An overview of the new L1Calo Run 3 system is given in Figure 4.2. In the upper path,

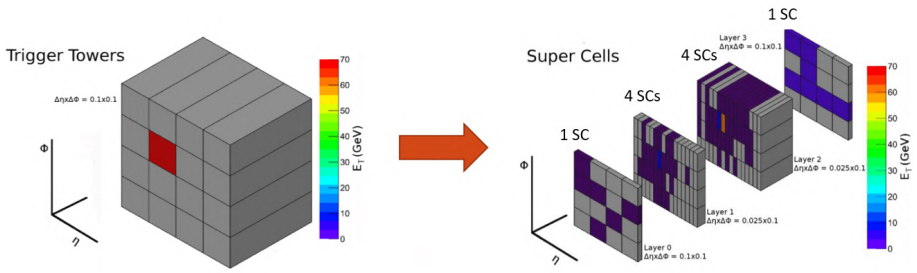

Figure 4.1: The figure shows the energy deposition of an electron at $70\,\mathrm{GeV}$ seen from the legacy L1Calo system within a $\Delta\eta \times \Delta\phi = 0.1 \times 0.1$ TT (left) and with the new Phase-1 system (right). Each of the Layer-0 (presampler) and the Layer-3 (backlayer) contributes one SC with a 0.1×0.1 granularity in the η-ϕ space to the overall LAr information for the L1Calo system, whereas the Layer-1 (frontlayer) and the Layer-2 (middlelayer) each contribute 4 SC with $\Delta\eta \times \Delta\phi = 0.025 \times 0.1$. Taken and modified from [50].

the digital SC information is forwarded to the three new FEX systems via the *Fibre-Optic Exchange* (FOX), which reorganises the data for the requirements of the FEX modules.
The Tile calorimeter, however, will undergo an upgrade after Run 3 and, as a result, will continue to transmit analogue TT signals via the lower legacy L1Calo path. In order to provide Tile information to the new FEX systems, the *Tile Rear Extension* (TREX) module, which is discussed in more detail in Chapter 5, was introduced. The modules are installed as a physical extension of the PPM in both Tile crates and send digital copies of the E_{T} values, intended for the legacy JEP as well as CP system, optically to the new FEX systems. At the start of Run 3, the TREX also allowed parallel running of the old legacy and the new Run 3 system, while the new one continued to be commissioned. During this time, early successful data taking by the legacy system was ensured. Furthermore, parallel operation was used for rapid debugging and comparisons between the two systems.
In addition to the FEXes, the TREX, and the FOX, the new Run 3 system consists of a new topological trigger called *Phase-1 Level-1 Topological Trigger* (Phase-1 L1Topo), of the *Topo Fibre-Optic Exchange* (Topo FOX), which arranges the output of the FEX systems for the needs of Phase-1 L1Topo, and of the aforementioned new readout system consisting of FELIX and SW ROD. The interface to the FELIX of eFEX, jFEX and Phase-1 L1Topo is formed by the new *ATCA Switch* (HUB) and *Readout Driver* (ROD) modules, which on the one hand forward TTC information received from the FELIX to the mentioned L1Calo modules and on the other hand buffer the readout data and forward it to the FELIX. A specially designed *FEX Test Module* (FTM) was produced for testing the FEX modules before installation.
Additionally, the TTC system of all sub-systems of the ATLAS experiment and accordingly also of the L1Calo system was upgraded in the course of the Phase-1 upgrade.

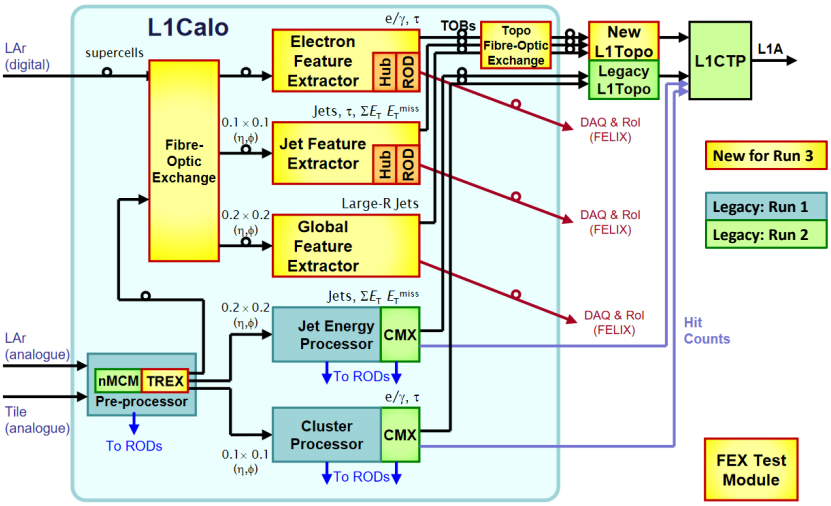

Figure 4.2: L1Calo system architecture during Run 3. The new Phase-1 components are shown in yellow/orange. At the start of Run 3, the legacy system, illustrated in blue/green, will continue to run in parallel with the new system. Taken and modified from [36].

4.2.1 The Feature Extractor Modules

The FEX system consists of three different types of modules, the *Electron Feature Extractor* (eFEX), the *Jet Feature Extractor* (jFEX), and the *Global Feature Extractor* (gFEX). All three are designed as *Advanced Telecommunications Computing Architecture* (ATCA) boards with different FPGAs and high-speed optical transceivers. The modules, similar to the legacy CP and JEP systems, run algorithms to determine particle candidates of interest using the calorimeter input, calculate energy sums and forward the resulting information as TOBs. Studies on the expected performance of the FEX algorithms have been carried out with the L1Calo offline software, which are considered in more detail in Section 7.4.

4.2.1.1 The Electron Feature Extractor

The entire eFEX [51] system consists of 24 ATCA modules within two ATCA shelves. It covers the range of $|\eta|$<2.5 with full coverage in ϕ and receives the full granularity SC information from the LAr calorimeter as well as the $\Delta\eta \times \Delta\phi = 0.1 \times 0.1$ TTs from the Tile calorimeter via the TREX modules. The eFEX system is the equivalent of the legacy CP system and also attempts to identify electron, γ or τ candidates. It accesses the full granularity of the upgraded LAr calorimeter to retrieve lateral as well as longitudinal shower shape information and increase the trigger efficiency while reducing the L1A rate. First, the e/γ algorithm, also called EM algorithm, which is responsible for identifying

electrons and γ candidates, performs a seed finding to search for a local energy maximum from the four central SCs of a 0.3 $\times$ 0.3 ($\eta \times \phi$) window in Layer-2 (shown as the black box in Figure 4.3(a)) by comparing with its neighbours to determine the seed of the TOB. When a local maximum and consequently the seed of the TOB has been found, the associated energy deposition $E_{\text{T,TOB}}$ is calculated in the following way

$$E_{\text{T,TOB}} = E_{\text{T,Clu1}} + E_{\text{T,Clu2}} + E_{\text{T,Clu0}} + E_{\text{T,Clu3}}, \tag{4.1}$$

with $E_{\text{T,Clu1}}$ and $E_{\text{T,Clu2}}$, the energy sums of the 3 $\times$ 2 cluster area of SCs in Layer-1 and -2, respectively, centred on the local energy maximum and its neighbour in ϕ that has the next highest E_{T} (shown exemplary as the yellow cluster area in Figure 4.3(a) for Layer-2). In addition, for the TOB calculation the energy sums, located at the same area, of the 1 $\times$ 2 cluster of SCs in Layer-0 and -3, $E_{\text{T,Clu0}}$ as well as $E_{\text{T,Clu3}}$, respectively, are used. The calculated $E_{\text{T,TOB}}$ value is added to the TOB information.
As with the CP system, there are also isolation parameters in the eFEX e/γ algorithm implemented to ensure unique identification of e/γ particles and to distinguish the candidates from the dominant jet background.
One of the isolation parameters is R_η, which is the equivalent to the electromagnetic isolation in the CP system. In the case of the eFEX, it is calculated using only transverse energies of Layer-2 and is defined as

$$R_\eta = \frac{E_{\text{T,Clu2}}}{E_{\text{T,Env2}} + E_{\text{T,Clu2}}} > R_{\eta,\text{thres,L/M/T}}, \tag{4.2}$$

with the already described $E_{\text{T,Clu2}}$ energy sum of the 3 $\times$ 2 cluster area of SCs in Layer-2 and the $E_{\text{T,Env2}}$ energy sum of the 7x3 environment area of SCs in Layer-2 around the cluster area, shown in blue in Figure 4.3(a). The R_η isolation ensures the narrow isolated showers characteristic of e/γ candidates, comparing the value to three programmable thresholds $R_{\eta,\text{thres,L/M/T}}$ each representing one of the working points *Loose* (L), *Medium* (M), and *Tight* (T). The condition is satisfied, if $R_\eta > R_{\eta,\text{thres,L/M/T}}$.
The second isolation parameter is the cluster width w_s, which also exploits the narrow shower characteristic and uses only the transverse energy E_{T} information of Layer-1. It is defined as

$$w_s^2 = \frac{\Sigma E_{\text{T},i}(i - i_{\text{max}})^2}{\Sigma E_{\text{T},i}} < w_{s,\text{thres,L/M/T}}^2, \tag{4.3}$$

where i spans the η range of five SCs in Layer-1 centred around the seed SC position, $E_{\text{T},i}$ is the transverse energy of the corresponding SC i, and $(i - i_{\text{max}})$ is the difference

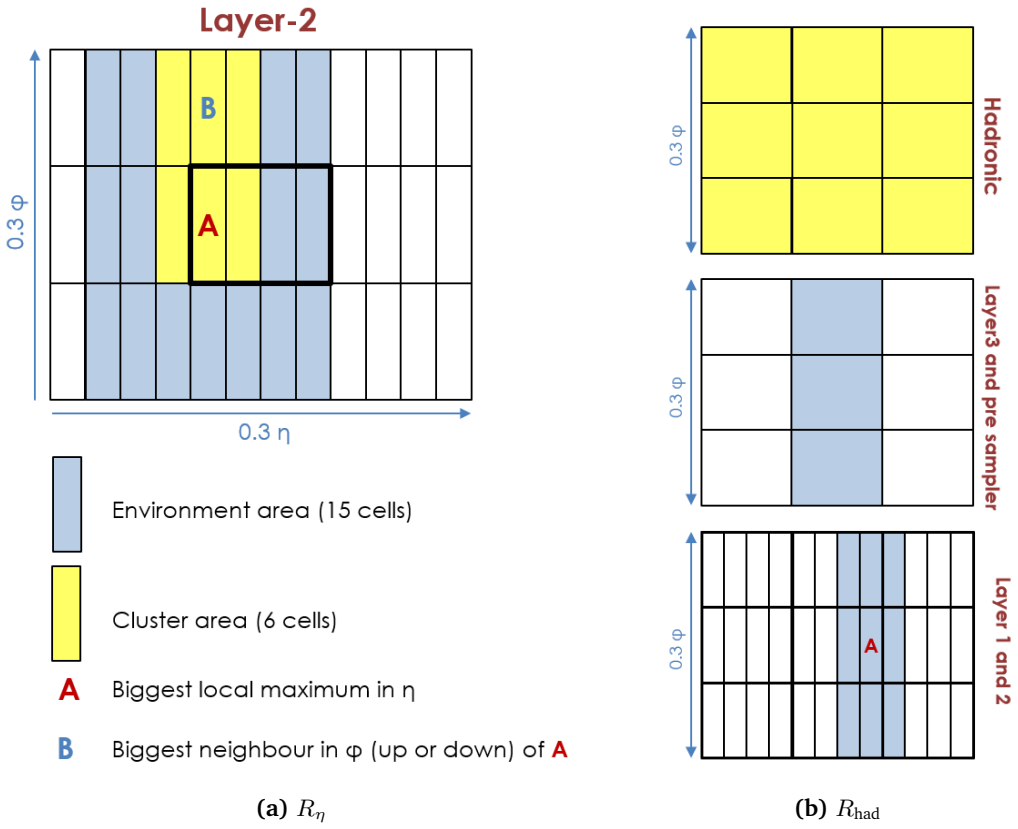

(a) R_η **(b)** R_{had}

Figure 4.3: Illustration for the calculation of the eFEX isolation parameter R_η and R_{had}. Figure (a) shows a visualisation of the R_η parameter, whereby only SCs in Layer-2 and in the environment as well as cluster area are used for the calculation. In addition, the seed finding is indicated. Figure (b) illustrates the calculation of R_{had} with SCs from all layers. Taken from private communication [52].

between that SC i and the seed SC i_{max}. The calculated value is then again compared against three programmable thresholds $w^2_{s,\text{thres,L/M/T}}$ with satisfaction of the condition if $w_s^2 < w^2_{s,\text{thres,L/M/T}}$.

The last isolation parameter of the e/γ algorithm is the hadronic isolation R_{had}. Similar to the legacy CP system, the hadronic isolation condition exploits the fact that e/γ candidates deposit almost all of their energy in the electromagnetic calorimeter. Here, R_{had} is defined as

$$R_{\text{had}} = \frac{E_{\text{T,had}}}{E_{\text{T,had}} + E_{\text{T,0}} + E_{\text{T,1}} + E_{\text{T,2}} + E_{\text{T,3}}} < R_{\text{had,thres,L/M/T}}. \tag{4.4}$$

The energy values used are shown in Figure 4.3(b). $E_{\text{T,had}}$ describes the energy sum of the 3 $\times$ 3 TT in the hadronic calorimeter, $E_{\text{T,1}}$ and $E_{\text{T,2}}$ are the sums of the 3 $\times$ 3 SCs

in Layer-1 and Layer-2, respectively, and $E_{\mathrm{T},0}$ as well as $E_{\mathrm{T},3}$ are summed of the 1×3 SCs in Layer-0 and Layer-3, respectively. All the areas of cells are centred around the seed. The calculated R_{had} values are compared to three thresholds and the condition is satisfied if $R_{\mathrm{had}} < R_{\mathrm{had,thres,L/M/T}}$. The isolation parameters described are used in the studies considered in Chapter 10.
The τ algorithm, which is responsible for identifying τ candidates, operates, like the e/γ algorithm, with a 0.3×0.3 ($\eta \times \phi$) window to find a seed. However, the actual seed finding algorithm is divided into two steps due to the partial energy deposition of the τ particle in the hadronic calorimeter. In the first stage, the main seed finder searches for a local energy maximum in 0.1×0.1 TT, which are composed of the energies of all electromagnetic and hadronic layers. In the second step, the "little" seed finder uses the same procedure as the e/γ algorithm to find a SC seed in Layer-2. The corresponding TOB transverse energy $E_{\mathrm{T,TOB}}$ is calculated as the sum of the energy in the 5×2 SCs in the fine Layer-1 and -2 centred around the seed and the sum in the 3×2 cells in the coarse Layer-0 and -3 as well as the hadronic layer with the seed as the centre.
Two isolation parameters were also introduced for the τ algorithm. The τ jet veto condition helps, similar to R_{η}, to distinguish τ candidates from jets on the basis of the narrower shower shape. The second condition, the hadronic fraction, helps to differentiate e/γ and τ candidates based on the energy fraction of τ particles deposited in the hadronic calorimeter.

4.2.1.2 The Jet Feature Extractor

The jFEX [53] system is the equivalent of the legacy JEP and searches for jets, computes the missing transverse energy $E_{\mathrm{T}}^{\mathrm{miss}}$ and the total transverse energy $E_{\mathrm{T}}^{\mathrm{tot}}$, and additionally introduces a determination of τ as well as forward electron candidates. It covers the complete calorimeter range up to $|\eta| < 4.9$ and consists of 6 ATCA modules within one ATCA crate. The jFEX modules receive finer granularity calorimeter information from LAr and Tile than the JEP system with typical 0.1×0.1 ($\eta \times \phi$) instead of 0.2×0.2 in the barrel region with the granularity becoming coarser and η dependent in the forward region.
The jFEX *Small-Radius Jet* algorithm [54] is based on a sliding window with a size of 0.9×0.9 ($\eta \times \phi$). The procedure is shown in Figure 4.4(a). In the first step, sums of 0.3×0.3 sections are computed within the 0.9×0.9 window to form seeds, as single jets are expected to deposit a large fraction of their energy within the corresponding seed. Afterwards, a local maximum of the sums is sought by comparing the 0.3×0.3 seeds

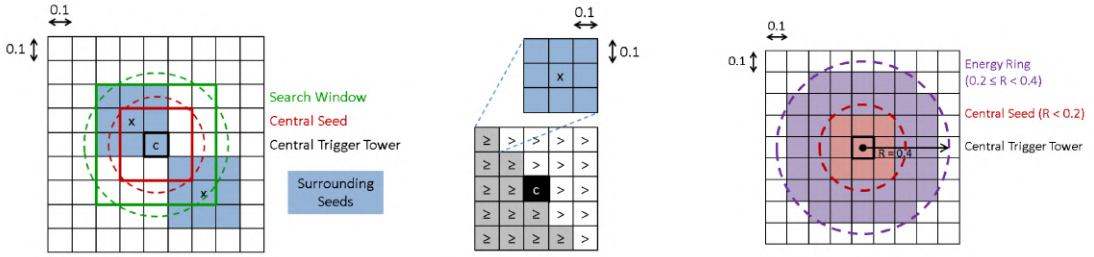

(a) jFEX Small-Radius Jet Seed **(b)** jFEX Small-Radius Jet Energy

Figure 4.4: Illustration of the jFEX seed finding and energy calculation of the small-radius jet algortihm. Figure (a) shows the determination of the seed of a small-radius jet with a 0.9×0.9 ($\eta \times \phi$) sliding window. Figure (b) visualises the subsequent calculation of the energy of the jet belonging to the determined seed. Taken from [54].

inside a 0.5×0.5 window.

In parallel to the seed finding algorithm, jet energy sums are already calculated for each individual TT. This is done by summing up the energies of the TTs surrounding the tower under consideration in a radius of $\Delta R < 0.4$. The procedure is shown in Figure 4.4(b).

The TOBs of small-radius jet candidates are then assembled using the η-ϕ coordinates from the seed finding algorithm and the corresponding jet energy sums from the second parallel running procedure.

The second implemented jFEX algorithm searches for τ and forward electron candidates. The algorithm uses information of a larger area of 1.7×1.7 ($\eta \times \phi$) around τ clusters than the eFEX (0.3×0.3). The results of both τ algorithms will be merged in the Phase-1 L1Topo to combined τ trigger items implemented in the CTP Phase-1 trigger menu. The procedure of the jFEX τ algorithm is similar to the jFEX jet algorithm. However, the parallel calculation of the energy sum is omitted as the energy sum of the found seed for τ candidates is used directly. The jFEX τ algorithm runs as the eFEX algorithm with calorimeter information up to $|\eta| < 2.5$. In the range of $2.5 < |\eta| < 4.9$ where the coverage of eFEX is no longer provided, the jFEX searches for forward electrons with the same algorithm as for the τ candidates.

In addition to determining jets, tau and forward electron candidates, the jFEX system calculates the two global sums, the total transverse energy $E_{\mathrm{T}}^{\mathrm{tot}}$ and the missing transverse energy $E_{\mathrm{T}}^{\mathrm{miss}}$ and stores the results in individual TOBs.

4.2.1.3 The Global Feature Extractor

The gFEX [55] system consists only of one ATCA module housed in one ATCA crate, which is handling the whole calorimeter detector data and is therefore capable of determining

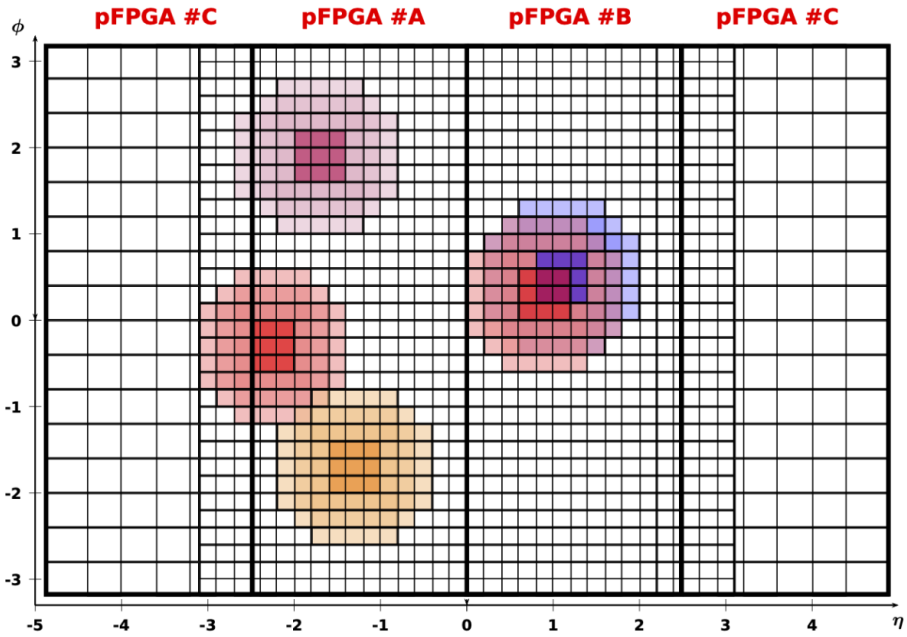

Figure 4.5: Illustration of an event with different potential large-radius jet candidates, which are allowed to overlap and also span over several FGPAs of the gFEX. Taken from [55].

large jet candidates. It receives SC information from LAr as well as TT information from Tile and in a first step builds so-called *gTowers* with a typical size of $\Delta\eta \times \Delta\phi$=0.2 $\times$ 0.2. The division of the entire calorimeter region into gTowers as the smallest squares is shown in Figure 4.5. Based on the gTowers, small- and large-radius jet candidates and the missing transverse energy $E_{\mathrm{T}}^{\mathrm{miss}}$ are determined.

The small- and large-radius jet algorithm forms so-called *gBlocks* from typically 3 $\times$ 3 gTowers and compares the energy sum to a programmable E_{T} threshold to determine jet seeds, which are shown as the centre 3 $\times$ 3 window in Figure 4.5. The determined seeds already correspond to the small-radius jet candidates, whereupon their information is packed into TOBs after fulfilling further global detector conditions.

The gBlocks are then used by the large-radius jet algorithm as a central seed, typically to form the energy sums of 69 surrounding gTowers, as illustrated in Figure 4.5. Once the large-radius jet candidate is formed, global detector conditions are checked again before a TOB is created.

In addition to the jet algorithms, the missing transverse energy $E_{\mathrm{T}}^{\mathrm{miss}}$ is calculated by the so-called *Jets-without-Jets* algorithm within the gFEX using the already determined gTowers and gBlocks, which information is then packed into a TOB.

The gFEX in general performs similar candidate identifications as the jFEX, but with

a slightly different global approach. This overlap of roles between the different FEX modules can be identified throughout the Phase-1 L1Calo system, ultimately allowing comparisons to be made between systems to simplify commissioning and ensure the best possible results.

4.2.2 Phase-1 Level-1 Topological Trigger

Similar to the legacy L1Topo introduced in Run 2, the new Phase-1 L1Topo [56] performs topological algorithms based on event topologies, but will additionally add the multiplicity functionality of the Run 2 CMXs. The entire Phase-1 L1Topo system is implemented as three ATCA modules within an ATCA crate and receives the results from the eFEX, jFEX, and gFEX systems as TOBs as well as muon TOBs from the new MUCTPI. The algorithm and multiplicity results are then forwarded to the CTP.

4.2.3 ATLAS Local Trigger Interface

During the Phase-1 upgrade, the TTC system of the ATLAS experiment was also revised. The four different modules, *Local Trigger Processor* (LTP), *Local Trigger Processor Interface* (LTPI), *TTC VMEbus Interface* (TTCvi), and *TTC Encoder/Transmitter* (TTCex), which previously performed the task of broadcasting the TTC signals from the CTP to all subsystems of the ATLAS experiment, were replaced with one unique module, the *ATLAS Local Trigger Interface* (ALTI) [57]. The ALTI has the task of reducing the complexity of the system, replacing the previous modules, which are running out of spares, and continuing to forward the TTC signals from the CTP, such as the LHC clock or the L1As, to the various sub-systems. The replacement of the four modules represented a serious intervention in the TTC system, which among other things led to a resulting change in the entire legacy timing calibration and thus to a necessary recommissioning as well as recalibration of the legacy system, which is examined in more detail in Chapter 8.

4.3 Phase-1 Test Rigs

In order to test the new hardware of the Phase-1 upgrade, in addition to the test systems at the individual institutes responsible for the respective components, there are two test rigs at CERN, the *B104 Legacy Test Rig* and the *Surface Test Facility* (STF). At these, combined tests were carried out with partly earlier as well as production versions of the

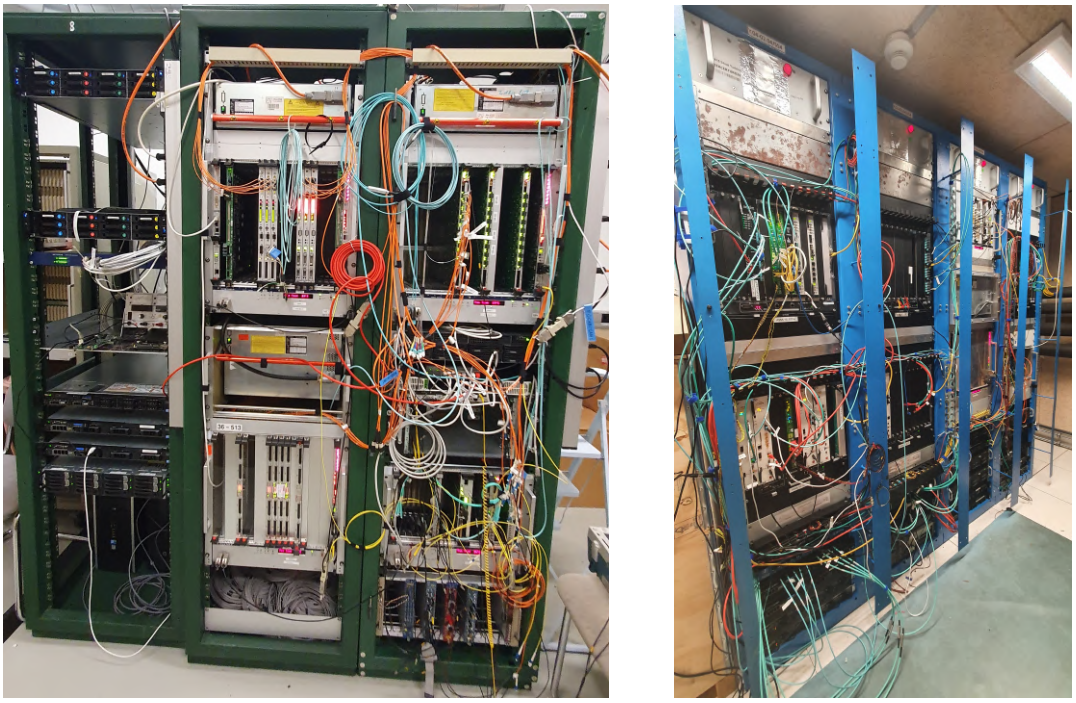

(a) B104 Legacy Test Rig **(b)** Surface Test Facility

Figure 4.6: Images of the two CERN L1Calo test rigs. The B104 Legacy Test Rig, shown in Figure (a), was heavily used to implement the TREX module and the ALTI, with the STF in Figure (b) being specifically designed for commissioning the Phase-1 upgrade.

Phase-1 hardware, firmware, and software. Both test rigs were essential for the development of the Phase-1 upgrade components within a combined environment that closely resembles the conditions inside the actual L1Calo system within the electronic caverns of the ATLAS experiment. The calorimeter or muon signals are not available as input to the test rigs, which is why the various sub-components have playback and spy memories to insert generated data into the system and to capture the results of calculations at various points. The test rigs are shown in Figure 4.6.

4.3.1 The B104 Legacy Test Rig

The B104 Legacy Test Rig was commissioned before Run 1 to test the former new legacy L1Calo components. Over time, the upgrades for Run 2 were also checked in the test rig, as well as parts of the new hardware, firmware, and software for the Phase-1 upgrade. The test rig consists of four VME crates, one containing the PPMs, one the CP, JEP and CMXs, the third containing RODs and the last a dedicated TTC system. In addition, certain IT infrastructure is required for communication and monitoring.

For the Phase-1 upgrade, a TREX module was added to test the functionality within the legacy system and to check the forwarding of data to the CP and JEP system. In addition, the test rig was used to develop the implementation of the TREX monitoring within the legacy monitoring architecture, which is described in Section 6.2.
Due to the dedicated TTC system, it was also a perfect place to test the ALTI introduced modifications of the TTC system and to prepare it for the installation in the ATLAS electronic cavern.

4.3.2 Surface Test Facility

The STF has been specifically set up for the Phase-1 upgrade and aims to provide an optimal development environment for combined testing and commissioning of the individual sub-systems introduced in Run 3. Thus, a complete run through the new L1Calo Run 3 system was set up to perform internal L1Calo system-level tests as well as checks for integration with neighbouring systems, such as the new LAr calorimeter or also L1Muon. The goal of each system was to show full functionality of hardware, firmware, and software within the STF. The test environment was essential for the development of the TREX monitoring, described in Section 6.2, and the TREX online simulation, the subject of Section 7.2.
The STF consists of four water-cooled racks containing a total of 5 ATCA shelves. Three of these house the jFEX, Phase-1 L1Topo, eFEX, and gFEX modules, the latter two sharing a crate. The other two are occupied by the *LATOME*, which forms the interface to the new LAr system, and the MUCTPI as the interface to the L1Muon that is used for Phase-1 L1Topo tests. In addition, the L1Muon system takes up one of the three VME crates installed in the four racks. The other two VME crates house PPMs with connected TREX modules to generate Tile calorimeter signals on the one hand, and a separate TTC system that supplies the STF with trigger and timing signals on the other. The test rig is complemented with three dedicated FELIX servers and an IT infrastructure to control and monitor the components.

4.4 Phase-1 Installation

After testing within the test rigs and several iterations of hardware, firmware, and software versions, the new Phase-1 hardware was ready to be installed within the ATLAS electronic caverns, namely USA15. It took almost 2 years from the first installation of the ATCA shelves in October 2020 to the last installed eFEX board in September 2022. An

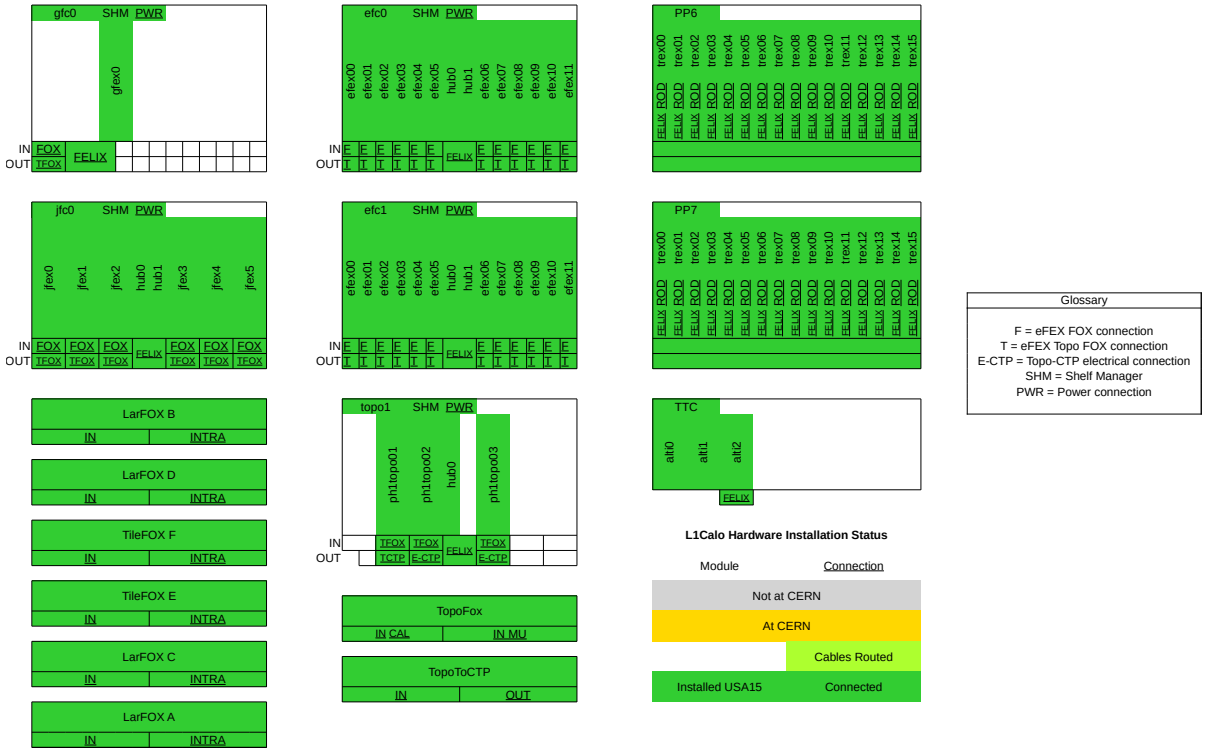

Figure 4.7: Overview of the installation status of the L1Calo Phase-1 hardware and infrastructure in USA15. The figure shows the completed status of the installation in September 2022 after the last eFEX ATCA crate has been completely filled with eFEX modules. Taken and modified from private communication [58].

overview of the installed hardware and the required connections is given in Figure 4.7. In addition to the listed components, further IT infrastructure was installed to control and monitor the Phase-1 hardware.

With the installation of each component, the next step of the commissioning work began and a number of individual functionality, connectivity, integration, and system tests were carried out before moving on to combined tests, first in the L1Calo and then in the ATLAS environment.

5 The Tile Rear Extension Module

The TREX modules are designed to provide digitised hadronic transverse energies E_{T} of the Tile calorimeter to the new FEX systems. In addition, the TREX modules continue to forward Tile signals to the legacy system, so that at the start of Run 3 and for commissioning purposes of the new FEXes, both systems, legacy and Phase-1, are able to run in parallel.
In this chapter, an overview of the TREX system and the associated changes to the legacy system are given. Afterwards, the three different data paths, the real-time, the readout, and the monitoring data path are discussed. This chapter follows the information given in [11, 43].

5.1 Overview

The TREX [11, 43] module is designed as a physical extension of the PPM and is connected to the backplane of the PPM within the VME crate. It was installed only for the two VME crates that process the TT signals of the Tile calorimeter, which is why a total number of 32 TREX modules were required. After three development iterations, a total of 40 TREX modules of the production version, including spares, were produced. A functional overview of the TREX as the extension of the PPM is given in Figure 5.1.
The TREX consists of the three main processing units the *Preprocessor Data Collector* (PREDATOR) FPGA, four *Data-In-Out* (DINO) FPGAs, and the *ZYNQ Ultrascale+ Multi-Processor System-On-Chip* (ZYNQ MPSoC). Besides the FPGAs mentioned, additional configuration and power supply components as well as optical transmitter modules are located on the TREX.
The data paths of the TREX module can essentially be reduced to three main paths, the real-time data path, shown as red and orange in Figure 5.1, the readout data path, shown in blue, and the monitoring data path, indicated in green.
The TREX as the physical extension of the PPM also required infrastructure, hardware, and firmware changes to be made to the legacy system. In order to accommodate the TREX modules in the two Tile VME crates of the PPMs, the crate had to be modified and the legacy *Rear G-Link Transmitter Modules* (RGTMs), which formed the interface to the DAQ system, had to be removed. The functionality of the RGTMs was transferred to the TREX.
The PPMs themselves underwent some hardware changes. First, the PPM's *LVDS cable*

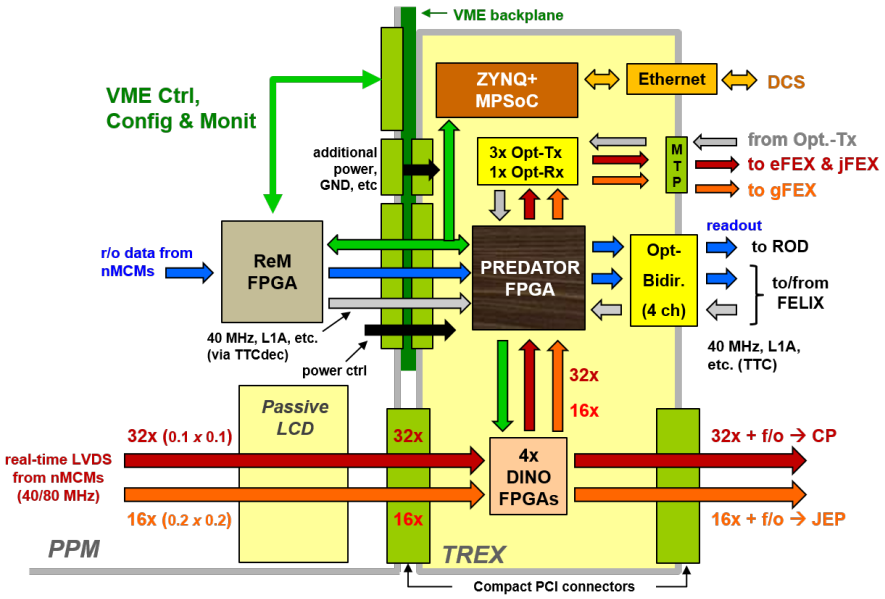

Figure 5.1: Schematic overview of the TREX module as a physical extension of the PPM. Besides the most important components of the TREX module, the PREDATOR, the DINOs and the ZYNQ, the three data paths, the real-time data path to the legacy system and to the new FEX systems (red and orange), the readout data path to the legacy ROD as well as to the FELIX (blue), and the monitoring data path via the ZYNQ (green), are shown [43].

driver (LCD) card was replaced with a passive bridge (pLCD). The function of the LCD card to drive the LVDS streams of the nMCM to the CP and JEP system was moved to the TREX. A second change involved the removal of resistors in the path of the differential signal in order to reduce the associated limitation of the bandwidth of the LVDS signals and thus to be able to work with higher transfer rates in the future, if necessary. In addition, the PPMs were equipped with an additional external wire to forward a signal that reflects the power status of the PPM to the TREX.

Besides the hardware changes, the firmware of the PPMs was also adapted. The firmware of the ReM, which had taken over the control of the nMCMs, the rate metering, and the collection as well as processing of the data read out by the DAQ system during Run 2, underwent the biggest changes. The readout data processing was moved to the TREX to free up space on the ReM FPGA to establish the communication infrastructure between the *Single Board Computer* (SBC), which serves as a VME controller, inside the crate and the TREX. The new firmware of the *Extended Readout Manager* (ExtReM) makes it possible to receive the VME commands originating from the SBC, process and forward them to the TREX. In addition, new management logic circuits, new status and error registers for the TREX, and a reorganisation of the internal clock distribution have been added

to the new firmware design. Another change concerned the firmware of the *Complex Programmable Logic Device* (CPLD) on the PPM, which repurposed the programming and configuration signals previously used for the FPGAs of the LCD card and uses them for the TREX FPGAs.

5.2 The Real-Time Data Path

The real-time data path of the TREX module, shown in red and orange in Figure 5.1, starts with the 48 LVDS streams from a PPM, which are described in more detail in the Section 3.1.1.2. 32 of the inputs carry 0.1×0.1 E_{T} values intended for the CP system, with the other 16 carrying 0.2×0.2 jet sums for the JEP system.
The input signals enter the TREX from the backplane connector of the PPM and are routed to the input of the four DINO FPGAs. The first two of the FPGAs take care of duplicating and forwarding the signals intended for the CP system, while the other two handle the signals of the JEP system. After the duplication, the signal copies for the CP and JEP system are forwarded via LVDS cables, similar as previously with the legacy LCD card. The remaining signal copies of the first two FPGAs with 0.1×0.1 E_{T} information, intended for the eFEX and jFEX modules, and the signal copies of the other two FPGAs with 0.2×0.2 granularity, intended for gFEX, are passed on to the PREDATOR FPGA.
Once they arrive at the PREDATOR, the signals are first deserialised to single-ended signals. Then the BCMUXed copies obtained from the LVDS stream for the CP system and intended for eFEX and jFEX are demultiplexed. For all copies, the odd parity bit is checked continuously, and a *link error* flag is raised as well as forwarded to the FEX systems in case of possible discrepancies.
Before the 8-bit E_{T} values and the 9-bit jet sums can be forwarded via optical fibres running at $11.2\,\mathrm{Gbit\,s^{-1}}$ from the TREX to the FEX systems, they are packed together for each fibre according to the formats shown in Figure 5.2. One fibre forwards 16 E_{T} values for eFEX as well as jFEX and 16 jet sums for gFEX.
For eFEX, the data format contains 10-bit data fields, whereas for jFEX and gFEX 12-bit data fields are used. The 8-bit E_{T} values or 9-bit jet sums take up the lower 8 or 9 bits of the data words, with the next higher bit being occupied by the already mentioned link error flag. The remaining bits of the data fields serve as a backup for any additional information that may be required in the future. The data words are ordered by increasing PPM digital channel number for eFEX and jFEX, while the increasing nMCM number is used for gFEX. In addition, in the data formats, an 8-bit *comma character* (K28.5), the 12-bit *bunch crossing identification* (BCID) number, and a 9-bit *cyclic redundancy check*

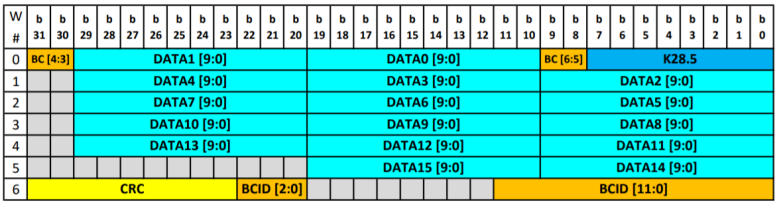

(a) eFEX real-time data format

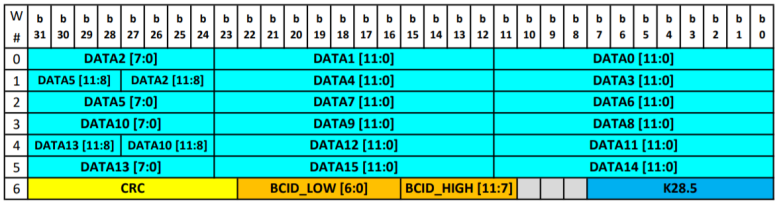

(b) jFEX real-time data format

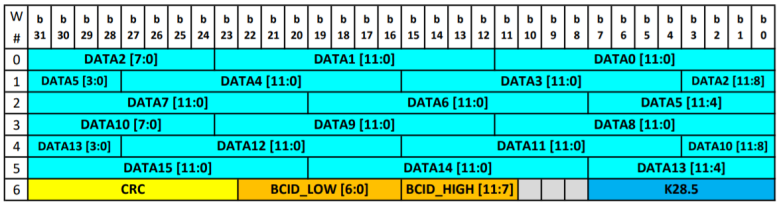

(c) gFEX real-time data format

Figure 5.2: The real-time output data formats from TREX to the three different FEX systems. The real-time data intended for the FEX systems are packed into the data formats shown within the firmware of the PREADATOR FPGA. They contain besides the E_{T} values an 8-bit comma character (K28.5), the 12-bit bunch crossing identification (BCID) number, and a 9-bit cyclic redundancy check (CRC) code. Furthermore, the formats were implemented in the TREX online simulation. Taken from [43].

(CRC) code are added for alignment, synchronisation, and error detection purposes. The formatted data is then serialised at $11.2\,\mathrm{Gbit\,s^{-1}}$ and forwarded from the TREX using three of the four installed optical transmitter modules, one for each FEX system, with the number of links used differing for each system.

A PPM with connected TREX covers the $\Delta\eta\times\Delta\phi = 0.4 \times 1.6$ region of the Tile calorimeter. For eFEX and jFEX, the TREX transmits 16 8-bit E_{T} values on one optical fibre with a coverage of 0.4×0.4 in the η-ϕ space, while for gFEX, a single optical fibre is sufficient to receive the 16 processed 9-bit jet sums of a PPM.

When forwarding to the eFEX, the TREX has to provide one, two or even four copies of the fibre data, depending on the calorimeter region, as several eFEX modules overlap in their coverage, thus resulting in up to 12 used optical links with connected fibres between TREX and eFEX. For the routing to jFEX, 12 links are always used, as three copies of the fibre data are forwarded regardless of the calorimeter region. As mentioned before, one

fibre link is sufficient for gFEX and the 16 jet sums, although another fibre being realised as a spare connection from TREX to gFEX.
The described sequence of the real-time data path of the TREX was implemented in parts in the L1Calo online simulation and is considered in more detail in Section 7.2.

5.3 The Readout Data Path

The starting point of the readout path, shown in blue in Figure 5.1, are the memory buffers within the nMCMs, which are temporarily filled with event data. After an incoming L1A signal from the CTP to the PPM, the ReM FPGA initiates the readout of the associated data in the memory buffers that contain the number of ADC slices, the ADC values, the calculated E_{T} values, error flags, and pedestal correction values.
In the case of Run 2, the event data was then processed on the ReM FPGA and passed to the RGTMs on the back of the PPM, which formed the interface to the DAQ system. For the Tile PPM crates in Run 3, the event data processing was transferred to the PREDATOR FPGA, the RGTMs were removed, and the TREX acts as the interface to the DAQ system. In contrast to the Run 2 system, however, two different types of interfaces to the DAQ system are implemented on the TREX, which are initially used in parallel.
The first is to the legacy ROD via one optical link running at $800\,\mathrm{Mbit\,s^{-1}}$, using the legacy *G-Link format*, described in Section 3.1.1.2, for the readout data.
The second interface is to the new FELIX system introduced in Run 3 via an optical link at $9.6\,\mathrm{Gbit\,s^{-1}}$. All new systems use the FELIX, as the RODs will no longer be supported in the future, and ATLAS as a whole will therefore move to a uniform readout infrastructure. For this reason, at a certain point, the readout via the RODs will be discontinued, and only the readout via the FELIX will be used. The FELIX receives the data from the TREX and forwards it to the SW ROD, where the data is separated from the additional header and trailer, leaving the event data for the ATLAS event builder to process.
The initial FELIX readout format, shown in Figure 5.3, uses the same G-Link format for the event data as the legacy system with an additional TREX header and trailer. This choice was made in order to re-use existing software for the legacy format and thus save additional work. The TREX header contains geographical information of the TREX module, such as the *Slot ID* and *Crate ID*, its own identifier with the *Module ID*, but also the current readout configuration with the number of read out PPM ADC and LUT values. The next header words include various information about the read out event, such as the *Level-1 ID*. Finally, the attached TREX trailer provides variables for error detection and diagnosis.

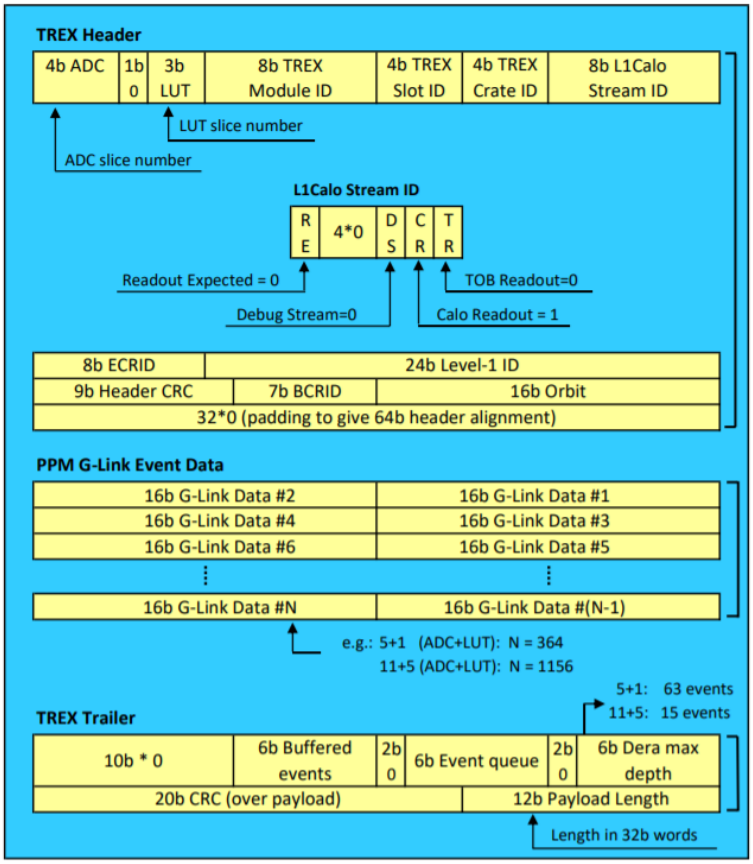

Figure 5.3: Initial readout format from TREX to FELIX. The read out data already formatted in the legacy readout G-Link format is packed together with a TREX header and trailer in the PREDATOR FPGA. The header contains geographical information of the TREX module, its own identifier, the readout configuration, and diverse information about the read out event. The trailer complements the format with variables for error detection and diagnosis. Taken from [43].

However, while further compression of the event data was performed on the legacy ROD to reduce the size of the ATLAS events, this step also had to be performed on either the TREX or the SW ROD. The shown initial format variant foresaw compression on the SW ROD and was used for initial testing of individual TREX modules and the online simulation, which is discussed in more detail in Section 7.2. However, the compression on the SW ROD turned out to be a heavy CPU load after the tests were extended to fully equipped TREX crates and therefore reduced the readout performance of the TREX. Consequently, it was decided to perform the compression on the TREX and forward the compressed data to the FELIX. The new format retains the header and trailer of the initial one and uses the so-called *S-Link format*, which consists of a dedicated header with the compressed data (more details in [11]), instead of the legacy G-Link format.

5.4 The Monitoring Data Path

The third main data path of the TREX is the monitoring data path to monitor, control, and archive the operational parameters such as voltages, currents and temperatures of the TREX to ensure safe operation. For this purpose, the measured data from the various components of the TREX must first be collected and then forwarded to the ATLAS *Detector Control System* (DCS), which is the topic of Section 6.1. Both functionalities are running in parallel and are handled by the core component of the TREX DCS, the Zynq MPSoC. It uses first the TREX's *Inter-Intra Circuit protocol* (I2C) interface that is shown with all connected components in Figure 5.4, to collect monitoring data at a programmable frequency of $0.5\,\mathrm{Hz}$, which is sufficient for DCS purposes. After collection, the data is packed together and stored temporarily in a buffer. In the second step, the data within the buffer is read, unpacked and the information is made available to the so-called *Open Platform Communications Unified Architecture* (OPC UA) server [59], which runs on the processor of the Zynq and is discussed in more detail in Section 6.2.1. Any OPC UA client can subscribe to the server via Ethernet and thus access the information provided. The clients are integrated in the TREX DCS project as part of the ATLAS DCS and therefore enable the monitoring of the TREX's operational parameters. In addition, actions such as powering up or down of the TREX board can be issued via the DCS and transferred to the Zynq via Ethernet. Further detailed explanations of the implementation within the ATLAS DCS is the subject of Chapter 6.

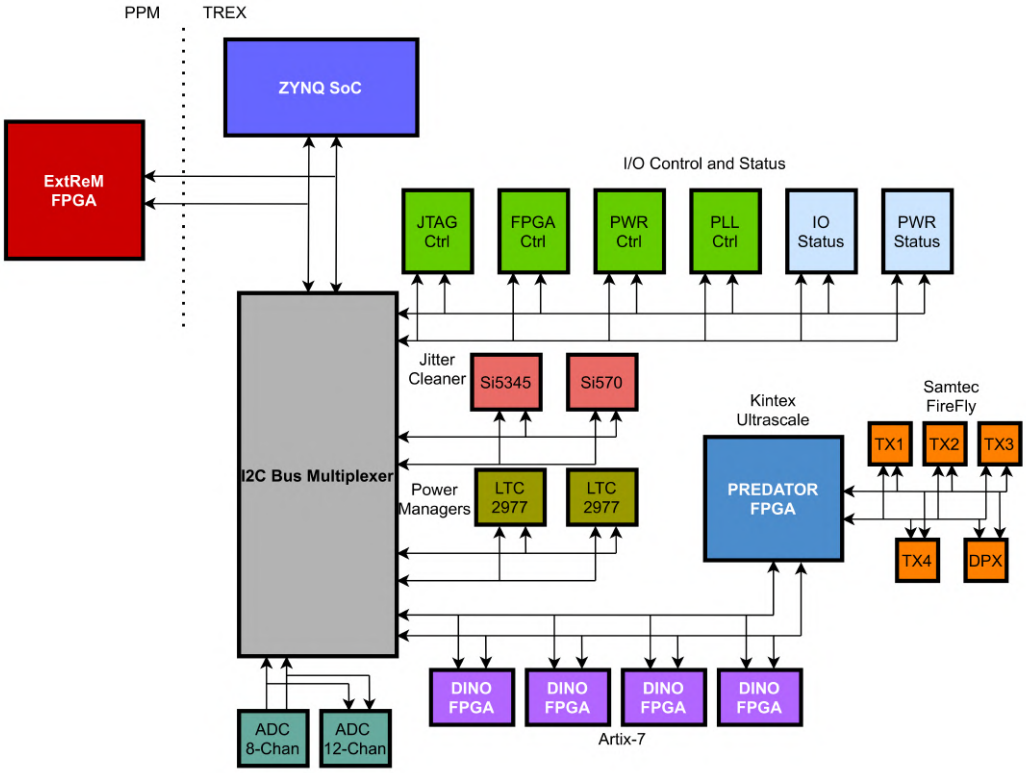

Figure 5.4: Schematic overview of the TREX I2C system. The illustration shows all components that are addressable via I2C and can therefore also be monitored. Taken from [11].

6 The Monitoring of the Tile Rear Extension Module

In order to ensure safe operation of the ATLAS experiment and to detect technical defects immediately, it is of great importance to continuously monitor the individual subcomponents of the experiment. This also applies to the newly installed components of the Phase-1 upgrade. The monitoring is performed by the ATLAS *Detector Control System* (DCS).
This chapter first describes the general structure of the ATLAS DCS in Section 6.1, followed by the DCS back-end implementation of the TREX system as a new Phase-1 subcomponent in the existing ATLAS DCS in Section 6.2.

6.1 The ATLAS Detector Control System

The ATLAS DCS [60–64] controls and monitors the complete ATLAS experiment to ensure safe operation. Thereby, the operational parameters of the individual systems are continuously checked and archived. In addition, the ATLAS DCS provides automatic control procedures, efficient error detection and handling, as well as communication to other systems such as the LHC.

6.1.1 Overall System Organisation

The DCS is built in a tree-like structure as shown in Figure 6.1, which can initially be divided into two sub-groups, the *Front-End* (FE) and *Back-End* (BE) [60–64].
The FE consists of the hardware of the system to be monitored and forms the lowest layer of the DCS. Its task is to collect the operational parameters, to make them available to the BE, and execute actions received from the operator via the BE. In the case of the L1Calo system, the FE is made up of the crates that house the hardware and mainly the individual modules themselves, as described exemplarily for TREX in Section 5.4. The connection between the FE and the BE is in most cases established through the *CAN industrial field-bus* (CANbus) or Ethernet.
The BE takes over the interaction with the FE and offers monitoring tools for tasks of storage, archiving, data processing, and analysis. In addition, these tools enable the visualisation of hardware data, messages, and alarms. Communication with the FE also

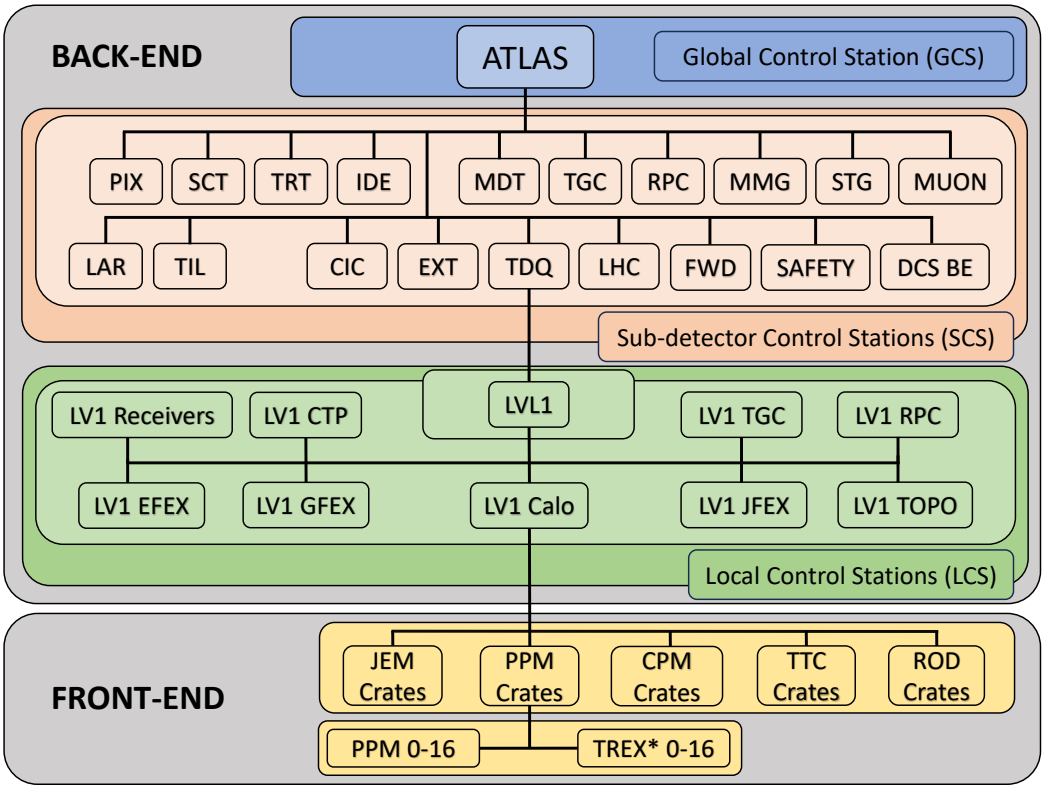

Figure 6.1: Overview of the ATLAS DCS using L1Calo as an example. The DCS system is initially divided into two parts, the Front-End (FE) and the Back-End (BE). The FE consists of the hardware to be monitored. The BE is implemented on a number of DCS servers and is built in a tree-like structure. It is divided into a global control station at the top, followed by several sub-detector control stations and, as the lowest level, the local control stations. Inspired by [63].

encompasses relaying operator actions within the DCS system [64].
The hardware of the ATLAS DCS BE is made up of a series of rack-mounted servers on which a *Supervisory Control And Data Acquisition* (SCADA) system using the industrial and commercially available *SIMATIC WinCC Open Architecture* (WinCC OA) as the base software has been implemented. This was extended by a framework developed in the course of a *Joint Controls Project* (JCOP) of the four large LHC experiments, the JCOP framework, in order to set common DCS standards and to guarantee joint development and maintenance of the detector control software.
The BE is divided into three main layers, as shown in Figure 6.1, which are described in the following [63]:

- Local Control Station (LCS): The LCSs form the lowest layer of the BE and are in turn subdivided according to geographical and functional characteristics, such as

the sub-group of eFEX modules. Each LCS is responsible for a sub-system of the sub-detector of the ATLAS experiment and forms the interface to the FE hardware, which is why the LCS receive the monitoring data of the hardware. In addition, they provide low-level monitoring and control of the sub-system's components and services. Tasks sent from higher levels of the BE are executed in the LCSs and passed on to the FE.

- Sub-Detector Control Station (SCS): The SCSs represent the middle layer of the BE and are organised into individual sub-detectors, such as the LAr or Tile calorimeter, according to the DAQ partition scheme. This subdivision into partitions allows full local operation of a sub-detector and a flexible standalone environment. This is used, for example, to operate the hardware in standalone mode, but also to monitor sub-system test rigs with the same DCS structure. The SCSs offer a concise representation of the subordinate LCSs hardware operational states.
  In addition, they form the interface to the TDAQ system, establishing communication through the *DAQ DCS Communication* (DDC) software and synchronising both systems. The SCSs provide the TDAQ system with state information of the individual sub-detectors, whereby the TDAQ system is able to trigger actions, which the SCSs then process and forward.

- Global Control Station (GCS): The highest layer of the DCS BE is the GCS. It is responsible for the entire detector operation and control, as well as the high-level monitoring. It also provides the operator interface and other service applications to control the DCS.

The entire BE is implemented as a *Finite State Machine* (FSM), which is the subject of Section 6.1.3, within a SCADA system developed with the software WinCC OA and extended by the JCOP framework, described in the following section.

6.1.2 Supervisory Control and Data Acquisition System

The basic software for the SCADA system that forms the software architecture of the ATLAS DCS is the commercial WinCC OA [65], which evolved from the PVSS II[5] software previously used by the four LHC experiments. It uses the script language *CONTROL*.

[5]German abbreviation for *Process Visualisation and Control System II*

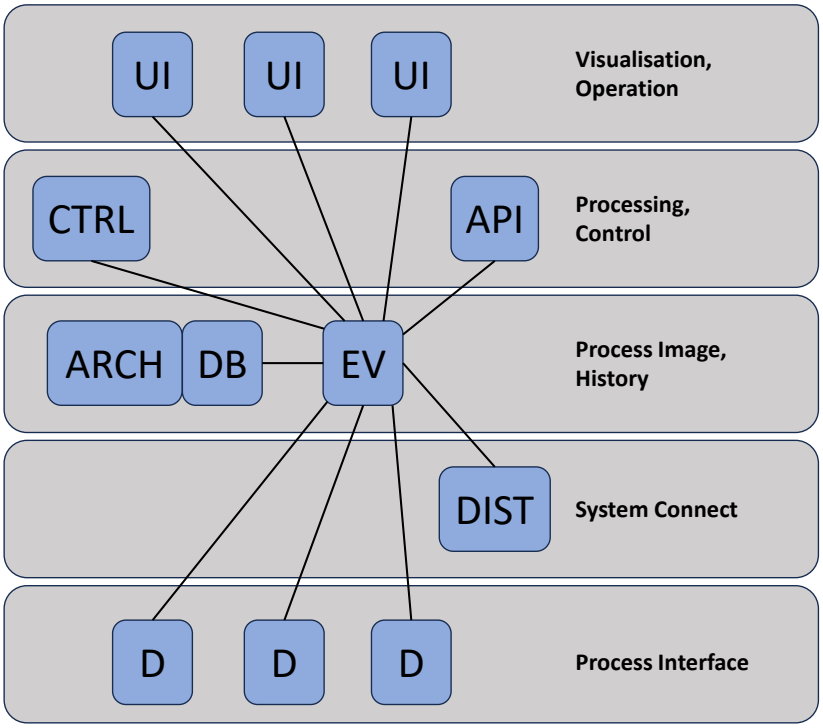

Figure 6.2: Overview of the structure of a WinCC OA project. The project has a modular structure and is divided into function-specific units, so-called managers. Inspired by [64, 65].

Architecture

An overview of the architecture of WinCC OA is given in Figure 6.2. It is highly modular and consists of so-called *managers* that take over various functionalities and are described in more detail in the following. The list below follows the information in [64, 65].

Process Image, History: The Process Image and History layer is the core of the WinCC OA project, with the *Event Manager* (EV) as the central processing unit. It is supported by the *Database Manager* (DB). Each WinCC OA project must necessarily contain these two managers. For additional archiving, an *Archive Manager* (ARCH) can be added to the project.

- Event Manager: As the central processing unit, the EV is the main data handler of the project. It organises the transfer of the complete data as well as operator actions and makes them available to the other managers. In addition, the EV is responsible for alert handling.
- Database Manager: The DB is in close contact with the EV and forms the

interface to the project internal database. Various values and parameters are stored in the database, including alarms, configuration parameters or changes to monitored values, all of which are handled during storage or retrieval via the DB.

- Archive Manager: For large amounts of data and for archiving them over a longer period of time, an additional ARCH, which forms the interface to an external database and is in close contact with the DB, is available in the WinCC OA environment.

Processing, Control: The Processing and Control layer provides the ability to execute processing and custom algorithms through a variety of options from different managers. The two most important and popular are the *Control Manager* (CTRL) and the *Application Programming Interface Manager* (API).

- Control Manager: The CTRL performs code execution in the CONTROL scripting language, which boasts an extensive function library designed for control and visualisation tasks.
- Application Programming Interface Manager: The API is a C++ class library that project developers can integrate to execute custom C++ code as a standalone manager.

System Connect: The System Connect layer contains managers with which different WinCC OA systems can be connected to each other. The *Distribution Manager* (DIST) plays the most important role.

- Distribution Manager: The DIST forms the interface to other WinCC OA projects and handles the communication between them. Among other things, it enables data from the other projects to be accessed, processed, and displayed.

Visualisation, Operation: The Visualisation and Operation layer forms the interface between the SCADA system and the user, using *User Interface Manager* (UI). This includes the *Graphics Editor* (GEDI) and the *Database Editor* (PARA).

- User Interface Manager: The UIs form the interface to the user and enable the display of data, alarms or even trends as well as the issuing of commands by the operator. The user interface is laid out in so-called panels, which can be freely designed by the user in various forms for different functions, such as the panel for the TREX modules described in Section 6.2.5.

- Graphics Editor: The pre-designed UI GEDI is used for the creation of new custom panels and provides all the necessary tools for this task.
- Database Editor: The PARA makes it possible to access the data points of the WinCC OA project in an intuitive way, to make changes to them or to create new ones.

Process Interface: The lowest layer of the WinCC OA project is the Process Interface layer, in which its managers are called *Driver* (D). These enable communication with the hardware to be monitored. Numerous drivers for various types of communication protocols, such as OPC UA, are available.

- OPC UA Client: The OPC UA client uses the OPC UA communication protocol to access the data of the hardware or forward actions to it by subscribing to an OPC UA server. The client can subscribe to multiple servers, thus allowing a single WinCC OA project to access the data of multiple hardware components.

The data that the WinCC OA projects receive from the hardware are divided into a special grouping within the project.

Data Structure

Within a WinCC OA project, the monitoring data received is divided into a three-level structure [64], explained in the following using a TREX example. The highest level reflects the *Data Point Type* (DPT), which corresponds to a device type such as an FPGA on the TREX (DPT $\widehat{=}$ FPGA). The second level is represented by the actual device, called a *Data Point* (DP) in the WinCC OA structure, and belongs to the corresponding DPT. In this example, it could be the first DINO FPGA on the TREX (DP $\widehat{=}$ DINO1). The lowest level is formed by the *Data Point Elements* (DPE), which describe the operational parameters of each device. This could be, for example, the temperature of the DINO1 FPGA (DPE $\widehat{=}$ Temperature).

Alarms

WinCC OA enables the monitoring of individual DPEs and the generation of alarms [63] in the event of issues. The configuration of these alarms offers significant flexibility, allowing to establish acceptable thresholds for each DPE and to trigger an alarm with the appropriate error status when these thresholds are crossed. The alarms raised can be visualized within a graphical user interface known as the *Alarm Screen*. In the ATLAS DCS

implementation, these alarms follow the same categories as the FSM status, as detailed in Section 6.1.3 and illustrated in Table 6.1(b).

Database Architecture

In order to permanently archive the various DPE values or to store configuration parameters required for WinCC OA, a number of different *ORACLE databases* are used in the ATLAS experiment [66]. An overview of the database architecture is given in Section 6.3. For the storage of the DPE values, a so-called *Relational Data Base* (RDB) Archive Manager is used in the WinCC OA environment to establish the interface to an external *ORACLE Online Database*. The data is permanently stored in the online database at certain intervals and can be accessed directly for monitoring purposes. However, for security and performance reasons, only systems within the *ATLAS Technical Network* can access the database.
Occasionally, there arises a need to access the database from beyond the technical network, primarily for debugging purposes. This necessity led to the development of an identical replica of the online database, known as the *ORACLE Offline Database*. This database is also accessed by the *DCS Data Viewer* (DDV) that provides an intuitive graphical application to display the DCS values through a web interface.
In addition to the offline database, the *COOL Conditions Database* (CondDB) is populated with some of the DCS values for access during offline calibration, reconstruction, and physics analysis with the ATLAS-wide offline software framework *Athena*, which is shortly described in Chapter 7.
Besides the databases for the DPE values, there is also the *Configuration Database* (ConfDB) that contains and stores configuration parameters for the corresponding WinCC OA project. Once more, the ConfDB is realised by a set of ORACLE databases, but in this case it is integrated directly into the WinCC OA project, using tools from the JCOP framework.

6.1.3 Finite State Machine

The complete ATLAS DCS system is represented in WinCC OA as a multitude of different and connected FSMs [63, 67] according to the combined FE and BE hierarchy. For this purpose, the JCOP FSM toolkit is used. The FSMs are thereby subdivided into so-called *FSM Units*, which represent the different systems within the BE hierarchy, such as abstract logical summaries, like the Level-1 trigger system, or components of the FE, e.g. the TREX

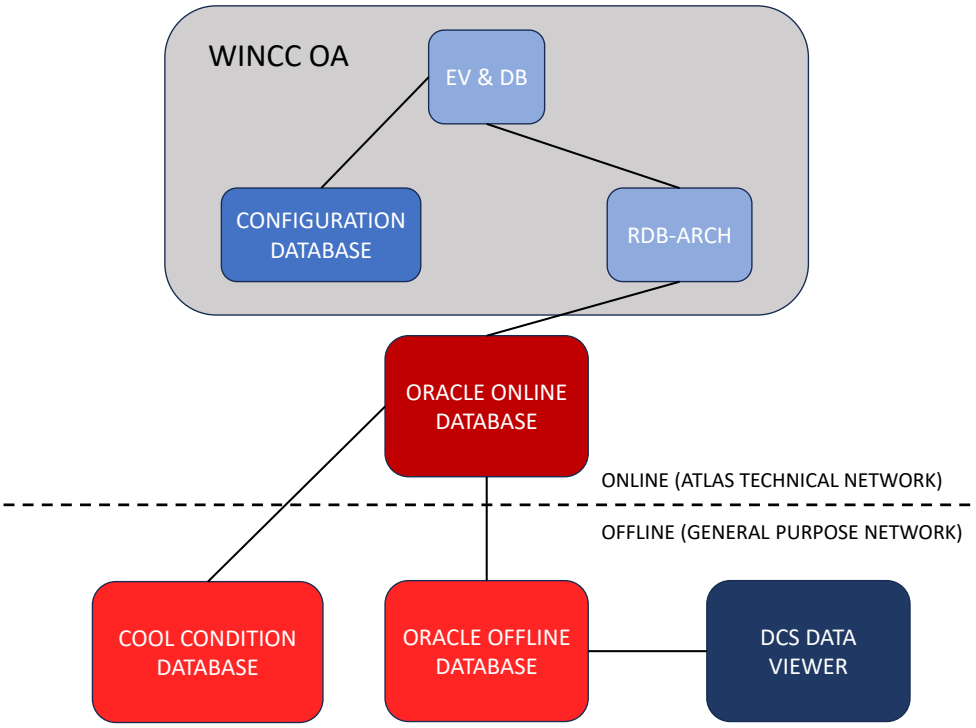

Figure 6.3: Overview of the ATLAS database structure. The various ATLAS databases are used to archive monitoring data and store configuration parameters for the WinCC OA project. The structure is divided into an online and offline component, where the online part can only be accessed within the ATLAS technical network. The Oracle offline database is an exact copy of the online database and thus allows access outside the protected network. Inspired by [63, 66].

module. These significant differences are also reflected in the three types of FSM units explained below [63, 67]:

- Device Unit (DU): The DUs form the lowest layer of the FSM and represent actual hardware by working with the monitoring data and determining a general health as well as physical condition of the device. In addition, they receive user commands through the FSM tree and convert them into a hardware-usable form. As the lowest layer, DUs cannot have their own children in the FSM hierarchy. Furthermore, the partitioning of FSMs and stand-alone operation at the level of DUs is not possible.
- Logical Unit (LU): The LUs form the layer directly above the DUs and are responsible for forming an abstract logical node that provides a condition summary and overview of the children below it. Accordingly, they are able to have children except of the Control Unit type. LUs perform similar tasks as the Control Units, but are not as processor-intensive and can therefore improve the overall performance of the

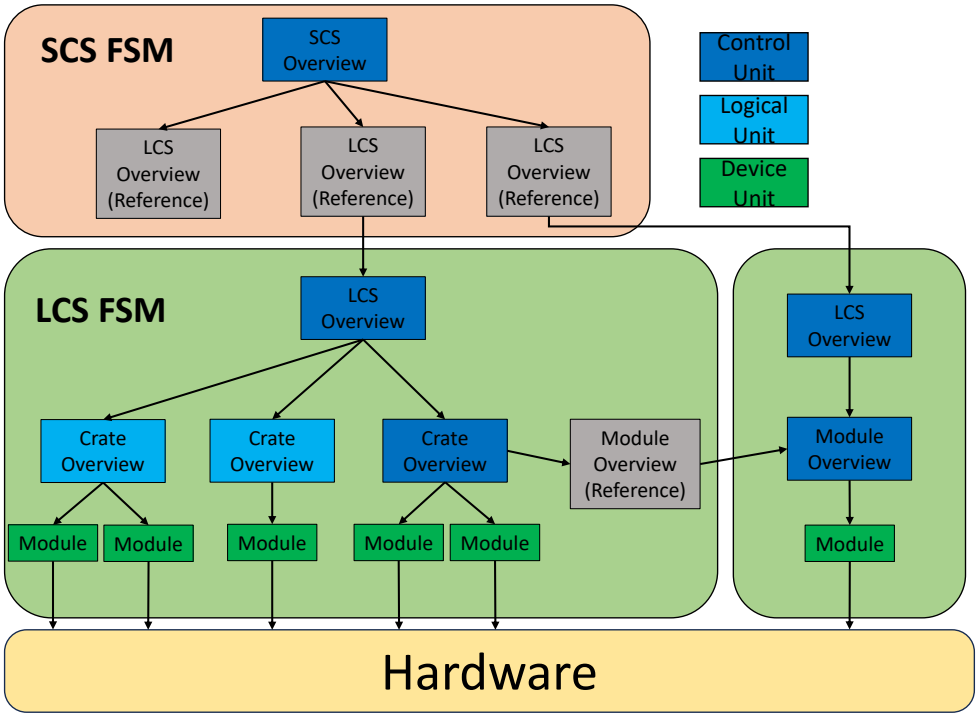

Figure 6.4: Overview of an ATLAS FSM structure. The FSMs run on the DCS servers and are divided into so-called units. The Device Units are the lowest layer and represent the actual hardware in the FSM environment. The Logical Units and Control Units form abstract logical summaries and reflect the state of the children. The Control Units implement the possibility of partitioning the FSM and thus enable the standalone operation of the Control Unit and the underlying children. Inspired by [63].

DCS system. Like the DUs, the LUs cannot be operated standalone.

- Control Unit (CU): Similar to the LUs, CUs also provide a summary and overview of the condition of their children, but this time all unit types are allowed (DU, LU, CU). The characteristic of CUs is the implementation of the partitioning of the FSM, which allows a standalone operation of the CU with its underlying children.

Figure 6.4 shows an example arrangement of different FSM units. The lowest layer is formed by the DUs with either LUs or CUs above them. Furthermore, the possibility of references is shown, whereby two different FSMs running on different PCs can be linked to each other.
The ATLAS DCS FSM distinguishes itself from the DCS systems of other LHC experiments by adopting a distinctive approach. Unlike the conventional single-condition FSM, the Central DCS team of the ATLAS experiment decided to implement two separate conditions known as *state* and *status*, which are typically unrelated.

The state serves as an indicator of the operational mode for the monitored system. The number and definition of the various states is largely left to the sub-systems and their needs, except for the CU of the last layer of the SCS, which is connected to the GCS and must contain the states READY, NOT_READY and SHUTDOWN. Nevertheless, there are suggestions and a colour scheme from the central ATLAS DCS team, shown in Table 6.1(a), to which the sub-systems should adhere.
The current operating condition of the system is conveyed by its status, which comprises four clearly defined statuses of increasing severity: OK, WARNING, ERROR, and FATAL, as shown in Table 6.1(b). The OK status implies that the system is working normally. A WARNING, on the other hand, has the lowest severity and indicates that the system is still functional. The ERROR status already shows a high severity and should be dealt with as soon as possible. By far the most crucial status is the FATAL, as this indicates that the system is no longer functional [63, 67].

Table 6.1: The shown overview of the state and status colour coding gives an impression of the visual representation of the condition of the FSM. Taken and modified from [67].

(a) State colour coding

Colour	State Description
	Final operational state
	Not final operational state
	Lowest operational state
	Standby state
	Transient state
	Error/Unknown state
	Severe error state

(b) Status colour coding

Colour & Status	Status Description
OK	System fine
WARNING	Low severity
ERROR	High severity
FATAL	Very high severity

6.2 TREX DCS Back-End Implementation

The TREX DCS BE is responsible for processing and monitoring the operational parameters received from the 32 installed TREX modules via OPC UA servers.
This section gives an overview of the implementation of the TREX BE, starting with a description of the OPC UA server design and the values to be monitored in Section 6.2.1. Afterwards, the basic WinCC OA setup, the FSM of the TREX BE, and the implementation within the current L1Calo FSM are explained. Finally, the panel design for visualising the state, status, and monitored values of the TREX modules is examined in more detail.

6.2.1 TREX OPC UA Server

The OPC UA server [11] running on the Zynq MPSoC processor of the TREX enables the transport of the data to be monitored from the FE to the BE by allowing a OPC UA client within a WinCC OA project to subscribe to it via Ethernet.
The OPC UA server is generated with the *Quick OPC UA Server Generation Framework* (quasar) [68, 69] by providing a design from the user based on the respective device. An overview of the TREX design is given in Figure 6.5, where the values shown correspond to DPEs in the WinCC OA architecture.
The DPEs reflect the temperatures of the TREX's individual components, as well as voltages and currents. These are supplemented by boolean parameters, such as the power status of the TREX or the configuration status of the FPGAs, and additional component identification as well as version numbers.

6.2.2 TREX WinCC OA Architecture

For the 32 TREX modules installed in USA15, a single WinCC OA project was created, which runs on one of the DCS BE PCs. It consists of several managers, which were already explained in Section 6.1.2.
Like every WinCC OA project, the TREX project also contains the mandatory Event and Database Manager. In addition, a Control Manager is added, which executes general project-relevant processes as well as the FSMs of the TREX modules written in CONTROL. For communication with the TREX hardware, an OPC UA client is part of the TREX project that subscribes to all 32 OPC UA servers running on the TREX modules and therefore gives the project access to all required data. The added RDB Archive Manager implements archiving for the TREX modules, while the Distribution Manager establishes the connection to the L1Calo Legacy DCS, in which the FSMs of the TREX modules are referenced. The TREX project also implements its own panel design for the individual modules, which is shown in Section 6.2.5.

6.2.3 TREX Alarms

The alarms for the DPEs are defined on the basis of ranges limited by thresholds and generally follow the scheme of the FSM status shown in Table 6.1(b), which is provided by the central ATLAS DCS team as guidelines for the alarm implementation. However, depending on the type of DPE to be monitored, the number of thresholds set and consequently the number of ranges varies.

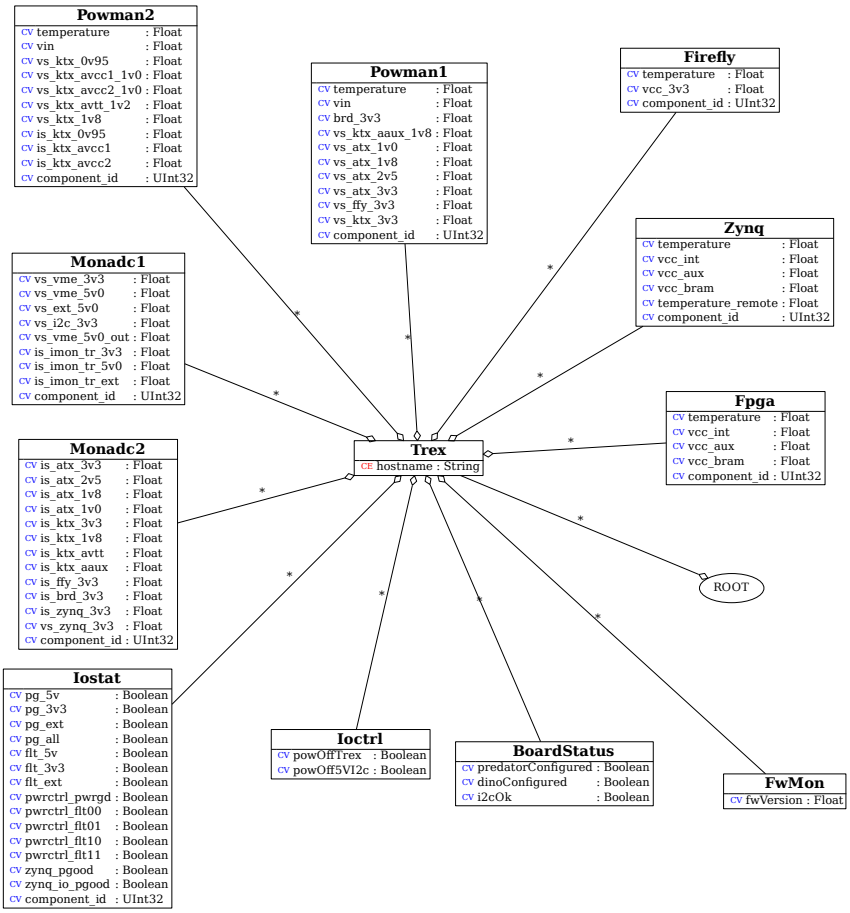

Figure 6.5: The illustration of the TREX OPC UA server design shows all Data Point Types and their corresponding Data Point Elements of the TREX module. Taken and modified from [11].

The temperature DPEs of the TREX components receive a total of six thresholds and thus define the following seven ranges from low to high temperature: Non Recoverable Low (FATAL), Critical Low (ERROR), Non Critical Low (WARNING), OK (GOOD), Non Critical High (WARNING), Critical High (ERROR), and Non Recoverable High (FATAL). The designation of the ranges as well as the severity is monitored and displayed in the ATLAS alarm screen.

In the case of the voltage DPEs, the lowest and highest fatal range is not implemented, as no fatal values can occur in the case of the voltages. This results in a reduction to four thresholds with five reachable ranges.

The current DPEs, on the other hand, usually only have one to three of the high alarm

thresholds, depending on the component, as low currents cannot be reached, resulting in two to four ranges.
The boolean DPEs are also assigned an alarm handling, whereby only one threshold is set. In the case of the TREX power DPEs, the two ranges OK (GOOD) and Not OK (FATAL) exist. The DPEs reflecting the configuration of the FPGAs can be in the state Configured (GOOD) or Unconfigured (WARNING).

6.2.4 TREX Finite State Machine

The FSM of a TREX module is located at the bottom of the ATLAS FSM hierarchy, as already indicated in Figure 6.1. The top node is the ATLAS GCS FSM, which is followed by the TDQ SCS FSM. The TDQ node references, according to the scheme in Figure 6.4, the first layer of the LCS, the LVL 1 FSM, that has gained further children through the Phase-1 upgrade, namely eFEX, gFEX, jFEX and Phase-1 L1Topo. However, for the TREX modules as physical extensions of the legacy PPMs, the legacy L1Calo LCS FSM as another child of the LVL1 node is the appropriate location for the TREX FSM, as shown in Figure 6.6.
The L1Calo FSM is represented at the top by an L1Calo Overview CU, which references the CUs of the 17 different crates of the L1Calo system. 15 of the crate overviews remain unaffected by the Phase-1 upgrade and have DUs of the types Crate, TCM and Module as children. The Crate DU gives an overview of the VME crate condition, the TCM type provides information on the state and status of the *Timing Control Module* [70], which is the interface of the VME modules to the DCS and TTC system, and finally the Module DU type covers the legacy L1Calo modules PPM, CPM, and JEM. More information on the legacy L1Calo DCS system can be found in [63].
The two remaining crates represent the two Tile VME crates and therefore have a reference to the TREX Module Overview CU in addition to the Crate, TCM and Module DUs. The TREX Module Overview CU forms the top layer of the two-layer TREX FSM implemented for each individual module, with the TREX Module DU as its child. This two-level arrangement in CU and DU is necessary to form a reference to the TREX FSM within the crate overview, which is only possible with a CU type.
The DU type of the TREX has been uniquely designed for the requirements of the module. An overview of the different states and the implemented actions can be found in Figure 6.7. The state of a TREX module depends on several individual DPEs. The module receives the state ON if the power DPE of the TREX has the value 1 and the TREX module has not lost the connection to either the OPC UA server or the I2C. If the connection is

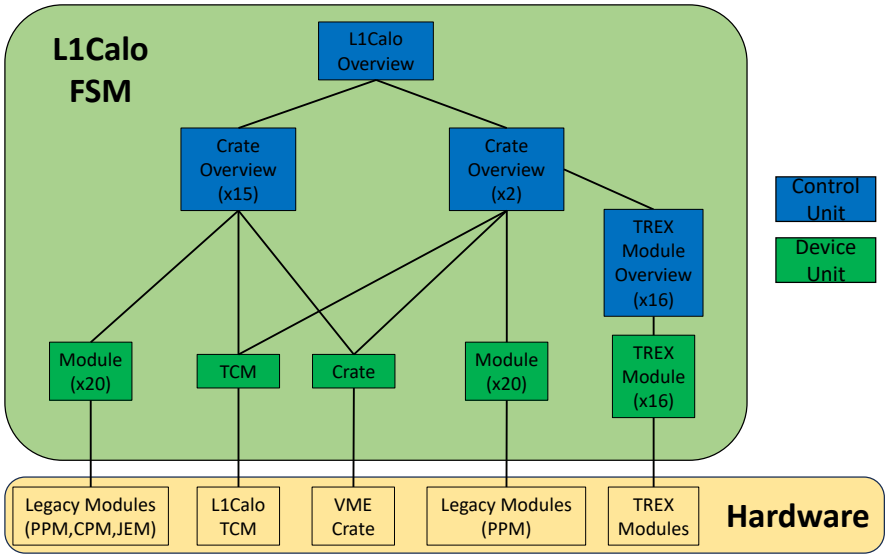

Figure 6.6: Illustration of the legacy L1Calo FSM implementation. The L1Calo FSM is initially arranged in a higher-level Control Unit (CU), which has a subordinate total of 17 Crate Overview CUs. Before the Phase-1 upgrade, these were all identical in terms of their FSM structure and contained Module, TCM and Crate Device Units (DUs). By introducing the TREX, the two Tile PPM crates were each supplemented with 16 TREX FSM structures consisting of a higher-level CU and a lower-level DU. Inspired by [63].

lost, the TREX FSM automatically receives the state UNKNOWN because no statements can be made about the condition of the module. The OFF state is reached when the Power DPE is set to 0. As user actions within the DU FSM, GOTO_ON and GOTO_OFF have been implemented, with which the TREX can be either switched on or off.
The conventional three states mentioned are extended by a fourth special UNCONFIGURED state that is set when one of the DINO or PREDATOR FPGA configuration DPEs are 0. Returning to a conventional state would require manual expert intervention.
The status of the TREX Module DU is directly related to the alarm definition of the DPEs described above and is propagated to the higher layer FSM units.
As TREX Module Overview CU, the standard ATLAS_CU_DEVICE_PASSIVE type developed by the central ATLAS DCS team was used, which however had to be adapted to the ATLAS_CU_DEVICE_PASSIVE_UNCONF type due to the special UNCONFIGURED state of the DUs. An overview of the determination of the CU state is given in Figure 6.8. The 32 TREX CUs pass their state to the legacy Crate Overview CU, which gives a summary of the crate condition in question and feeds its information into the generic L1Calo CU.

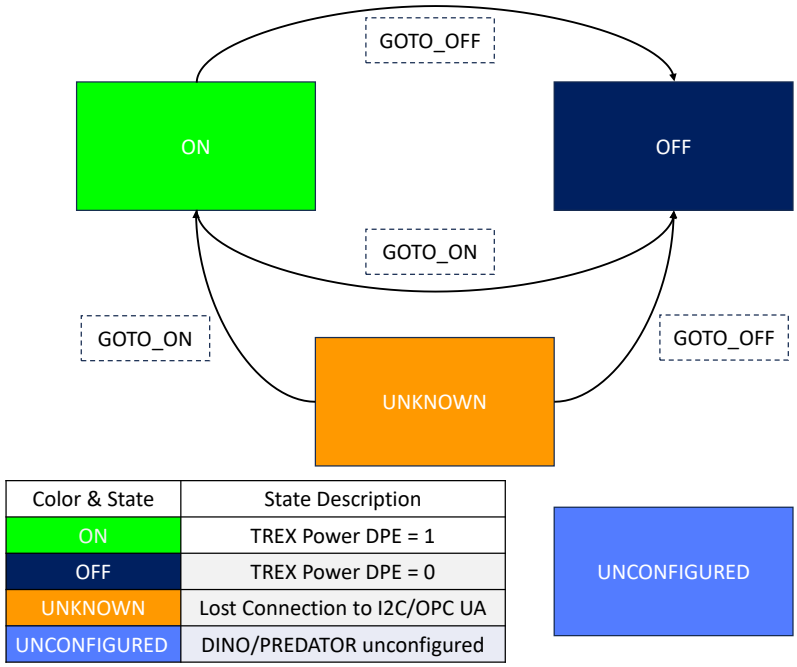

Color & State	State Description
ON	TREX Power DPE = 1
OFF	TREX Power DPE = 0
UNKNOWN	Lost Connection to I2C/OPC UA
UNCONFIGURED	DINO/PREDATOR unconfigured

Figure 6.7: The illustration of the state machine of the TREX Device Unit shows the four different states and the possible transitions between them. The UNCONFIGURED state can only be exited by a manual expert intervention. The table shows an overview of the accessible states of the TREX Device Unit. The state description is only to be regarded as a brief general summary of how the state is reached and does not cover any specific special cases. Inspired by [63].

6.2.5 TREX Panel Design

Each unit of the LCS has a graphical interface called a panel that displays information about the respective FSM component. The graphical interface also provides the user with an overview of the FSM, enables navigation through it, and allows the defined actions to be executed, such as GOTO_ON or GOTO_OFF. Figure 6.9 shows the panel of the TREX module DU.

It is designed according to the model of the legacy Module DU panel in the graphical editor GEDI and consists of several sub-panels. The basis is formed by a common L1Calo design that was created for all Phase-1 L1Calo modules and defines the structure with DPE table, module schematic, reading display, node and fault information. The sections are then filled with module-specific panel designs, such as the module schematic of the TREX board, which additionally shows the temperatures of the individual components. The DPE table displays most of the relevant DPE online values with their thresholds. If

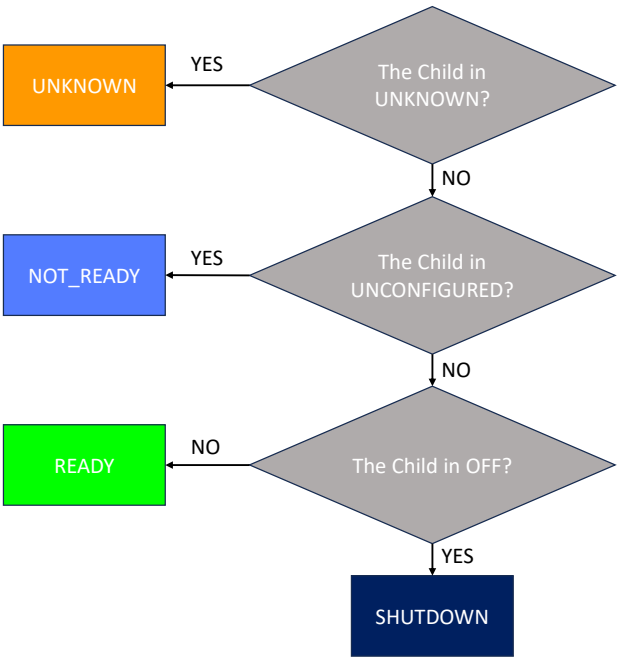

Figure 6.8: Illustration of the process for determining the TREX module Control Unit state. A Control Unit for the TREX was introduced for referencing reasons and was developed based on the ATLAS_CU_DEVICE_PASSIVE type specified by the central ATLAS DCS team. Inspired by [63].

a threshold is crossed, it will be shown in the fault information section. The reading display allows a quick search for a DPE within the table, while the node information section gives an overview of the critical DPEs determining the state and provides general module information.

The TREX Module Overview CUs show exactly the same panel design as the DUs, as these were only introduced for the purpose of referencing and do not provide any additional information.

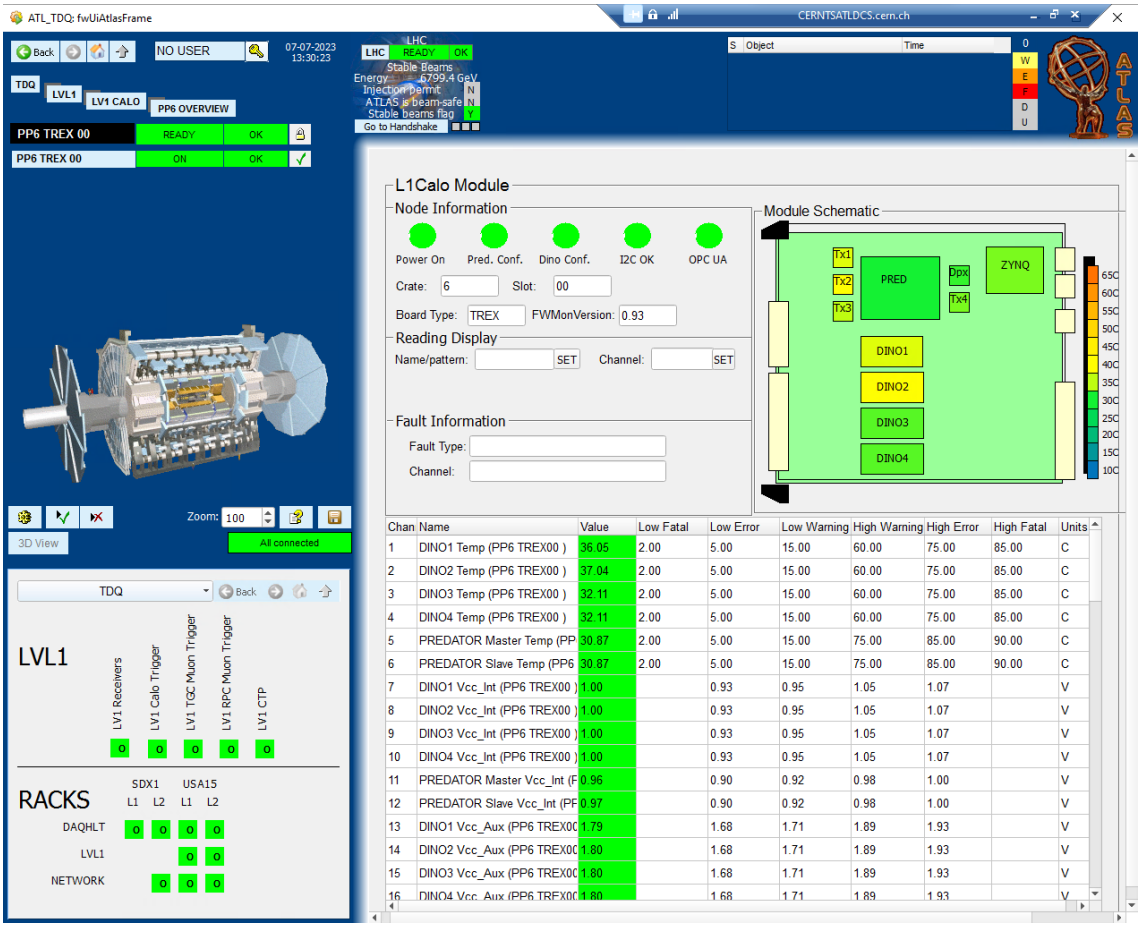

Figure 6.9: The TREX Device and Control Unit panel. The design is based on the legacy L1Calo concept and was developed as a general panel for the new Phase-1 modules with specific sub-panels depending on the module type.

7 The Level-1 Calorimeter Trigger Online- and Offline-Software

The software architecture of the L1Calo system can be divided into two main components, the online and offline L1Calo software. The online software is largely written as a stand-alone software framework, but is in close contact with other software packages, such as the ATLAS TDAQ software. The offline software, on the other hand, is partly implemented directly in the ATLAS-wide offline software framework Athena or uses its environment. In the following sections, an overview of the L1Calo online and offline software is given, with main focus on the tools used during the thesis. In addition, the implementation of the TREX simulation in the L1Calo online software is considered in Section 7.2 as well as a performance study conducted with the offline software in Section 7.4.

7.1 The L1Calo Online Software

The main task of the L1Calo online software [71] is to control, calibrate, test, and monitor the L1Calo system. In general, the online software can be divided into a total of eight main sections and interacts closely with other software packages. An overview of the structure is shown in Figure 7.1. The information in this section follows the information in [71]. In the following, the different areas are described in more detail according to their importance for this thesis:

- Infrastructure and Database: The infrastructure and database layer contains on the one hand a number of infrastructure tools that interface with various other software packages, such as CERN software, External software, ATLAS TDAQ software, and ATLAS offline software. On the other hand, the L1Calo database packages [72, 73] allow communication with various ATLAS wide databases, an overview of which is given in Section 6.1.2, or with TDAQ as well as L1Calo databases. The TDAQ database contains the hardware configuration of the L1Calo system with crates, modules, and connections between them. The L1Calo COOL database in particular contains the configuration and calibration values of all L1Calo modules.

- Hardware Access and Diagnostics: The software of the hardware access and diagnostics layer enables communication with the L1Calo modules for the legacy system via the *VMEbus* [74] and for the Phase-I system via the *IPbus* [75] of the

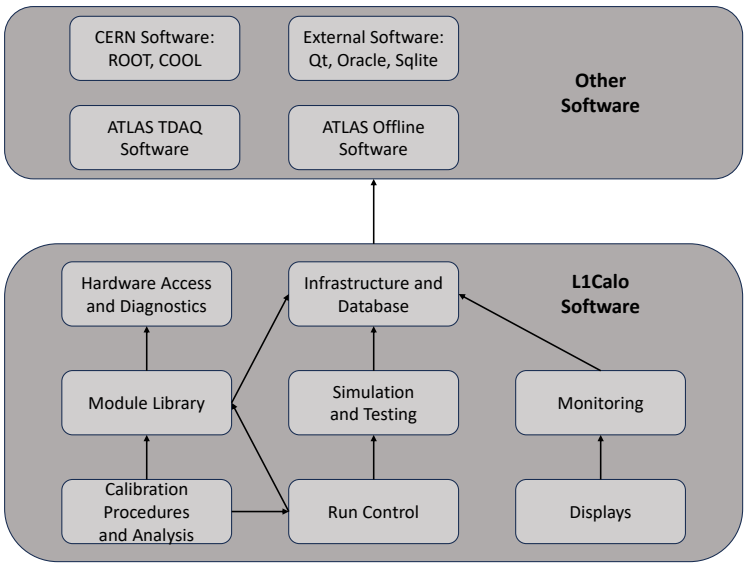

Figure 7.1: Overview of the L1Calo online software architecture. The L1Calo online software can be divided into eight main sections that perform the tasks of controlling, calibrating, testing, and monitoring of the L1Calo system. Inspired by [71].

crates. Each module has its own set of registers and memories that determine the configuration of the module.
The hardware access software allows the configuration of the hardware during different types of operation, whether at the start of a run by the *ATLAS TDAQ run control* software [76] or when debugging individual modules in stand-alone mode. In addition, the L1Calo online software provides graphical diagnostic tools, the *Hardware Diagnostic Monitoring and Control* (HDMC) [74] system and *Serendip* for either the VMEbus controlled or IPbus controlled hardware, respectively, to debug down to the individual module register level.

- Run Control and Module Library: The aforementioned ATLAS TDAQ run control software enables the common control of the distributed ATLAS system. In addition, partitions for individual sub-systems, such as L1Calo, controlled by the run control software are also used for calibrations and system-specific tests. Via the IGUI of the run control software, synchronous run control commands resulting in a state change, e.g. initialised or configured, are forwarded to all sub-systems included in the partition. In order for the L1Calo system to function within the ATLAS TDAQ run control software, the L1Calo run control software as wells as the module libraries, which implement higher level functions, were developed.

- Simulation and Testing: A detailed online simulation [77] for the individual components of the L1Calo system is implemented in the L1Calo online software. The online simulation was extended in the course of the Phase-1 upgrade to include the new hardware, among them the TREX module and its simulation, which is described in the following Section 7.2.
  The online simulation was used during the hardware and firmware development phase to check the individual components and compare the data obtained at any point in the system. For this purpose, the components of the real-time path of the L1Calo system have playback and spy memories to feed generated test data following various different patterns into the system. The same test patterns are used within the simulation to finally make a comparison between the read out data of the hardware and the events built by the simulation, in order to detect possible errors at an early stage.

- Monitoring: Within the ATLAS TDAQ online monitoring framework, L1Calo has developed a variety of monitoring software [78] to collect events at any point in the readout, decode them using so-called *byte-stream decoders* and subsequently populate monitoring histograms that allow to determine the data quality of the events.
  The online byte-stream decoders were additionally used for first data analyses of the Phase-1 system, as they were already available in an early stage of the development of the Phase-1 hardware.

- Calibration Procedures and Analysis: There are many parameters in the L1Calo system that need to be determined through calibrations at regular intervals. These include the DAC and PED calibration scans of the PPM or the timing and energy calibrations performed in combined partitions of L1Calo and the calorimeters. More details about the calibrations are given in Section 8.1.
  For the execution of the calibrations, a number of software packages [79] have been introduced in the L1Calo online software. The results of the calibrations are processed with online or offline analysis software to determine appropriate calibration parameters.

- Displays: A variety of graphical interfaces for the L1Calo system have been developed as part of the L1Calo online software. Among others, besides the already mentioned HDMC and Serendip, a L1Calo panel for the ATLAS TDAQ run control software was developed, which shows a detailed status of the individual modules.

In addition, a table with various L1Calo trigger rates and the *L1Calo mapping tool* were introduced. The L1Calo mapping tool allows a visualisation in the η-ϕ space of L1Calo TTs, showing their interconnections, database parameters, trigger rates, and simple event data. Another useful tool is the *L1Calo event viewer*, which allows the user to examine decoded L1Calo event data in a convenient way.

During the commissioning of the ATLAS system for Run 3, new ATLAS TDAQ software versions required constant updates of the L1Calo online software. In addition, for the Phase-1 upgrade, all previously described areas of the L1Calo online software were extended for the new hardware. This includes the topic of the next section, the TREX online simulation.

7.2 TREX Online Simulation

The TREX online simulation was introduced as part of the existing legacy L1Calo online simulation to verify the functionality of the TREX hardware, described in Chapter 5, and to establish the connections for forwarding the Tile calorimeter information to the new FEX systems within the simulation. In a first step, the online software configuration of the L1Calo system was extended with TREX modules and connections to the FEX systems, the FELIX as well as the SW ROD according to the test setup.
The existing simulation of the readout data path to the legacy ROD inside the *rodSim* software package was extended with a simulation of the readout to the FELIX and SW ROD system in order to compare the results with the actual new TREX hardware readout. Since the functionality of the legacy ROD readout had not been changed and was only transferred from the PPM to the TREX, the simulation design was not modified.
Due to the development of the simulation software at an early stage of the TREX hardware, the format shown in Figure 5.3, which uses the same G-Link format for the event data as the legacy readout, was implemented for the new Phase-1 readout in the simulation. This also simplified the development of the TREX readout simulation, as the data already packed for the legacy readout simulation in the G-Link format was used as direct input into the new Phase-1 TREX readout format and only TREX headers as well as trailers had to be added.
For the comparison of the real-time paths from the TREX to the FEX systems between hardware and simulation, the latter was included in the software package *ppmSim* as part of the already existing PPM simulation. In the implementation process of the real-time path simulation of the TREX, it was first necessary to demultiplex the simulated output

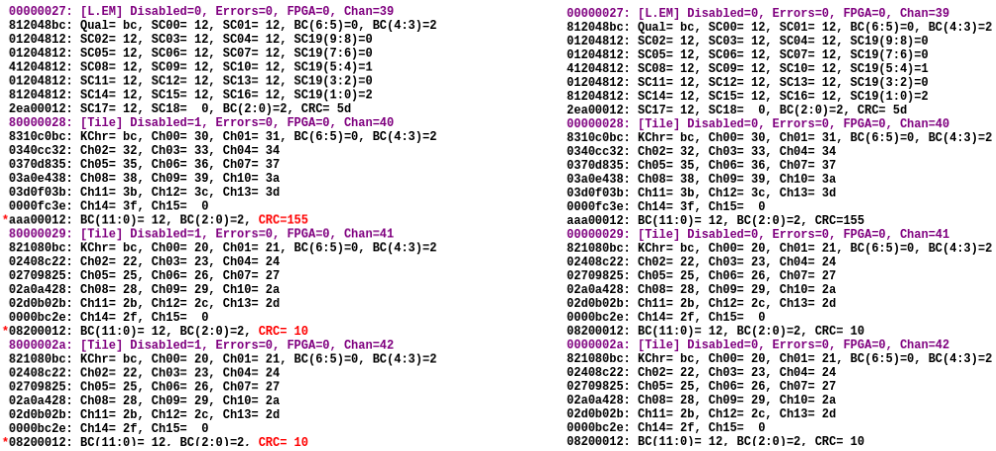

(a) eFEX Hardware Input Data

(b) eFEX Simulation Input Data

Figure 7.2: Comparison between eFEX hardware and simulation input data with the L1Calo event viewer. Figure (a) shows the hardware data, which has CRC errors and faults in the display of the disabled channels, which could be traced back to firmware problems. Figure (b) illustrates the simulation data. The comparison shows a perfect match of the data with the exceptions already mentioned.

of the PPM intended for the CP system, which was still multiplexed with the BCMUX procedure explained in Section 3.1.1.2. For this purpose, the already implemented demultiplex logic of the CP simulation in the *cpmSim* software package was used.
The demultiplexed data intended for the CP system, originating from the nMCMs arranged in increasing numbers, had to be reorganised according to increasing PPM digital channel numbers for the needs of eFEX and jFEX. With the reorganised data, the data packages sent via one fibre were then packed together for eFEX and jFEX according to the data formats shown in Figures 5.2(a) and 5.2(b), respectively. The data intended for the JEP system were directly packed into the data format for gFEX, shown in Figure 5.2(c), without any further intermediate steps. The data formats were stored in so-called *FibrePacker* and were used within the ppmSim package. The legacy part of the ppmSim as well as the cpmSim and *jemSim* simulation packages were not changed in order to keep the legacy simulation functional.
After the implementation of the online simulation, tests were carried out in the STF to check the functionality. Figure 7.2 shows some of the test results displayed in the L1Calo event viewer in this case with the eFEX system. Figure 7.2(a) illustrates the read out input data from the eFEX hardware, including one channel from the LAr calorimeter and three channels with Tile calorimeter signals. The Tile signals on the one hand were generated on the PPM according to special patterns and forwarded to the eFEX via TREX, the LAr signals on the other hand originate from the LATOMEs.

The hardware results were then compared with the simulation results shown in Figure 7.2(b), which used the same signal pattern, but this time generated within the simulation. In comparison, a one-to-one match of the results is visible, except for the displayed CRC errors and the indication of the disabled channel for the TREX within the read out eFEX hardware data. Both problems were traced back to incorrect mappings, once for the CRC error and once for the disabled channels within the eFEX firmware. This example shows the usefulness of the simulation to finally locate issues. Furthermore, the data formats were verified in the simulation tests. Similar checks were also carried out for the jFEX and gFEX system, which finally led to a consistent result after several development and debugging iterations.

7.3 The L1Calo Offline Software

The L1Calo offline software is either directly implemented in the ATLAS offline framework Athena [80] or utilises its environment. Athena is used for the HLT, high-level event reconstruction, calibration, simulation, monitoring, and other core data analysis tasks. In summary, Athena is used for any processing of the events delivered by the ATLAS TDAQ system and makes the processed results available to the operator. Furthermore, the framework provides the user with a variety of physics analysis tools or a suitable development environment to ultimately generate physics results.
The user has the possibility with the Athena software to work with different data types that are defined in the *ATLAS Computing Model* [80, 81] and reflect the general data flow of the system, which is shown in Figure 7.3. The intermediate steps are also implemented as jobs in Athena and are explained in more detail below together with the data types:

- RAW Data (RAWD): The RAWD corresponds to the output of the last stage of the HLT and is arranged as a so-called *byte-stream*, which has no object-orientation. It represents the pure output of the detector information without any reduction, whereby a data size of about $1.6\,\mathrm{MB}$ per event is expected.

- Reconstruction: With the help of the offline reconstruction, various particle parameters and auxiliary information are determined from the collected RAW data of all subsystems in order to identify and reconstruct, for example, particle candidates such as electrons, which are necessary for physics analysis. The reconstruction step also includes decoding the RAW data using the offline byte-stream decoders.

- Derived RAW Data (DRAWD) & Preselection: The DRAWD samples allow the anal-

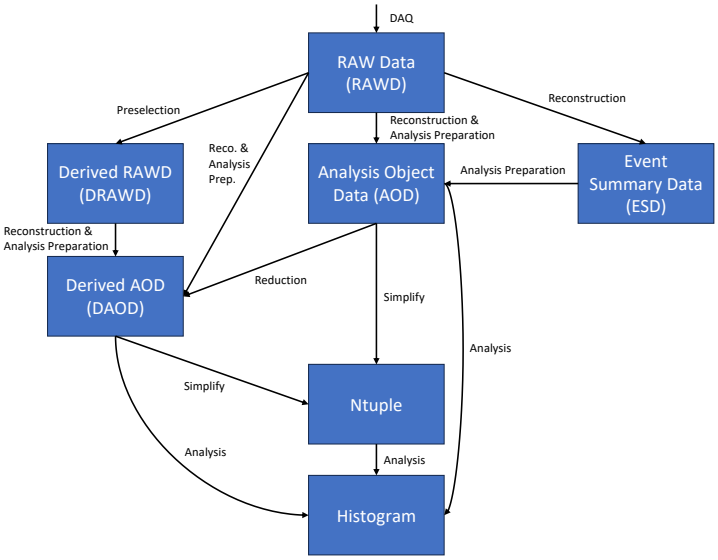

Figure 7.3: Overview of the offline software data flow. The offline software offers the user a variety of options and variability when accessing the RAW data of the ATLAS detector. Inspired by [80, 81].

ysis of special RAW events, such as $Z \rightarrow e^+e^-$ or $Z \rightarrow \mu^+\mu^-$ decays. These are selected via preselection on the basis of already determined reconstruction quantities. The $Z \rightarrow e^+e^-$ preselection was used in the studies presented in Section 9.3.2 and will be discussed in more detail there.

- Event Summary Data (ESD): The ESD corresponds to the output of the reconstruction, which is now object-oriented. The content is still very detailed in order to access e.g. individual cell energies of the calorimeters. The data size per event for ESDs is about $0.5\,\mathrm{MB}$ and these are stored into ROOT files. With regard to L1Calo, the general ESDs contained all read-out information, such as PPM information or any kind of TOBs, until early 2023. However, with the planed move to the Phase-1 system, the inclusion of PPM information was no longer supported.

- Analysis Object Data (AOD) & Analysis Preparation: The AODs represent a compact summary of the reconstructed events, but still contain sufficient information for common physics analyses. The expected size of the AOD per event is about $0.1\,\mathrm{MB}$, that is stored into a ROOT file, and is produced in two different ways. They can be derived from the ESDs through an analysis preparation in which various information is neglected, or through a combination of reconstruction and analysis preparation directly from the RAWD. With regard to the calorimeters and L1Calo, for example, the commonly produced AODs do not contain any PPM or calorimeter

cell information, but are populated with the TOB information.

- Derived Analysis Object Data (DAOD) & Reduction: The DAODs give the user a high degree of flexibility for the type of analysis planned by freely choosing the AOD information contained. With the derivation framework implemented in Athena, individual physics groups determine which data is written to the DAODs, that have a smaller data size and are used for specific analyses. They are derived in different ways and are in general produced centrally. On the one hand, through a direct reconstruction and analysis preparation of either RAWD or DRAWD and, on the other hand, through a reduction of the required data of an already existing AOD.
  The reduction step takes place in three different ways. The first is the so-called *Skimming* where whole events are filtered out based on preselection criteria. The second, called *Thinning*, defines the removal of whole objects, such as the electron physics object. The third and last way corresponds to *Slimming*, which describes the reduction by removing variables, such as the transverse energy of the electron object, uniformly for all events and objects.
  In the case of L1Calo, two different types of DAODs are implemented in the derivation framework, which are additionally applied to different DRAWD data. In general, both contain all the data read out by the L1Calo system in addition to various offline physics objects to enable analysis based on L1Calo information. The first type of DAODs, the *L1Calo1* DAODs, introduce thinning on the PPM TT information. The information is only retained if either one of the TT ADC values is above 36 or the calorimeter cell transverse energy E_{T} is above $0.8\,\mathrm{GeV}$. This already greatly reduces the data sizes of the DAODs. In addition, randomly selected $1\,\%$ of all TT data is kept in the L1Calo1 DAODs. In general, the L1Calo1 DAODs can be used in all analyses that consider signals, as only noise should be filtered out by thinning. Examples are efficiency or calibration studies.
  The *L1Calo2* DAODs do not introduce any reduction and ensure that an AOD exists with all information for any kind of L1Calo analysis. This enables, among other things, the investigation of noise or filter coefficients.

- Ntuple & Simplify: Ntuple are a simpler version of AODs. They consist of simple data types and vectors that are filled with information from AODs in the simplification process. Moreover, they do not require the Athena framework and can be analysed with the ROOT software provided by CERN.

- Analysis: The last step of the data flow is the analysis. The code can be implemented in the Athena framework or uses its environment to run the analysis directly on AODs or DAODs. The other variant allows the analysis of the ntuple without the Athena framework.

The L1Calo offline software has been enhanced during the Phase-1 upgrade with various tools, some of which have already been mentioned, to allow commissioning and general data taking with the Phase-1 system:

- Byte-stream decoder: One of the most crucial parts that were implemented were the offline byte-stream decoders, which finally enabled the analysis of the read out Phase-1 data on a large scale. They had to be newly developed, debugged, and tested for the Phase-1 systems but were partly derived from the online byte-stream decoders.

- L1Calo DAODs: The L1Calo DAODs were initially extended with various Phase-1 information in manual production. For this purpose, a dedicated production software package was implemented in the L1Calo offline software, working within the Athena environment. After a longer period of testing, debugging, and validation, the Phase-1 information was added to the centrally automated production of the L1Calo DAODs.

- Ntuple Production: The L1Calo offline software was extended with a ntuple production software package, which also uses the Athena environment. The ntuple code was first developed for legacy L1Calo data and was extended step by step with further L1Calo Phase-1 information, such as eFEX TOBs. There is also the possibility to add SC information from LAr to the ntuples for low-level comparisons between both systems, or also CTP readout for trigger studies. The ntuples will then be analysed with custom-made ROOT scripts outside Athena, simplifying the analysis procedure.

- AOD Analysis: Another part of the L1Calo offline software is the AOD analysis software package, which combines a variety of algorithms for the analysis of AODs as well as DAODs. It uses again the Athena environment and allows, among other things, all kinds of comparisons between the Legacy and Phase-1 system as well as the determination of trigger efficiencies, which were used for the studies described in Chapter 9 and 10.

- Simulation: One of the biggest development tasks in terms of L1Calo offline software was the implementation of the high level bit-wise simulation for the Phase-1 systems. The simulation of the L1Calo system is part of the Athena framework and enables a more detailed check of the L1Calo system, especially of the various running algorithms. The goal is to automatically recalculate the trigger decision by the algorithms for each ATLAS event on a bit-wise level and compare it with the readout of the L1Calo hardware. The simulation of the FEX systems also allows the emulation of TOBs with either calorimeter or FEX input to the simulation, which was used for the studies described in Chapter 10. In addition, the simulation has been utilised to perform studies prior to the completion of the Phase-1 system, one of which is described in the next Section 7.4.

- Monitoring: As part of Athena, the L1Calo monitoring framework is implemented for monitoring the data quality of the L1Calo system. For this purpose, various types of histograms were also introduced for the Phase-1 system, such as efficiencies, comparisons with simulation or even simple hit maps. The legacy part of the monitoring also underwent some changes to adapt to the regularly introduced newer versions of the Athena framework.

Finally, the L1Calo offline software integrated in Athena also includes the analysis of the legacy energy calibration, called *RampMaker*, which is used in the calibrations in Section 8.1.3. The software could still be used in large parts, but had to be adapted to the new requirements of the updated Athena version for Run 3.

7.4 FEX Offline Simulation Studies

In order to determine the expected performance of the algorithms of the FEX systems, described in Section 4.2.1, and thus to obtain statements about the efficiency as well as the reduction of L1 trigger rates, the implemented offline simulation of the L1Calo system as part of the Athena framework was used.
As an example, the first study [82], shown in Figure 7.4, compares the single electron trigger efficiencies of the CP's legacy EM trigger with the proposed simulated Run 3 EM trigger implemented in eFEX. The data used are based on Monte Carlo simulation of the $Z \rightarrow e^+e^-$ process. For the calculation of the efficiencies, the *tag-and-probe* method, described in Section 9.3.1, was used, whereby only electron candidates satisfying, among other things, a likelihood-based medium identification and an isolation were considered as tag electrons. For the rate reduction of the eFEX trigger, its isolation parameters were

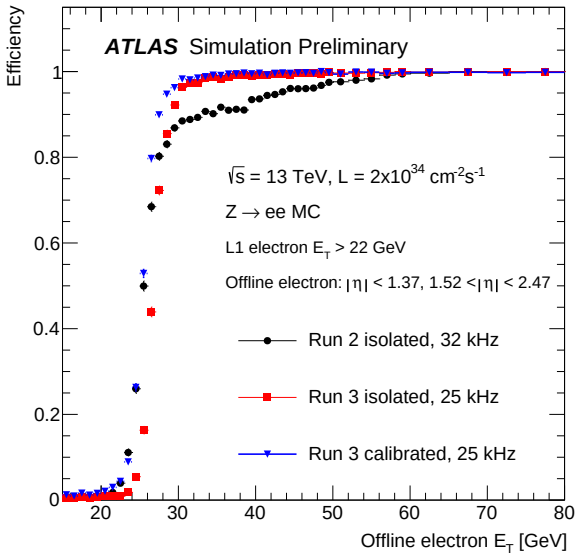

Figure 7.4: Single electron trigger efficiency comparison between the legacy CP EM trigger and the eFEX EM trigger. The tag-and-probe was used to determine the efficiencies. The black curve shows the efficiency of the legacy system at an L1 rate of $32\,\mathrm{kHz}$, which has a worse performance and a higher rate compared to the red efficiency curve of the eFEX system. In the blue efficiency curve, dead material corrections were introduced and the TOB E_T threshold was adjusted. Taken from [82].

tuned. The isolation criteria are only applied to TOBs up to an energy threshold $E_{\mathrm{T,max}}$ of $50\,\mathrm{GeV}$ for the legacy system and $60\,\mathrm{GeV}$ for the new Run 3 system. A TOB E_T threshold of $22\,\mathrm{GeV}$ was used for the Run 2 trigger (black in Figure 7.4) and the uncalibrated Run 3 trigger (red in Figure 7.4). The blue curve in Figure 7.4 represents the Run 3 trigger, which however introduces a layer- and η-dependent *Dead Material Correction* (DMC), to correct for varying detector responses. The TOB E_T threshold for this trigger has been set to achieve the same rate as the uncalibrated Run 3 trigger. Furthermore, the overlap area between barrel and endcap in the range of $1.37 < |\eta| < 1.52$ is in the studies not considered. As shown in the figure, the new Run 3 trigger is expected to have an improved single electron trigger efficiency at a lower trigger rate than the Run 2 trigger. Similar studies and comparisons have been made in the course of this work using Run 3 data, which is the content of Section 9.3.

Further simulation studies have been carried out, for example, for the eFEX and jFEX τ algorithms as well as for various missing transverse energy $E_\mathrm{T}^\mathrm{miss}$ algorithms from jFEX and gFEX, which can be examined in more detail in [82].

8 Recalibration and Recommissioning of the Legacy Level-1 Calorimeter Trigger

The legacy L1Calo system was recalibrated and recommissioned for the start of Run 3. In this chapter, the various steps are explained with a focus on the part of the L1Calo system, which processes the Tile signals and which will be referred to as the *Tile L1Calo system*. Similar steps were also carried out for the LAr calorimeter. These will not be discussed in much detail in the following.
The recalibration and recommissioning of the legacy Tile L1Calo system became necessary due to the elapsed time, possible associated hardware problems, various repairs and adjustments to the Tile calorimeter, as well as the partly substantial changes resulting from the Phase-1 upgrade. The biggest impacts were the installation of the TREX module and the resulting adjustments to the legacy system, described in Section 5.1, the upgrade of the TTC system with the ALTI, explained in Section 4.2.3, and the various updates to the ATLAS software architecture as well as the L1Calo software, mentioned in Chapter 7.
The chapter will start with a general overview of the standalone and combined calibrations of the L1Calo system in Section 8.1. This is followed by a detailed description of the recommissioning steps leading up to a functioning and calibrated legacy L1Calo system, which took over the initial data taking period of Run 3 and contributed greatly to the commissioning of the Phase-1 system.

8.1 Calibrations of the Legacy L1Calo System

In order to set up the legacy L1Calo trigger optimally for successful data taking, a number of different calibration parameters are available. These are determined by calibrations performed in regular intervals, even during normal data taking. Only in certain cases, such as after technical shutdowns, major changes or technical problems, the parameters are validated, which means that they are released after thorough tests for usage during physics data taking. However, the calibrations are still useful in most cases and serve as an additional check of the legacy L1Calo system's functionality. The regularly performed calibrations can generally be divided into two different groups.
The first group describes standalone calibrations, such as the *DAC* and *Pedestal* scans of the PPM. The second group consists of the combined Calorimeter-L1Calo calibrations, such as *Phos4* and *Energy* scans, which are performed in combined partitions and use

signals from the *Charge Injection System* (CIS) of the calorimeters, which inject an electrical signal with a known charge into the calorimeter electronics. The different calibration types are described in more detail below.

8.1.1 PPM DAC & Pedestal Scan

The DAC and Pedestal scan [83, 84] are only relevant for the PPMs of the L1Calo system and are therefore usually performed one after the other in standalone mode within calibration procedures defined in the online software.
As the name of the DAC scan implies, the focus of the calibration is on the DAC located on the AnIn board of the PPM, described in Section 3.1.1.2. During the calibration, several events at different DAC offsets of each PPM channel are recorded and compared with the digitised ADC values of the nMCMs in order to prove the expected linear dependence of the two quantities. In addition, as the primary objective during the calibration procedure, a DAC offset is determined for each PPM channel to set a uniform baseline of 32 ADC counts, the pedestal, throughout the entire system. The Pedestal scan is normally performed immediately after the DAC scan and takes events to determine the mean μ and the standard deviation σ of the pedestal.
Unusual shapes of the histograms resulting from the Pedestal scan, such as excessive width of the pedestal or even multiple peaks, as well as problems with the DAC scan would indicate a problematic PPM channel. For this reason, the DAC and Pedestal scan are also used for general checks of the functionality of the PPMs. More details about the scans can be found in [83].

8.1.2 Combined Timing Calibration

The combined timing calibration, also called Phos4 scan for historical reasons[6], has the overall goal of setting the timing for the calibrations with the CIS and thus setting optimal conditions for the energy calibration, explained in the next Section 8.1.3. The aim of the timing calibration is also pursued for the normal physics data taking, but must be determined for this case on the basis of data, which is described in more detail in Section 8.2.7.1.
The general goal of the timing calibration, both in physics and for CIS, is illustrated in Figure 8.1. Figure 8.1(a) shows a mistimed signal, since the sampling point is not at the peak position of the pulse and thus a correct bunch crossing identification as well as a

[6]Because of the Phos4 chip on the Run 1 MCMs

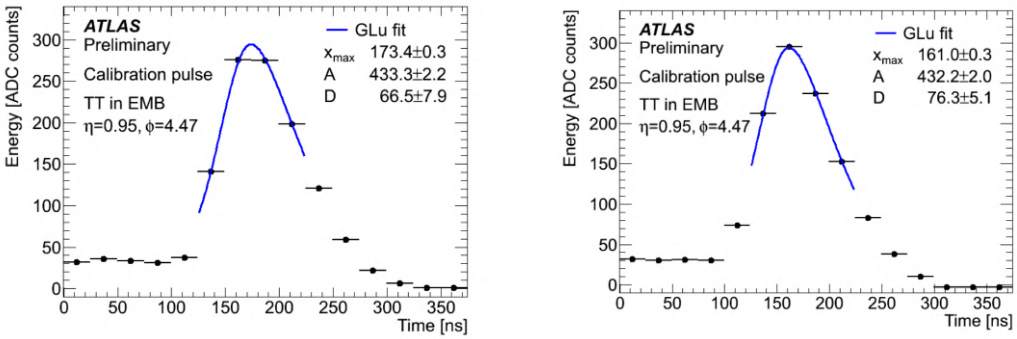

(a) Mistimed Calibration Pulse

(b) Well timed Calibration Pulse

Figure 8.1: Two calibration pulses from the same TT in the LAr EMB, fitted with a *Gaus-Landau* (GLu) function. Figure (a) shows a pulse with a mistimed setting when digitising the analogue TT pulse. Figure (b), on the other hand, shows a pulse whose sampling point lies on the peak position of the analogue pulse and is thus well timed, which reflects the intended timing setting of the L1Calo system. The Gaus-Landau function was chosen as the fit function because of the good description of a calibration pulse. Taken from [85].

precise determination of the deposited energy cannot be guaranteed by the PPM. Figure 8.1(b) shows the perfect setting that enables optimal further processing of the signals.
To shift the sampling point, the ADC clock phase can be delayed in relation to the LHC clock in steps of $1.042\,\mathrm{ns}$, as already described in Section 3.1.1.2. This results in 24 possible steps for a BC with a duration of $25\,\mathrm{ns}$.
The possibility of the stepwise delay is exploited in the Phos4 scan to scan through the constant signal of the CIS in 24 steps and thus obtain one sample point every $1.042\,\mathrm{ns}$, which allows a more precise determination of the peak position. With the generally extended readout configuration of "15+1" used for the Phos4 scan and the resulting 15 readout ADC values, 360 possible steps are therefore obtained for one pulse, which is shown in Figure 8.2. The figure also illustrates the excellent resolution of $1.042\,\mathrm{ns}$ and the ideal peak position within the 15 ADC readout window at $175\,\mathrm{ns}$, which is why the fine timing delay value of the Phos4 scan is determined as a deviation from this peak position. In the validation step, the delay values determined by the analysis implemented in the online software are written to the L1Calo COOL database for the usage in the energy calibrations. Results for the first fine timing calibration of the Tile calorimeter in preparation for Run 3 are shown in Section 8.2.3. In addition to the calibration, the Phos4 scan gives an overview of the functionality of the system as well as introduced changes and is used to support the identification of problematic TTs.

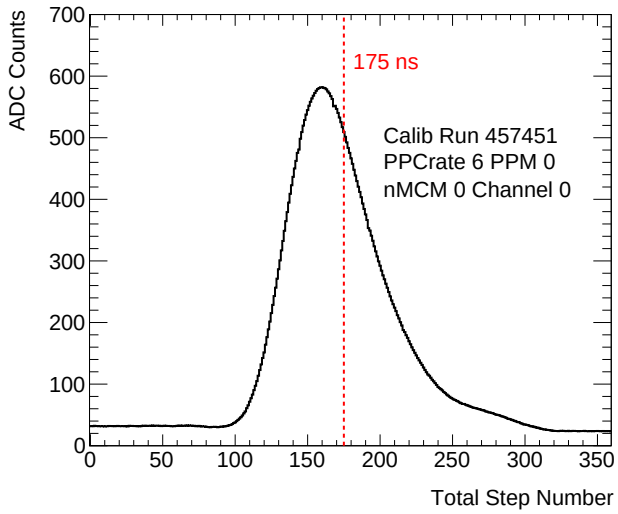

Figure 8.2: Scanned calibration pulse in steps of $1.042\,\mathrm{ns}$ obtained from the Phos4 scan analysis for a Tile TT. The fine delay parameter is determined from the deviation from the pulse's optimal peak position of $175\,\mathrm{ns}$.

8.1.3 Combined Energy Calibration

For a meaningful energy calibration, it is first important to have calibrated the timing for the CIS calibration system in order to guarantee a precise determination of the deposited energy. The energy calibration is then a simple procedure in which pulses with different, fixed, and increasing energies are injected by the CIS. For each energy value, a certain number of events is recorded, which are then analysed by the RampMaker analysis implemented in the offline software.

The RampMaker creates, as the name suggests and as shown in Figure 8.3, a ramp from the recorded events in which the L1Calo transverse energy $E_{\mathrm{T}}^{\mathrm{L1Calo}}$, calculated from the maximum of the recorded ADC values, is plotted against the calorimeter transverse energy $E_{\mathrm{T}}^{\mathrm{Calo}}$, calculated from the calorimeter cell energies corresponding to one TT. A linear fit is performed on the data points, the slope of which is used to derive the raw energy calibration gains. The determined gains are first manually written into the L1Calo COOL database during the validation process, if so decided, and then used in the VGA of the receivers for the physics data taking as described in Section 3.1.1.1 to realise an initial energy calibration at receiver level.

The entire energy calibration routine is executed in three different runs, the difference being the raw energy calibration gains loaded in the calibration configuration. In the first and third run, a gain of 1 is loaded for each receiver, which assumes that there is a

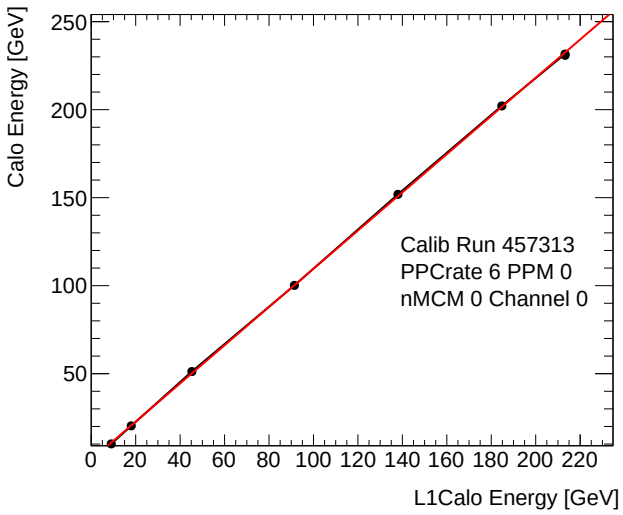

Figure 8.3: Energy ramp for a Tile TT from the analysis of the RampMaker. The L1Calo transverse energy calculated from the maximum ADC value read out is plotted against the Calo transverse energy calculated from the sum of the energies of the calorimeter cells belonging to a TT. The slope of the ramp is used to derive the raw energy calibration gain for the energy calibration on receiver level of the individual TT.

perfect linear dependency between L1Calo and Calo transverse energies. New raw energy calibration gains are determined with this method, whereby the run is only repeated to test and ensure stability.
During configuration, the second run loads the raw energy calibration gains from the database, which is used to check the quality of the current gains. Initial energy calibration results for the Tile L1Calo system can be found in Section 8.2.4. Like the Phos4 scan, the various energy calibration runs can also be used to identify introduced changes to the system and to find problematic TTs.

8.2 Recommissioning Steps of the Legacy L1Calo System

In LS2 between 2018 and 2021, the L1Calo system was kept operational except for a few short shutdown phases. During this time, standalone and combined calibrations were carried out at regular intervals to check the functionality of the legacy system and to detect possible issues at an early stage. Furthermore, the so-called *Milestone Weeks* (M-Weeks) started in May 2020, during which all ATLAS sub-systems attempted to achieve previously set goals in combined tests. The combined tests included cosmic runs[7], high-rate runs,

[7]Described in Section 8.2.1

splashes[8], first collisions[9], but also combined individual sub-system tests, such as L1Calo with the calorimeters together, or runs of individual systems in the ATLAS environment. In total, 12 M-Weeks were carried out until March 2022, followed by weeks of continuous tests until the start of Run 3 in July 2022. These weeks were of utmost importance, not only for the recommissioning of the legacy system, but also for the commissioning of the Phase-1 system, which is described in the next chapter.
Besides the challenge of running the legacy L1Calo system again combined with all sub-systems in ATLAS after about 2 years, it also experienced significant modifications that made the recommissioning necessary.
For the L1Calo Tile system, the installation of the TREX modules in May 2021 resulted in a major change to the legacy system. This was initially followed by a series of standalone tests to verify functionality, including the standalone PPM DAC and Pedestal scans, as well as the verification of the real-time legacy trigger path to the CP and JEP systems to ensure error-free transmission of the real-time data. More information about the tests performed can be found in [11].
After the initial standalone tests, the first combined ones with the Tile calorimeter were successfully performed, including combined pulsing tests as well as timing and energy calibrations. During M-Week 8 in June 2021, the TREX boards were also tested for the first time in the ATLAS environment. In several overnight cosmic and high-rate runs, the error-free transmission of the real-time data to the CP and JEP system was confirmed. Furthermore, in high-rate runs in which the sub-systems are read out at a high L1A rate, a $100\,\mathrm{kHz}$ legacy readout via the TREX to the legacy RODs was achieved.
Before M-Week 8, the ALTI modules were introduced for the L1Calo system and in September for the Tile system, which had a profound impact on the physics data taking timing and the complete calibration routine of the legacy L1Calo system. For the physics data taking timing, an attempt was made to correct the expected shifts introduced by the ALTI. Data from various runs of the M-Weeks were also analysed to further recommission the L1Calo system, including cosmic runs, splashes, and initial test collisions.

8.2.1 Cosmic Runs

During the M-Weeks, a large number of so-called cosmic runs were carried out. These reflect special runs in which muons originating from cosmic particles hitting the atmosphere flying through the detector are triggered. However, due to the low deposited

[8] Described in Section 8.2.2.1
[9] Described in Section 8.2.2.2

energies of the muons in the calorimeters, only a small amount of low-energy signals occur in the readout of the L1Calo system.
Nevertheless, the combined running of the different sub-systems in the ATLAS partition are tested in these runs. Furthermore, the recorded data allows the execution of simple sanity checks of the L1Calo system. First, however, data access to the legacy data had to be ensured. For this purpose, a ntuple production software package was developed in the L1Calo offline software using the Athena environment as described in Section 7.3. The initial code allowed access to the PPM readout, calorimeter cell E_{T} values, and various trigger information from the CTP readout. With the ntuple production package it was possible to create smaller data sets for cosmic runs and thus perform basic analyses with simple python scripts, as shown in both Figures 8.4(a) and 8.4(b) for cosmic run 404341 after the introduction of the TREX as well as the ALTI.
Figure 8.4(a) shows an η-ϕ map of the coverage of the L1Calo system divided into TTs. An entry is filled if the peak ADC value of a TT exceeds a threshold of 50 ADC counts corresponding to about $4.5\,\mathrm{GeV}$, which ensures that low-energy noise is filtered out. These η-ϕ maps are a good way to check the general functionality of the L1Calo system and also to detect possible noisy TTs whose high energy noise would lead to possible false triggers. In this case, it is obvious that most of the high E_{T} cosmic particle hits occur in the barrel region of the calorimeters. On the one hand, this can be attributed to the larger detector volume of the Tile calorimeter with a coverage of $|\eta| < 1.7$ and the associated greater probability of the energy deposition of the muons. On the other hand, when calculating the E_{T} values from the deposited energies E, the multiplication with $\frac{1}{\cosh(\eta)}$ results in smaller transverse energies E_{T} for larger η values in the L1Calo system, which supports the statement of the distribution shown. In addition, one TT with more than 1000 entries stands out and was classified as a possible noisy TT. It was checked and treated after analysis with further tests, some of which are described in Section 8.2.6.
The second Figure 8.4(b) shows a simple pulse with the 5 ADC readout of a Tile calorimeter TT. This analysis was done to check if the peak is still in the middle of the readout window and has a standard pulse shape after the introduction of the TREX as well as the ALTI. In this case, a pulse was recorded that was in line with expectations, indicating a functioning L1Calo system.

8.2.2 Pilot Beam

M-Week 10 in October 2021 was a unique one and was called the *Pilot Beam* period, which spanned over two weeks and allowed a number of different special runs and first

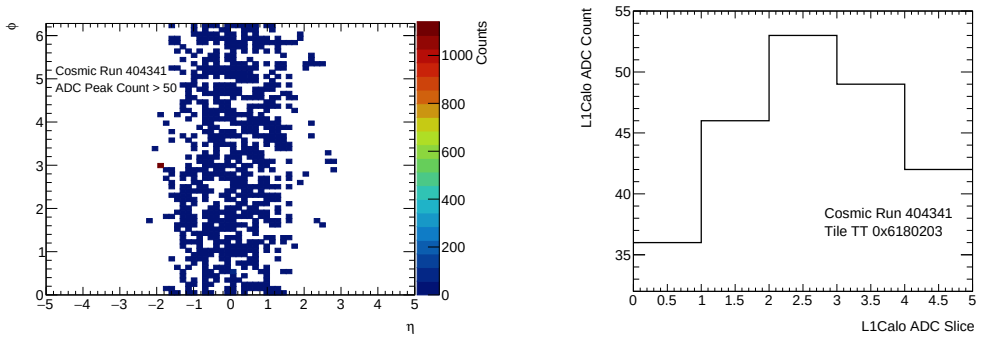

(a) η-ϕ map with ADC Peak Count > 50 **(b)** Cosmic Tile TT Pulse

Figure 8.4: Overview of performed sanity checks from cosmic run 404341. Figure (a) shows an η-ϕ map of all events with ADC peak count > 50. A presumably noisy TT with a high number of entries can be identified. Furthermore, the increased number of entries in the barrel region of the detector is expected from muons during a cosmic run. Figure (b) shows an ADC pulse of a Tile calorimeter TT, whose peak is centred in the readout window and has an expected pulse shape.

collisions. Prior to this, a first timing calibration was introduced for the normal physics data taking, which tried to predict the shift of the timing due to the changes in the legacy system, especially the switch to ALTI and the installation of the TREX, as best as possible. In addition, a change had to be made to the timing parameters of the TT on the C-side of the L1Calo system to account for the open detector on the C-side during the pilot beam period due to the upcoming installation of the NSW. Of particular interest for L1Calo in the first week were the so-called splashes, which will be explained in more detail in the next section. In the second week, the awaited first collisions took place, which are described in Section 8.2.2.2.

8.2.2.1 Splashes & Initial Timing Checks

There were a total of three sessions of splashes in the pilot run period. During these special runs, the LHC beam is "splashed" into the collimators, which normally serve as protection for the beam tubes as well as magnets and are closed for the splashes, at a distance of about $100\,\mathrm{m}$ from the ATLAS experiment, causing a shower of high-energy particles to fly through the entire detector. In the case of L1Calo, these showers were used to check the general functionality of the system and, above all, the initial timing for the physics data taking. The splashes are predestined for a check of the initial fine timing calibration for physics data taking, as almost each cell of the calorimeter is hit during a splash, because of the high-energy particle shower, and thus a timing parameter can be determined for each TT. To determine the fine timing, an analysis was used that was

already introduced for Run 1 and is described in detail in [85].
In summary, the analysis first performs a signal fit, as shown in Figure 8.1, on the read out PPM ADC values. The time of the maximum of the fit is then determined and compared with the ideal position in the centre of the ADC readout window. The difference forms the fine timing parameter of the TT, which is finally written to the L1Calo COOL database for the usage in physics data taking in the validation process.
For the initial timing analysis, however, only one session was used in order to check the implemented initial set of fine timing parameters for the collisions in the second week. There are two different splash settings, referred to in the following as *Beam 1* and *Beam 2*, related to the beam that is shot into the collimator. Beam 1 rotates clockwise in the LHC and hits a collimator on the A-side of the ATLAS detector, resulting in a shower of particles from the A-side. In order to record a signal for the timing analysis in each TT, a so-called *Ring-of-Fire* is set, which describes a region on the C-side of the L1Calo system for Beam 1 with which the incoming particles are triggered. If the Ring-of-Fire was not set, the L1Calo system would trigger too early on signals of the TT on the A-side and only partial signals would be recorded for the TT on the C-side.
Beam 2 rotates counterclockwise in the LHC, so there is a shower of particles from the C-side. The Ring-of-Fire is set on the A-side in the L1Calo system for Beam 2.
Figure 8.5 shows an η-ϕ map from a splash of Beam 1 in the hadronic layer of the L1Calo system, displayed with the L1Calo mapping tool implemented in the online software. The ADC values in the central time slice of the 15 ADC readout window are shown, read out at a frequency of $80\,\mathrm{MHz}$. It can be seen that almost each TT contains a signal with which a timing analysis can be carried out. The differences in the ADC values are mainly due to the position of the TT within the detector, as the ADC signal peak is shifted accordingly and is not located everywhere in the central time slice.
These shifts are corrected for in the timing analysis by including the time-of-flight of the particles from the shower, which is necessary because the particles do not originate from the interaction point inside the detector but about $100\,\mathrm{m}$ away from it. In addition, besides the direct changes to the timing parameters for the open C-side, a correction was introduced within the analysis.
The offsets from the ideal input timing delays in the L1Calo PPMs obtained from the timing analysis for one of the first two splash runs with both beams for the hadronic layer are shown in Figure 8.6. Overall, it is illustrated that the calculated offsets from the ideal timing delays are rather small, and the previously estimated values represent a good approximation. In the case of the very forward region $|\eta| > 3.2$, the large offsets can be explained by large systematic errors in the time-of-flight corrections. Finally, due

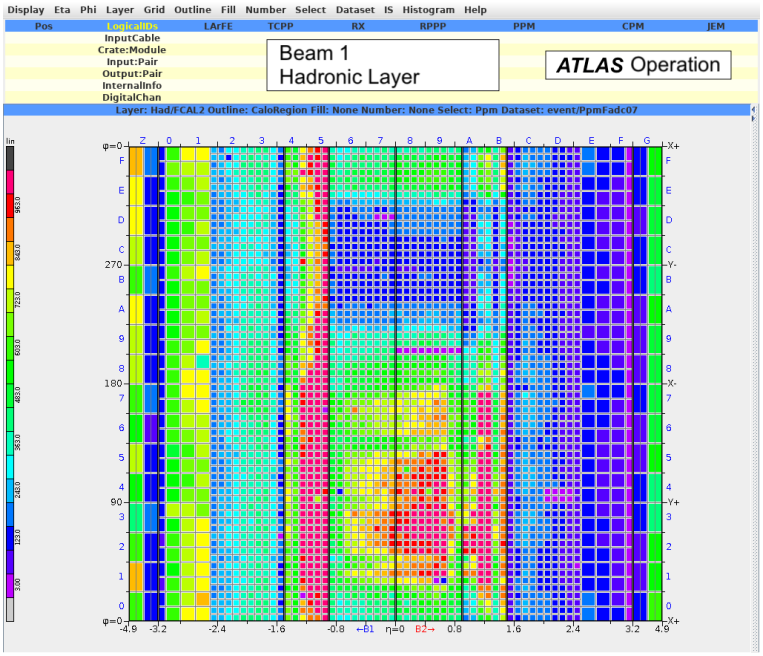

Figure 8.5: η-ϕ map from the L1Calo mapping tool for the hadronic layer during a splash of Beam 1 in run 405495. Shown is the ADC value of the central ADC slice of the readout window. It is visible that all TT show an energy deposition due to the particle shower of the splash. Taken from [82].

to the good results for both the electromagnetic and the hadronic layers, it was decided to keep the timing delays for the upcoming first collisions.

8.2.2.2 First Collisions

The second week of the pilot beam period resulted in the first collisions within the experiments since 2018. In total, there were six stable beam runs, which is declared when the LHC beam has been optimally prepared for use in physics data taking. However, the collisions had a very low centre-of-mass energy $\sqrt{s}$ of $900\,\mathrm{GeV}$, which corresponds to the injection energy of the SPS into the LHC, with mostly two colliding bunches. This resulted in low-energy collision products, allowing only low-energy L1Calo triggers to be tested. In addition, the small number of colliding bunches resulted in a limited data set. The limitations due to the early phase of the recommissioning of the LHC therefore allowed, in addition to the system test of the L1Calo trigger during the first collisions after about three years, various sanity checks as well as testing of the Athena data monitoring implemented in the offline software.
Figure 8.7(a) shows an η-ϕ map of the hadronic layer of the L1Calo system, which is automatically generated as part of the Athena offline monitoring framework. It illustrates

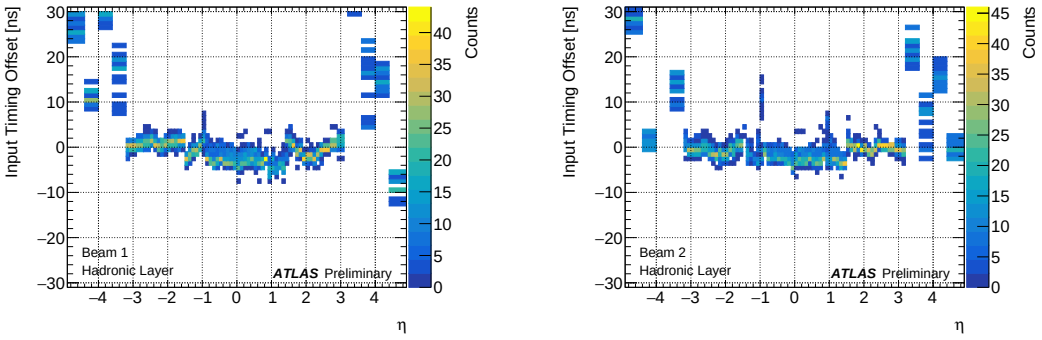

(a) Hadronic Splash Timing Beam 1 **(b)** Hadronic Splash Timing Beam 2

Figure 8.6: Illustration of the offsets from the input ideal timing delays in the L1Calo PPMs plotted as a function of η. Shown are the offsets, calculated from the timing analysis, for the hadronic layer for Beam 1 in (a) and for Beam 2 in (b). All in all, the system showed reasonable timing settings. The huge deviation in $|\eta| > 3.2$ can be attributed to large systematic errors in the time-of-flight corrections necessary for the timing analysis. Taken from [82].

a hit map that is filled if the TT peak ADC value of the triggered time slice exceeds 50 ADC counts, corresponding to about $4.5\,\mathrm{GeV}$. It is clearly visible that only a small number of TTs exceeds the 50 ADC counts at all. In addition, an η range of about five η stripes containing a large number of hits is identifiable. An explanation for this is the open C-side of the ATLAS detector during the pilot beam period due to the installation of the NSW, as the transverse energy E_T is artificially boosted to higher energies, due to the incorrect η location of the TT when converting from energy E to E_T.
Figure 8.7(b) shows another Tile TT pulse, but this time with the 11 ADC readout with a sampling frequency of $80\,\mathrm{MHz}$ used for the first collisions. The ADC peak is in the middle of the readout window, indicating good timing, and has a pulse shape expected for Tile TT signals.
Further cross-checks performed with the data from the first collisions confirm the observation of reasonable timing and pulse shapes, as well as expected L1Calo trigger rates. All in all, the summary of the 2021 pilot beam period was that the legacy L1Calo system is in a reasonable state after three years without any beam. However, it was also noted that further work needed to be done, such as the energy calibration, to bring the L1Calo system into the best possible condition for the upcoming physics data taking.

8.2.3 Initial Tile Timing Calibration

For an initial energy calibration at receiver level of the Tile L1Calo system, first the timing of the calibration with the CIS had to be determined. However, this was challenging,

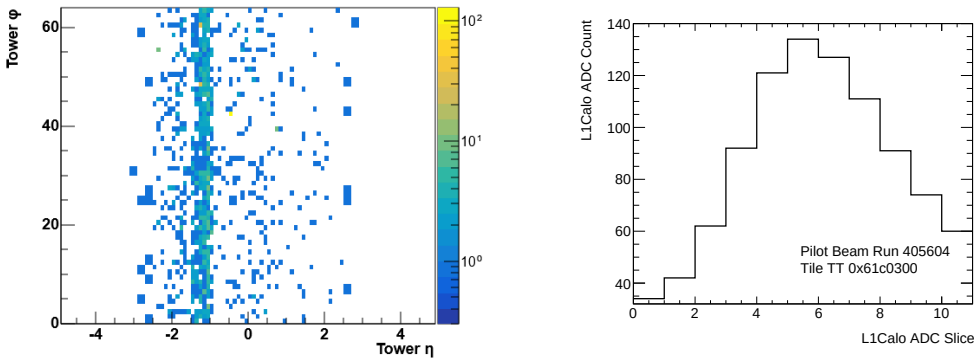

(a) Athena Monitoring η-ϕ map

(b) Pilot Beam Tile TT Pulse

Figure 8.7: Overview of performed sanity checks from run 405604 during the pilot beam period. Figure (a) shows an η-ϕ map from the Athena monitoring of events with a maximum ADC value of a TT within the hadronic layer above 50 ADC counts. A region of increased activity can be identified, which is due to the open C-side of the ATLAS detector during the pilot beam. Taken and modified from the Athena offline monitoring [86, 87]. Figure (b) shows an ADC pulse of a Tile TT whose peak is as intended centred in the readout window.

especially due to the introduction of the ALTI into the already special setup of the TTC system during the CIS calibrations.

The TTC system of the Tile calorimeter is generally divided into four regions, the LB A-side and C-side and the EB A-side and C-side, each of which has its own ALTI system. In normal physics data taking, all ALTI systems are in *slave* mode and receive the TTC signals from the CTP system. For combined calibrations, where the CTP system is not available, the LB A-side ALTI system acts as the so-called *master* and therefore as the source of the TTC signals. It sends for the calibrations the pulse trigger signals to the CIS, delivers the TTC signals, including the L1As, to the other Tile calorimeter TTC systems, which are still in slave mode, but also to the L1Calo system. More information about the setup can be found in [88]. Further complicating the implementation of the ALTI in the special calibration setup were the regular updates of the ALTI software and firmware during the commissioning phase. This led to frequent changes in the TTC systems used for the calibrations, which resulted in a multitude of changes and issues, such as shifts in the timing, but also to partially or completely missing calibration pulses. Consequently, this caused a lengthy testing, development, and debugging phase with constant updates of the ALTI, timings, and calibrations until the first working and combined timing calibration of the Tile L1Calo system was performed in April 2022.

The calibration was done in two steps. First, the coarse timing parameters that determine the depth of the FIFO on the PPM (as explained in Section 3.1.1.2) and therefore shift

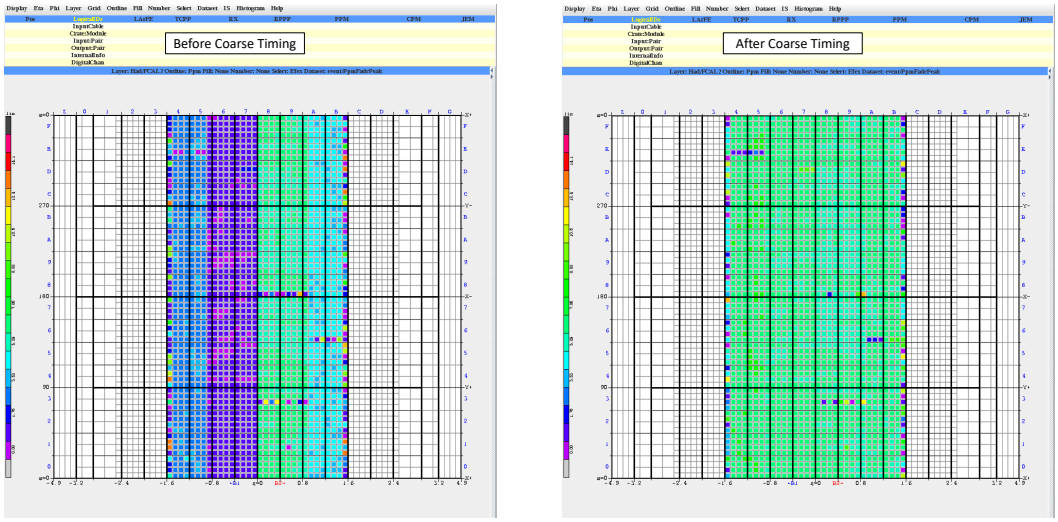

(a) ADC Peak Position before Coarse Timing **(b)** ADC Peak Position after Coarse Timing

Figure 8.8: Adjustment of the Tile calorimeter TTs coarse timing. Figure (a) shows the ADC peak position within the readout window of the Tile calorimeter TTs using the L1Calo mapping tool before adjusting the coarse timing. The coarse timing was afterwards tuned in such a way that the peak position of all regions is mainly in the centre of the readout window. Figure (b) shows the ADC peak position after adjusting the coarse timing with mostly uniform peak positions.

the signal in one BC steps were adjusted in the L1Calo COOL database. However, it is only possible to adapt the coarse timing of the Tile calorimeter TTs globally or depending on the region from which the signal originates, whereby the division corresponds to the four regions of the Tile TTC system. Figure 8.8(a) shows the Tile calorimeter TT signals and their ADC peak position with the L1Calo mapping tool before adjusting the coarse timing parameters, for which events of a Tile L1Calo Phos4 scan were used. It can be clearly seen that the peak position after the profound changes, especially by the ALTI, differs considerably depending on the four different TTC system regions. The peak position of the EB C-side is mostly at the third or fourth ADC slice, whereas the LB C-side is at the border of the readout window at the zero or first position. On the A-side, the LB is already in the targeted range of the peak position from six to seven, whereby the EB is at the fourth or fifth position. This discrepancy was eliminated by the adjustment of the coarse timing parameters so that finally the signal peaks of all TTs in the different regions of the Tile calorimeter are in the middle of the readout window, with the peak at the seventh ADC slice. There are few outliers with a peak position of six, but this is easily compensated for by the subsequent fine timing calibration. Figure 8.8(b) shows the peak position after adjusting the coarse timing.
The second step forms the Phos4 scan fine timing calibration as described in Section 8.1.2.

For the initial calibration, run 416362 was used, the results of which were presented in several overview histograms, a selection is shown in Figure 8.9, and validated.
Figure 8.9(a) shows the difference of the determined fine timing parameters with those in the database since 2018. Once again, the various detector regions and the large differences due to the changes caused by the ATLI are clearly recognisable. Furthermore, some large outlier TTs are visible, which are mostly due to the fact that the newly determined coarse timing parameters lead to strongly changed fine timing parameters for some TTs, although the combined timing correction, which is called *Fulldelay* and allows an overview of the overall timing status of the TTs, remains similar. Another factor that explains the large outliers is the possibility to change the used edge of the sampling clock to digitise the signals, which can also lead to a larger change in the fine timing parameter. More information can be found in [83].
Figure 8.9(b) shows the difference of the newly determined Fulldelay with the one in the database. Again, the differentiation of the individual Tile TTC system regions can be seen, whereby the TT of the separated regions all have a similar Fulldelay, which supports the previously made statement of the large influence of the coarse timing on the fine timing and of the changed used sampling edge of some TTs.
During the analysis of the Phos4 scan, further histograms are created that allow an overview of TTs that do not pass the analysis and therefore cannot be assigned any fine timing parameter, for example due to missing pulses or unconventional pulse shapes. These are considered and treated with the methods described in Section 8.2.6 for noisy and problematic TTs. An exception are the TTs of the *Tile demonstrator* (LB A-side drawer 14 TT 1-9), which had to be calibrated separately, as described in Section 8.2.5.

8.2.4 Initial Tile Energy Calibration

After the Tile L1Calo CIS calibration system was timed in, the energy calibration was performed. The procedure described in Section 8.1.3 was used to determine the raw energy calibration gains, which are loaded into the L1Calo COOL database in the validation process after a thorough evaluation. The raw energy calibration gains are used in the VGA of the receivers for an initial energy calibration.
In June 2022, the results of the energy calibration based on run 424429 were validated for the first time since 2018. Similar to the Phos4 scan, this was preceded by a longer testing, development, and debugging phase, mainly due to the introduction of the ALTI in the special TTC setup for the calibrations. A special feature of the first validated energy

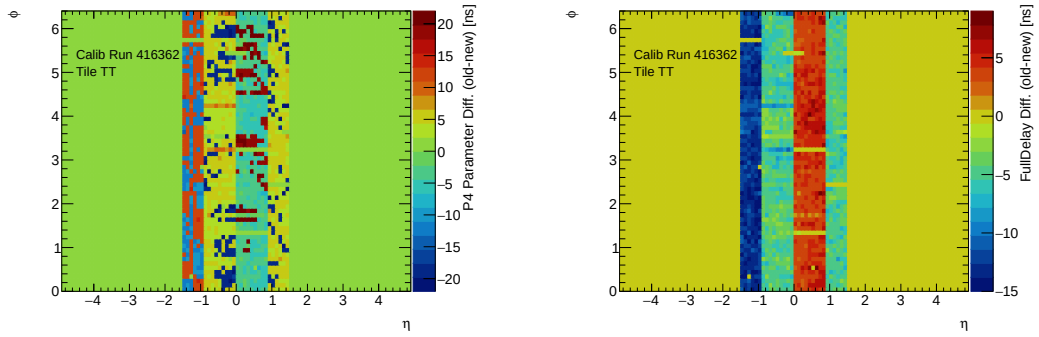

(a) Difference of Fine Timing Parameters

(b) Difference of Fulldelay Parameters

Figure 8.9: Results of the initial Tile Phos4 scan timing calibration. Figure (a) shows the difference between the fine timing parameters determined in the Phos4 Scan analysis and those loaded in the database. Figure (b) shows the difference of the combination of fine and coarse timing, namely Fulldelay, from the determined ones and those loaded in the database. In general, a shift can be seen according to the respective regions.

calibration run was that a hard approach was taken against noisy Tile TTs by masking a number of PMTs of the Tile calorimeter so that their outputs no longer contribute to the respective TT signal. The procedure is considered in more detail in Section 8.2.6.
Figure 8.10(a) shows an η-ϕ map of the determined raw energy calibration gains for the Tile calorimeter TTs. In general, the gains of the EB are higher than those of the LB. Furthermore, there are missing white spots that indicate problematic TTs, since no raw energy calibration gain could be determined for these, which in turn can be used for the investigation of problematic TTs described in Section 8.2.6. An exception is again the Tile demonstrator.
Figure 8.10(b) shows an η-ϕ map of the difference between calculated gains and the 2018 gains loaded in the database, normalised to them. The figure gives a good overview of the changes within the almost four years. In general, however, the changes are moderate, with a small trend of lower raw energy calibration gains, possibly due to the recovery from radiation damage of the Tile PMTs during the shutdown period. In addition, some stronger outliers can be detected, which are also plotted by the analysis in a separate histogram in case of a deviation from the previous reference gain in the database of more than $10\,\%$. These TTs are checked again before the validation procedure and, if problems are detected, their gains are initially left unchanged and investigated further.
After the initial energy calibration of the Tile L1Calo system, it underwent another major update before the first physics data taking, in which the hard approach of masking the PMTs was discarded and changed L1Calo noise cuts were used instead. In addition, the calibration of the demonstrator was introduced in this update.

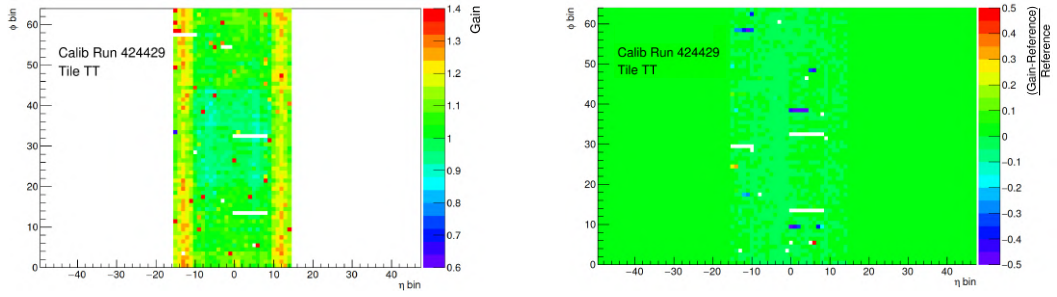

(a) Raw Energy Calibration Gains **(b)** Difference of Raw Energy Calibration Gains

Figure 8.10: Results of the initial Tile energy calibration. Figure (a) illustrates the Tile TT raw energy calibration gains of the first validated Tile energy calibration after Run 2. Figure (b) shows the difference of the newly calculated gains with those loaded in the database from Run 2. In general, slightly lower gains can be seen with some outliers, which however were examined in detail before validation.

8.2.5 Tile Demonstrator Calibration

The Tile demonstrator [89] was installed in 2019 for a small part of the Tile calorimeter (LB A-side drawer 14 TT 1-9), which in total provides the signals of nine TTs, and serves as a test module of the new electronics for the Phase-2 upgrade of the Tile calorimeter planned after Run 3.

Due to the changes in the electronics of the Tile calorimeter introduced by the demonstrator, which also affect the TTC system and leads to a delay of the CIS pulses, it was detected during the debugging phase of the combined calibrations that the TTs of the Tile demonstrator did not show any pulses in the L1Calo readout window. This shift cannot be compensated with the capabilities of the L1Calo system, so for a calibration of the demonstrator, the pulses of the CIS are shifted by 61 BCs through the Tile calorimeter CIS configuration to be within the readout window of the L1Calo system. However, the shift is only possible for whole TTC regions, which is why the remaining TT pulses of the LB A-side are shifted outside the readout window and therefore a timing and energy calibration carried out specifically for the demonstrator becomes necessary. Accordingly, a demonstrator timing calibration was first performed and the calculated fine timing parameters validated. The raw energy calibration gains were then determined and validated in a separate energy calibration.

8.2.6 Noisy & Problematic Trigger Towers

A large part of the recommissioning work was the identification, analysis, and treatment of noisy and problematic TTs. These can generally be divided into different categories, which, however, may overlap.

- Noisy TTs: Noisy TTs receive additional noise from an external source at some point up to the L1Calo system. In general, noisy TTs can be divided into low-energy and high-energy noisy TTs. The low-energy noise is below or just above the standard noise cuts of the PPM. In most cases, it does not trigger important unprescaled L1Calo trigger items and is therefore not critical for stable data taking. The high-energy noise is in most cases fatal for physics data taking and must be prevented at all costs.

- Problematic TTs: Problematic TTs have generally a wide variety of technical problems. These include TTs whose associated Tile calorimeter regions are switched off due to technical problems and therefore do not lead to any signal in the L1Calo system. But also TTs with unusual pulse shapes or TTs that lead to faulty behaviour due to defective hardware within the L1Calo system. These TTs mostly do not contribute to the trigger decision because of their faulty behaviour, which is why they may affect the performance of the L1Calo system.

- TTs with calibration issues: TTs with calibration issues do not function in the CIS or are miscalibrated, which leads in general to a reduction in the performance of the L1Calo system.

In order to identify the various problematic TTs from the different categories and further narrow down the problem, the expert has a wide range of tools at his disposal.

- Calibrations: The simplest and most convenient tools are the standalone and combined calibrations. With the standalone calibrations, mainly hardware problems of the PPMs and there especially of the nMCMs can be identified. The combined calibrations inevitably lead to the identification of TTs that do not function in the CIS system or are miscalibrated. Furthermore, any kind of problematic TT can usually be identified by the shapes of the read out pulses and calibration results, as seen in Figure 8.11(a). In addition, it is possible to inspect the analogue pulses during a combined calibration at receiver level with an oscilloscope installed in USA15, which allows a more detailed analysis of TTs that have been declared problematic. In addition, during the calibration runs with the help of the L1Calo mapping tool, various rates can be displayed, such as the input rates of the PPMs with the energy of signals above a certain energy threshold, with which various noisy TTs can be identified.

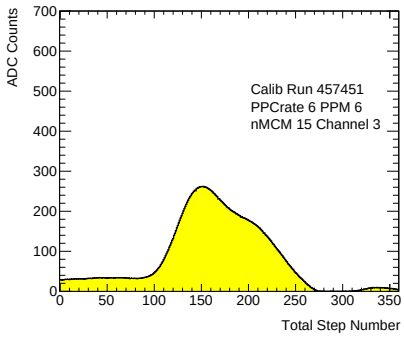

(a) Problematic TT during Phos4 Scan

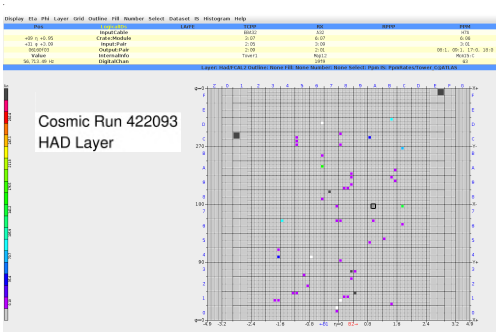

(b) Noisy TT Investigations during Cosmic Run

Figure 8.11: Selection of two possibilities for the identification of problematic or noisy TT. Figure (a) displays a problematic Tile TT identified during a Phos4 scan. The TT shows a deformed pulse shape and in further tests revealed an additional high-energy noise, which led to the TT being masked. Figure (b) illustrates the L1Calo mapping tool during a cosmic run. It is visible that some Tile TTs have high kHz PPM input rates (indicated in black), which led to follow-up investigations and subsequent masking of some of these TTs.

- Combined runs: For combined runs with CIS pulses on the one hand, but also without any kind of pulses on the other hand, the oscilloscope and the L1Calo mapping tool are also used. The combined run with CIS pulses has the advantage of flexibility and no time restriction compared to the tests during the calibrations. The combined runs without any pulses are excellent for finding noisy TTs.

- ATLAS runs: Analysis of signals and rates from different runs in the ATLAS system provide another way to identify and investigate noisy or problematic TT. These include cosmic runs and also normal physics data taking runs. The cosmic runs provide an excellent opportunity to identify noisy TTs by analysing the read out data or using the L1Calo mapping tool to detect TTs with increased rate due to noise, as shown in the example in Figure 8.11(b).
  Signal analysis and rate studies of normal physics data taking additionally allow a way to detect high-energy noisy TTs. In addition, miscalibrated TTs show unusual local performance in the analysis or offline Athena monitoring plots, allowing detection of them.

After identifying the noisy, problematic or even miscalibrated TTs, there are a number of ways to act against them, which are explained in more detail below:

- Physical interventions: The first method includes all interventions of a physical nature, such as repairs and replacement of defective hardware, most notably the replacement of faulty nMCMs or the various repairs to the Tile calorimeter, which

can help to eliminate all kinds of noisy, problematic or miscalibrated TTs. But also the cleaning of cable connectors falls under this category, which is mainly used for noisy TTs, since metal dust has already occurred in the connectors, which have introduced external noise into the system. However, physical interventions during physics data taking, especially of the Tile calorimeter, are only possible to a limited extent or not at all, which is why these are mostly carried out in technical shutdowns at the end of the respective year.

- PMT masking: PMT masking offers a way to exclude individual PMTs of the Tile calorimeter when forming the TTs, filtering out noisy PMTs and preventing the noise from being passed on to the L1Calo system. However, this method is a hard approach to tackle noisy TTs and is only used in exceptional cases, because part of the signal deposited in the calorimeter is lost. An attempt is made to correct for this loss with the help of the combined energy calibration.

- PPM masking & noise cuts: As already described in Section 3.1.1.2, it is possible to set a programmable noise cut for each individual TT when using the LUTs, whereby the specific LUT output is set to 0 for signals with energies below the noise cut. In addition, the possibility of masking TTs exists by setting the LUT output to 0 regardless of the signal energy.
  For each TT of the L1Calo system, a certain noise cut is set, in general for the Tile calorimeter signals intended for the CPMs it is $1\,\mathrm{GeV}$. For low-energy noisy TTs that slightly exceed the noise cuts, the cut can be set higher, to prevent low-energy noise in the legacy CP and JEP, while the interesting high-energy signals of the TTs are still available. For high-energy noisy TTs, however, at a certain point it is pointless to increase the noise cuts further, which is why they are usually masked. This process represents the biggest cut in the system and should only be carried out in extreme cases, as the signals of the masked TTs are lost and therefore usually affect the general performance of the L1Calo system. The masking process can also be performed during a run for possible sudden occurrences of increased rates of a TT, in order to avoid endangering the data taking.

- Calibration with physics data: Miscalibrated TTs or TTs that do not work in the CIS system can be calibrated with a special analysis with physics data.

In the course of the recommissioning, a total of more than 100 noisy, problematic, and miscalibrated Tile TTs were found with the described identification methods. Finally, a large part of the problems could be treated or solved, so that at the time of writing this

thesis only seven out of 1920 Tile TTs were still masked. In addition, there are some TTs that have experienced minor calibration issues, most of which have been resolved and will continue to be closely monitored.

8.2.7 Early Collisions

At the end of the recalibration and recommissioning phase before the actual physics data taking started, the calibrated L1Calo system was checked for its timing and energy calibration by analysing the first high-energy test collisions of Run 3. Furthermore, the various Athena monitoring histograms during the test collisions gave an overview of the system, whereby a generally good functionality was observed.

8.2.7.1 Timing Calibration

The timing of the L1Calo system was checked again with the previously described timing analysis in first high-energy test collisions at the start of Run 3. Since the splashes, the timing has not been further adjusted, which is why a timing shift of at least $3\,\mathrm{ns}$ was expected due to further ALTI updates.
For the analysis, the L1Calo1 DAODs[10] of run 427394 with the centre-of-mass energy of $\sqrt{s} = 13.6\,\mathrm{TeV}$ but only two colliding bunches was used, which was executed with a L1Calo readout configuration of $80\,\mathrm{MHz}$ with 11+1 readout mode.
Figure 8.12 shows the result of the timing analysis for the Tile LB. A deviation from the ideal timing of about $5\,\mathrm{ns}$ was identified. This shift was also detected for all other calorimeter regions, which is why a global shift of the physics data taking timing by $5\,\mathrm{ns}$ was applied shortly after the analysis. Furthermore, special TT-dependent shifts were applied to adjust the timing as best as possible.
The timing was checked after correction in multiple normal physics data taking runs from 431178 to 431812 with centre of mass energy of $\sqrt{s} = 13.6\,\mathrm{TeV}$ and 2400 colliding bunches. However, the run settings only allow a L1Calo readout configuration of $40\,\mathrm{MHz}$ with 5+1 readout mode, resulting in a reduced resolution of the timing analysis. For the analysis, L1Calo1 DAODs of the EGZ DRAWD with, among others, a $Z \rightarrow e^+e^-$ preselection was used. Figure 8.12 shows the results, where it is clear that the calculated timing delays have shifted and are nearly centred around $0\,\mathrm{ns}$, reflecting an almost ideal timing calibration.

[10] Introduced in Section 7.3

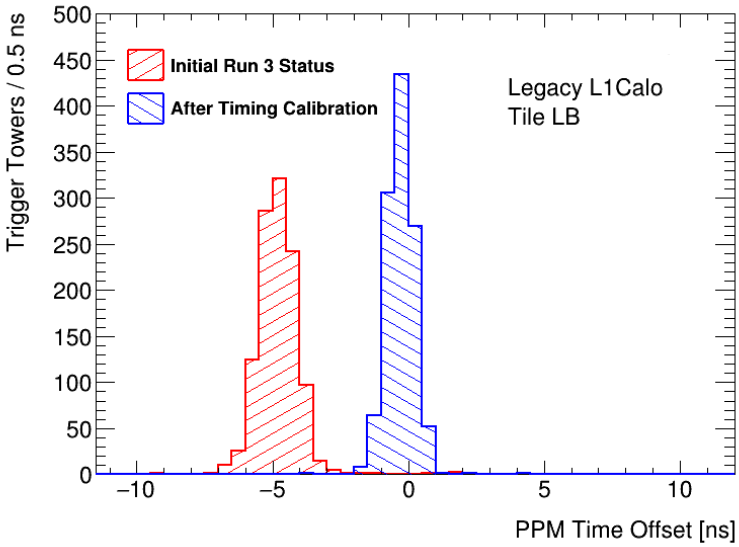

Figure 8.12: Comparison between the PPM input timing offset for the Tile LB TTs of run 427394 before the timing adjustment (red) and of runs 431178 to 431812 after the timing adjustment (blue). Before the timing was calibrated, there was a global offset due to the introduction of the Phase-1 upgrade of all calorimeter TTs of about $5\,\mathrm{ns}$ determined by a special timing analysis. For this, a global correction was introduced, which led to a centring of the TT offset around 0. Taken from [90].

8.2.7.2 Energy Calibration

The energy calibration was also checked with the L1Calo1 EGZ DAODs of runs 431178 to 431812 at the beginning of Run 3. With these, the demonstrator calibration, the withdrawal of the PMT intervention, and also the optimal timing setting had already been implemented. For verification, similar to the RampMaker, the L1Calo ADC peak transverse energy $E_{\mathrm{T}}^{\mathrm{L1Calo}}$ was first plotted against the sum of the Tile calorimeter cell energies $E_{\mathrm{T}}^{\mathrm{Calo}}$ for a TT, which is shown in Figure 8.13(a). Saturated as well as signals from masked TTs were filtered out during the analysis. In addition, a 50 ADC count cut was applied to the L1Calo ADC values and a threshold of $1\,\mathrm{GeV}$ was set to the calorimeter transverse energy to filter out low energy events that would be either way rejected by the noise cuts. Overall, a slight over-calibration of the L1Calo system on receiver level is visible. This observation is also confirmed by Figure 8.13(b), where the ratio between L1Calo and calorimeter E_{T} is plotted. It shows that the L1Calo system was over-calibrated at the receiver level by about $7\,\%$ for the Tile calorimeter TTs.
In addition, the energy calibration at receiver level was compared with that at LUT level, which is shown in Figure 8.14. In the analysis, the same thresholds were applied as in the previous studies with an additional cut to the saturation of the CP LUT at $127.5\,\mathrm{GeV}$.

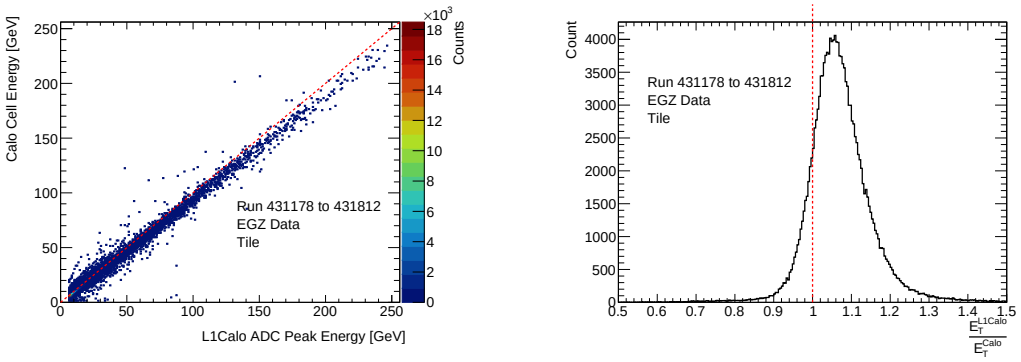

(a) L1Calo to Calo Transverse Energy Ramp **(b)** Ratio of L1Calo to Calo Transverse Energy

Figure 8.13: Comparisons between the L1Calo $E_{\mathrm{T}}^{\mathrm{L1Calo}}$ and Calo $E_{\mathrm{T}}^{\mathrm{Calo}}$ transverse energy. Figure (a) shows a ramp between the transverse energy $E_{\mathrm{T}}^{\mathrm{L1Calo}}$ determined from the L1Calo TT ADC peak and the Tile calorimeter transverse energy $E_{\mathrm{T}}^{\mathrm{Calo}}$ consisting of the cell energies of the Tile calorimeter summed for one TT. In Figure (b) the ratio of the two transverse energies is plotted. In both figures, a slight over-calibration of the L1Calo system on receiver level is visible.

The comparison was performed in dependence of η and shows a similar over-calibration as before and in general a good agreement of the ADC and LUT values with, however, smaller deviations in the EB region, which may be due to outdated parameters in the energy calibration on LUT level.

All in all, the first energy calibration for Run 3 showed a good performance despite a slight over-calibration, which is why it was initially decided to keep the calibration for the first data taking period of Run 3 and to intervene only in individual cases, if necessary.

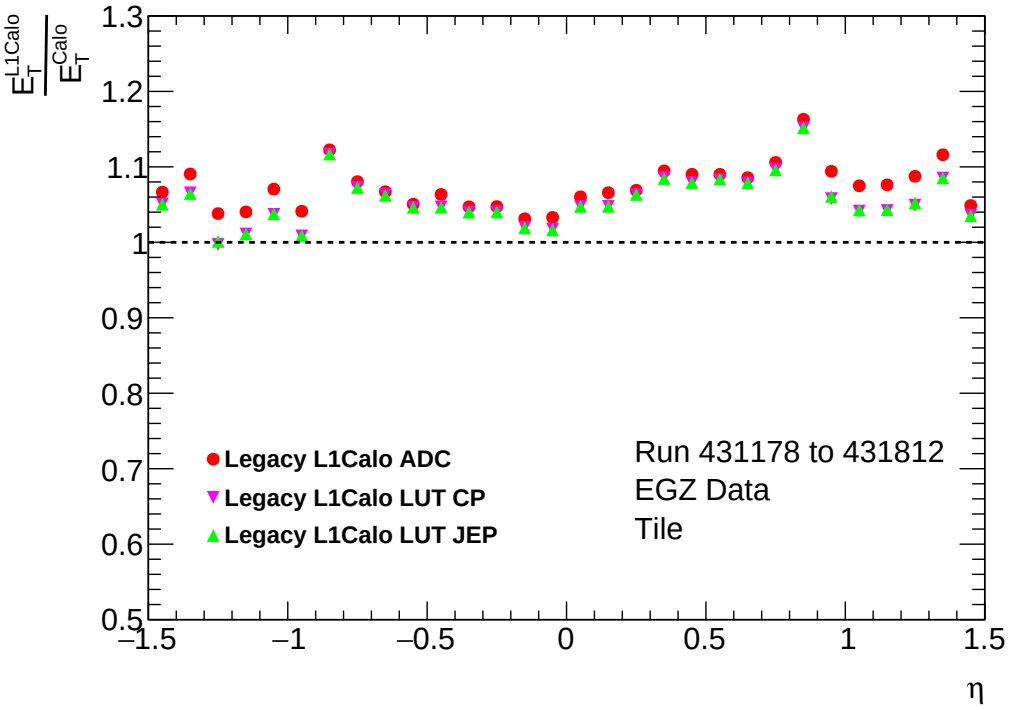

Figure 8.14: Ratio between mean values of the different L1Calo transverse energies $E_{\mathrm{T}}^{\mathrm{L1Calo}}$ and Tile calorimeter transverse energy $E_{\mathrm{T}}^{\mathrm{Calo}}$ as a function of η. On the one hand, the ratio from the mean of the L1Calo transverse energy calculated from the maximum of the ADC values and the Tile calorimeter transverse energies determined from the cell energy sum for a TT is compared, which allows a statement about the quality of the energy calibration on receiver level. On the other hand, the ratio from the mean values of the transverse energies calculated according to the LUT of the PPM for the CP and the JEP system, which reflect the transverse energies after the final energy calibration of the L1Calo system, and the Tile calorimeter transverse energy is determined. Again, a small over-calibration of the L1Calo system is found at both levels with good overlap between ADC and LUT ratios and only a slight deviation in the EB of the Tile calorimeter.

9 Phase-1 Commissioning

After the installation of the Phase-1 components in the electronic caverns of the ATLAS experiment, which is described in Section 4.4, the commissioning of the Phase-1 hardware within the ATLAS system was started. The focus was on stable operation and an error-free real-time path with properly functional algorithms, for which a stable readout of the individual components was required for debugging and validation reasons. To achieve this, the various runs of the M-weeks, the pilot beam, and also the complete first data taking period, which was still triggered by the legacy system, were used.
With a more and more stable overall system including a functioning readout, the interest in the analysis of the read out data and comparisons with the legacy system grew. In the following chapter, only analyses and comparisons with the eFEX system are considered, although similar comparisons were made for the other Phase-1 systems.
Section 9.1 looks at simple sanity checks of the inputs of the eFEX system. Section 9.2 then gives an overview of comparisons between TOBs, while Section 9.3 first explains the tag-and-probe method and then compares trigger efficiencies between legacy and eFEX EM triggers.

9.1 eFEX Input Comparisons

One of the first studies performed with Phase-1 data was the comparison between the TREX output and the corresponding eFEX input, which is shown in Figure 9.1(a). The comparison is intended to show that the data sent by the TREX also arrives at the input of the eFEX with a $100\,\%$ match. For this purpose, collision run 427394 was used again, which has a low L1A rate due to the low number of colliding bunches and therefore allows the readout of the eFEX input data, which is restricted to a low L1A rate. The read out objects of both systems were matched with their respective η-ϕ coordinates and their E_{T} values were plotted against each other. The FELIX-SW ROD readout of both systems was used. The figure shows an exact match of both systems, which confirms perfect transmission and mapping.
The η-ϕ matching method is suitable for the coarser Tile TTs, as their coordinates overlapped perfectly. Comparing the outputs of the LATOMEs from the LAr calorimeter to the corresponding eFEX input is more challenging since an η-ϕ coordinate is associated with multiple SCs in different layers. Accordingly, a matching based on unique identification numbers was implemented within the analysis software, the results of which for

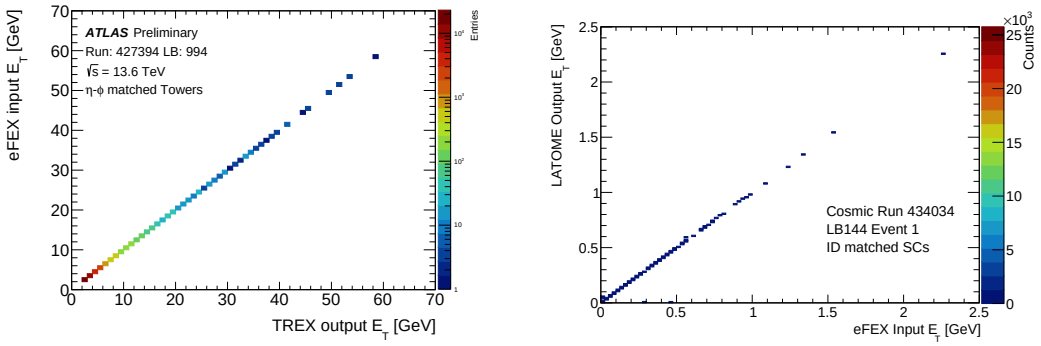

(a) TREX Output to eFEX Input Comparison **(b)** LAr Output to eFEX Input Comparison

Figure 9.1: Calorimeter output to eFEX input comparisons. Figure (a) shows the perfect match of the transverse energy of the TREX output readout object to the transverse energy of the eFEX input readout object. The objects were matched based on their η-ϕ coordinates. Taken from [82]. In contrast, Figure (b) illustrates the comparison of the transverse energies from the LAr output to the eFEX input with a matching based on identification numbers of the readout objects. Small deviations due to different energy scales are visible. Furthermore, two larger outliers are shown, which can be explained by issues in the LAr SC masking.

cosmic run 434034 are shown in Figure 9.4(b). The eFEX input E_{T} is plotted against the LATOME output E_{T} and again shows a good match, albeit with small deviations. These can generally be attributed to different energy resolutions of the two readouts. The LATOME output readout has a resolution of $12.5\,\mathrm{MeV}$ [91] and the eFEX input readout has a variable resolution due to a multi-linear energy encoding[11]. In the case of the comparisons shown here for low transverse energies in the cosmic run, an energy resolution of $25\,\mathrm{MeV}$ results for the eFEX input readout up to an E_{T} of $5.6\,\mathrm{GeV}$.

Furthermore, two major outliers with zero E_{T} values of the LATOME output readout and non-zero E_{T} values for the eFEX input readout were detected, which were caused by a wrong treatment of masked SCs in the LAr calorimeter. This problem was solved within the further commissioning process. In addition, the analysis verified the mapping between the LAr calorimeter and the eFEX system based on an identification number matching. In the course of the analysis, various noise studies were also carried out to identify noisy SCs of the LAr calorimeter system.

Overall, the sanity comparisons between calorimeter output and eFEX input showed very good agreement with minor problems, which were resolved during the commissioning.

[11] Further details can be found in [91].

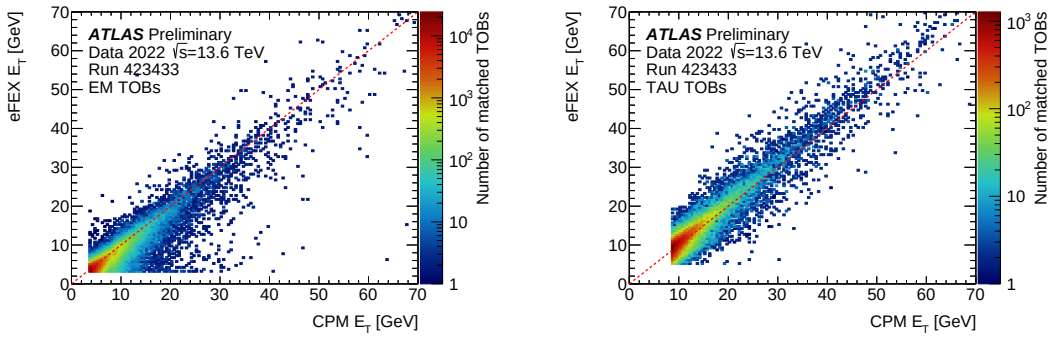

(a) Legacy EM TOB to eFEX EM TOB Comparison

(b) Legacy τ TOB to eFEX τ TOB Comparison

Figure 9.2: Legacy to eFEX EM and τ TOB comparisons. The two comparisons were made with data from the non-stable beam run 423433 and half ϕ coverage as well as $|\eta| < 0.8$ due to constraints of the eFEX system. The matching of the TOBs was performed based on their η-ϕ coordinates with maximal deviation of $\Delta R < 0.2$. In general, there is good agreement between the $E_{\text{T,TOB}}$ values of the two TOB types from both systems. Taken from [82].

9.2 eFEX TOB Comparisons

Both the legacy CP system and the eFEX system identify e/γ and τ candidates with specific algorithms, whereby their comparison allows a deeper understanding of their similarities as well as differences, thus significantly advancing the commissioning of the new eFEX system.

For this reason, a comparison between the $E_{\text{T,TOB}}$ values of the TOBs determined by the legacy CP system and the eFEX Phase-1 system was performed. The comparison was done separately for the two running algorithms, the e/γ algorithm and the τ algorithm, and their resulting EM or TAU TOBs, respectively. The matching of the TOBs of both systems is based on their η-ϕ coordinates. Due to different seed determination algorithms and their resulting distinct coordinates associated to the TOBs, a deviation of $\Delta R < 0.2$ of both systems was allowed. The comparisons for EM and TAU TOBs were performed before the start of Run 3 in non-stable beam test collisions of run 423433 and the results are shown in Figure 9.2. Due to the ongoing commissioning of the eFEX system, there was only access to data with $|\eta| < 0.8$ and half the ϕ coverage. Nevertheless, the $E_{\text{T,TOB}}$ values of the matching TOBs of both systems generally showed good correlation. Deviations can be attributed to the different algorithms and their TOB $E_{\text{T,TOB}}$ determination as well as the masked SCs in the new Phase-1 LAr system.

9.3 Trigger Efficiency Comparisons

The performance of a trigger is primarily determined by two decisive variables, on the one hand the trigger rate and on the other hand the trigger efficiency, whereby both influence each other.
The trigger rate of a specific item is generally tried to be kept low in order to ensure a high variety of the various trigger items in the L1 trigger menu and not to exceed the maximum L1A rate of $100\,\mathrm{kHz}$. However, at the same time, the goal is to maximise the trigger efficiency, which describes the probability that an event of interest was triggered by a certain trigger item for further processing and finally for offline analysis, and therefore significantly determines the performance of a trigger. It usually depends on multiple variables.
In the following, the tag-and-probe method used to determine the trigger efficiencies is explained. Afterwards, comparisons of the single electron trigger efficiencies between the legacy CP EM trigger and the eFEX EM trigger for the identification of e/γ candidates are shown.

9.3.1 The Tag-and-Probe Method

The tag-and-probe method [92] uses characteristic signatures to determine trigger efficiencies. In the case of the initial comparisons of single electron trigger efficiencies between the legacy and Phase-1 L1Calo system that will be described in Section 9.3.2, the characteristic signature of $\mathrm{Z} \rightarrow e^+e^-$ decays was used, which serves as an example in the following to explain the method.
The method first ensures that the event under consideration is an event of the Z decay. This requires, for example, that the event has at least two offline reconstructed electron candidates with opposite charge and an invariant mass m_{ee} of the two electrons with the highest transverse momentum p_T of approximately the Z mass. If the criteria are met, further strict selection criteria, such as a transverse momentum p_T cut, are applied to the electron with the highest transverse momentum p_T, also called leading electron or tag electron, to further filter out background events and ensure that this electron originates from the Z decay.
After the tag electron has passed all the criteria, the electron with the second highest transverse momentum p_T, also called subleading or *probe* electron, is very likely to be an electron of the Z decay. The unbiased probe electrons are then used to check a wide range of test criteria. In the case of L1Calo and the single electron trigger efficiency, for

example, it is checked whether a TOB, which was found by the CP or eFEX system, associated with the probe electron exists. The corresponding efficiency ϵ is then determined using

$$\epsilon = \frac{N_{\text{probe,test}}}{N_{\text{probe,all}}}, \tag{9.1}$$

with the total number $N_{\text{probe,all}}$ of probe electrons after the tag selection and the number $N_{\text{probe,test}}$ of probe electrons that fulfilled the test criteria.
This method was used with different configurations and test criteria to determine all the efficiencies shown in this thesis. More on the various criteria used for the tag electron as well as for the probe electron will be explained in the next section.

9.3.2 First eFEX Efficiency Comparisons

The very first trigger efficiency comparisons between the legacy and Phase-1 L1Calo system were performed using the CP EM trigger and the eFEX EM trigger to identify e/γ candidates. The initial studies used L1Calo1 DAODs produced from EGZ preselected DRAWDs[12] of run 438532, which contain, among other things, characteristic signatures of Z $\rightarrow e^+e^-$ decays.
However, the preselected EGZ DRAWDs also contain other signatures, such as Z $\rightarrow e^+e^-\gamma$, Z $\rightarrow \mu^+\mu^-\gamma$, and Z $\rightarrow e^{\pm}fe^{\mp}$ with *fe* for the forward electron, which usually have different preselection criteria. Nevertheless, the preselection reduces the data set to a multitude of possible Z $\rightarrow e^+e^-$ decay events, allows a faster analysis due to the smaller data set, and fulfils the requirement for characteristic signatures of the tag-and-probe method.
In the preselection for the Z $\rightarrow e^+e^-$ decays, initial loose event selection criteria are applied to the dataset. At least two offline reconstructed electrons are required, each with a transverse momentum of $p_{\text{T}} > 20\,\text{GeV}$. In addition, a selection of the electrons based on the likelihood method *medium* electron identification is performed.
The likelihood method is an analysis that, depending on various criteria such as shower shape information or track-cluster matching, assigns a value to an electron that indicates the probability that the reconstructed electron is a real electron and not, for example, a photon or hadronic jet. Depending on the assigned values, the electrons are classified within three different working points: *tight*, *medium*, and *loose*. As the names suggest, electrons within the tight working point reflect the electrons with the highest probability of being a real electron, with decreasing probability towards medium and loose. More information about the method can be found in [93]. Furthermore, a first invariant mass

[12] Introduced in Section 7.3.

cut of $m_{ee} > 55\,\mathrm{GeV}$ is applied in the preselection for both electrons.
In addition to the criteria already applied during the dataset preselection, further selection criteria were introduced, particularly for the tag electron, in order to filter out the other signatures present in the EGZ data and, above all, to ensure clean $Z \to e^+e^-$ events for the determination of the efficiencies [93]. Most of the following selection criteria were chosen according to the recommendation of the ATLAS e/γ group, which can be found in [94]:

- Triggered Legacy L1Calo Trigger: The first requirement for the respective event under consideration is that it was triggered by the CP EM trigger *L1_EM22VHI*. The L1_EM22VHI trigger item describes the first unprescaled single electron trigger of the legacy L1Calo system. The name can be divided into different components. *L1* stands for Level-1, *EM* for the type of trigger, in this case the EM trigger for e/γ candidates, and the 22 indicates the TOB transverse energy $E_{\mathrm{T,TOB}}$ threshold of the trigger. The threshold is variable in the legacy system in the η coordinate to compensate for the different detector responses, this is indicated by the *V* in the trigger item's name. The other two initials *H* and *I* indicate that the isolation criteria already described in Section 3.1.1.3, H for hadronic isolation and I for electromagnetic isolation, have been applied to the respective trigger item.
  With this first selection criterion, for example, the events with $Z \to \mu^+\mu^-\gamma$ signatures contained in the EGZ DAODs are most likely filtered out directly.

- Two Electrons: The event should contain at least two electrons in the calorimeter barrel.

- Invariant Mass: In addition to the loose invariant mass cut of $55\,\mathrm{GeV} < m_{ee}$ already used in the preselection, a stricter cut of $76.2\,\mathrm{GeV} < m_{ee} < 106.2\,\mathrm{GeV}$ is applied in the selection to the two electrons of the tag-and-probe method.

- Opposite Charge: Because of the charge neutrality of the Z boson, the two offline reconstructed electrons are expected to have an opposite charge.

- Tag Electron p_{T} Cut: In addition to the p_{T} cut in the preselection for the $Z \to e^+e^-$, a tag electron cut of $p_{\mathrm{T}} > 20\,\mathrm{GeV}$ was used to filter out, for example, $Z \to e^+e^-\gamma$ signature events in the EGZ dataset, to which only a p_{T} cut of $15\,\mathrm{GeV}$ was applied in the preselection.

- Tag Electron Calorimeter Cluster: The tag electrons should only be in the barrel region and therefore have a calorimeter cluster of $|\eta|$ <2.47 to match the coverage

of the CP and eFEX systems for which the EM trigger efficiencies were calculated.

- Tag Electron Tight Identification: For the tag electrons, an additional tight identification criteria was applied on top of the medium likelihood identification criteria already used on the data set during the Z $\rightarrow e^+e^-$ preselection to further increase the probability that the tag electron is a real electron and thus select even cleaner Z $\rightarrow e^+e^-$ events.

- Tag Electron Loose Isolation: Loose requirements are placed on the tag electron for its isolation, which are calculated in two different ways to filter out hadronic jets in particular. One is the calorimeter-based isolation, where the transverse energy E_{T} deposited in the calorimeter cells is taken into account in a cone of size ΔR around the electron position. On the other hand, the track-based isolation, in which the sum of the transverse momenta p_{T} of the tracks around the electron track are considered.

- Primary Vertex & Tag Electron Track: First, it is required that the event under consideration has a primary vertex. Then the two impact parameters d_0 and z_0 of the tag electron track, which allow a statement of the orientation of the track in transverse (d_0) and longitudinal (z_0) direction in relation to the primary vertex, are used to ensure that the tag electron originates from the primary vertex. For this, the tag electrons must fulfil a d_0 significance of $|d_0/\sigma_{d_0}| < 5$ and must pass $|\Delta z_0 \sin(\theta)| < 0.5\,\mathrm{mm}$. More details about the impact parameters can be found in [95]. The criteria are applied to ensure that only clean and unique tag electrons coming from the Z $\rightarrow e^+e^-$ decay are considered.

- Corresponding EM TOB to Tag Electron: Due to the determination of the L1Calo single electron trigger efficiency, the tag electron must additionally match an EM TOB. In accordance with the required triggered L1_EM22VHI for the event, a legacy EM TOB matched to the tag electron with a maximum position deviation of $\Delta R \leq 0.15$ and with an $E_{\mathrm{T,TOB}}$ exceeding the variable legacy $E_{\mathrm{T,TOB}}$ threshold and passing the electromagnetic as well as the hadronic isolation is required.

After all selection criteria have been successfully passed, the tested electron is declared as a tag electron. Then, the number of associated probe electrons is filled into several η-dependent denominator histograms as a function of the probe electron transverse momentum p_{T}, in order to determine efficiencies separated into different calorimeter regions. For the very first single electron trigger efficiencies, the calorimeters were divided into four different η-dependent regions, the *Inner Barrel* (IB, $|\eta| \leq 0.8$), the *Outer*

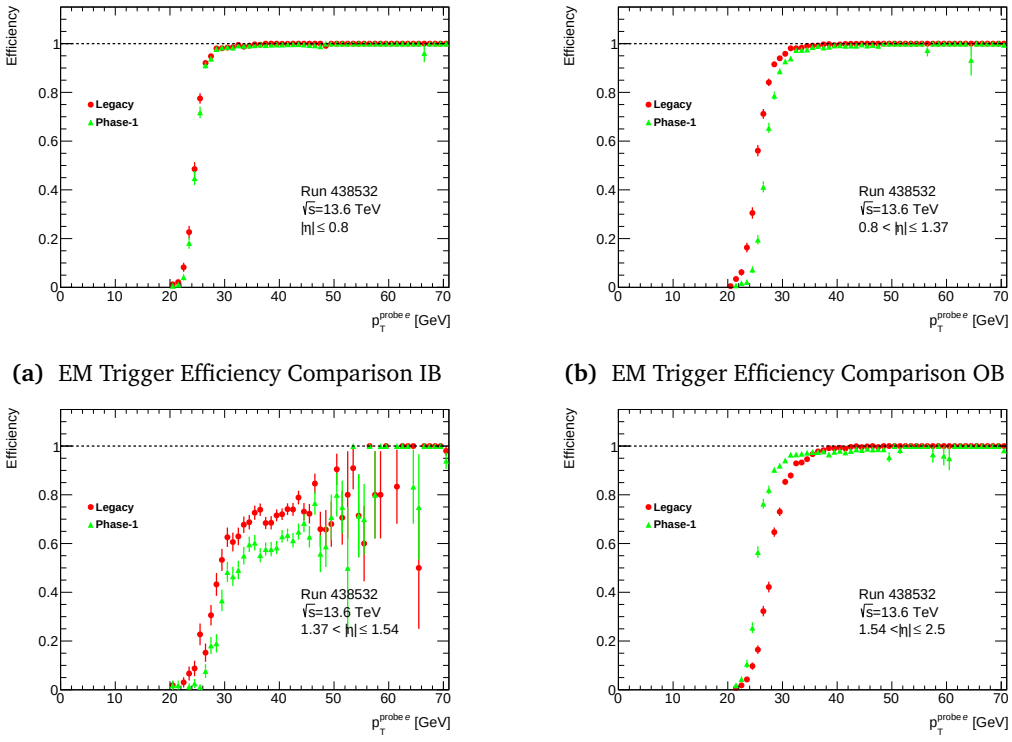

(a) EM Trigger Efficiency Comparison IB

(b) EM Trigger Efficiency Comparison OB

(c) EM Trigger Efficiency Comparison OVL

(d) EM Trigger Efficiency Comparison EC

Figure 9.3: Legacy to eFEX EM trigger efficiency comparison. Shown is the comparison of the very first single electron trigger efficiencies generated by the tag-and-probe method between the legacy system and the eFEX system divided into four different η regions. Data from the EGZ L1Calo1 DAODs of run 438532 were used. The test criterion for the probe electron was that a TOB in the radius $\Delta R \leq 0.15$ with $E_{\mathrm{T,TOB}} \geq 22\,\mathrm{GeV}$ exists. In general, the efficiency of the eFEX EM trigger is comparable to the legacy EM trigger.

Barrel (OB, $0.8 < |\eta| \leq 1.37$), the *Overlap* (OVL, $1.37 < |\eta| \leq 1.54$), and the *Endcap* (EC, $1.54 < |\eta| \leq 2.5$).

The probe electrons are then subjected to selected test criteria, which included finding an associated EM TOB in the CP or eFEX system near the position of the probe electron with $\Delta R \leq 0.15$ and with a transverse energy $E_{\mathrm{T,TOB}} \geq 22\,\mathrm{GeV}$. After passing the test criteria, the number of remaining probe electrons was filled into enumerator histograms as a function of p_{T}.

To determine the efficiencies for both the legacy CP and the Phase-1 eFEX system, the filled histograms were divided according to Equation 9.1 for each region and plotted as a function of the probe electron transverse momentum p_{T}. The resulting so-called *turn-on* curves in Figure 9.3 show the comparison of the trigger efficiencies for the CP and eFEX system for the different regions.

The entire barrel region shows a good match of the efficiency curves of both systems, whereby the turn-on curve for the Phase-1 system in the OB region starts slightly later. However, this may be due to a possible not yet optimal configuration during the early stage of the Phase-1 system. The overlap region is shown in this analysis for completeness, but generally has a rather poor efficiency due to the special geometry as well as the amount of dead material of the region and is not considered further in the following. The efficiency curve in the EC shows a delayed turn-on of the legacy system in relation to the Phase-1 system, which was detected for the first time in this analysis. After prolonged investigation, this was attributed to outdated pulser-to-physics corrections, especially for the EC region of the legacy system with $|\eta| > 2.0$. Due to this fact, for the following efficiency analyses, the EC region were subdivided into the *Inner Endcap* (IEC, $1.54 < |\eta| \leq 2.0$) and the *Outer Endcap* (OEC, $2.0 < |\eta| \leq 2.5$) in order to better illustrate this effect. Furthermore, it can be observed that the eFEX turn-on curve only reaches the plateau for optimal efficiency at higher p_{T} values, which is due to a large number of masked SCs from the Phase-1 LAr calorimeter system especially in the EC region.
In addition to the investigation of the efficiencies, a further comparison of the transverse energies $E_{\mathrm{T,TOB}}$ of the legacy and Phase-1 EM TOBs matched to either the tag or the probe electron was performed in the analysis, which is illustrated in Figure 9.4. The distribution of the $E_{\mathrm{T,TOB}}$ values with the largest accumulation of leading TOBs at about $40\,\mathrm{GeV}$ and with a bulk at $35\,\mathrm{GeV}$ for the subleading TOBs can be attributed to the consideration of $\mathrm{Z} \rightarrow e^{+}e^{-}$ events. The figures show very good agreement between the $E_{\mathrm{T,TOB}}$ of the TOBs from both systems and supports the encouraging observations from the efficiency determination.
All in all, the very first efficiency comparisons show a very good performance of the eFEX as well as the legacy system, with small exceptions such as the pulser-to-physics corrections or several masked SCs. Furthermore, it should be noted that these first efficiency studies did not include isolation or trigger rate considerations, which however received further attention in the analyses of the next section.

9.3.3 eFEX Efficiency Comparisons including Isolation

After the initial efficiency studies, the eFEX EM trigger was further optimised and the isolation parameters were tuned, which opened up the possibility for valid investigations of the efficiencies including isolation. The adjustment was made to reduce the high trigger rates of the isolated eFEX EM trigger caused by untuned and loose isolation threshold parameters of the eFEX e/γ algorithm. In the course of this, the trigger rate of the Phase-

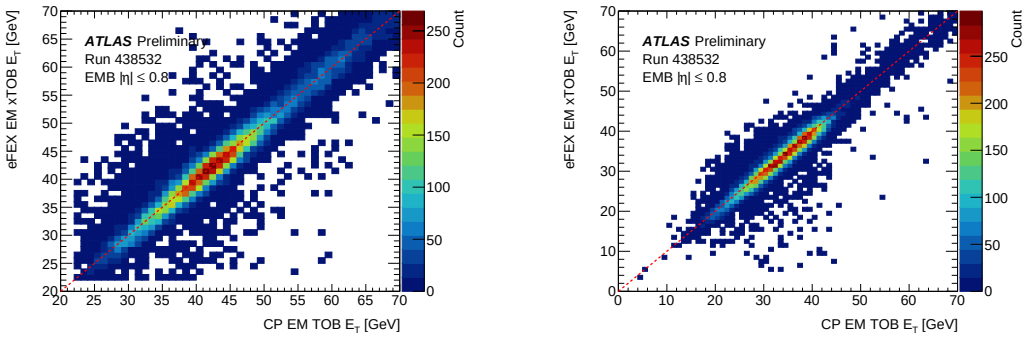

(a) Legacy to eFEX EM Leading TOB Comparison

(b) Legacy to eFEX EM Subleading TOB Comparison

Figure 9.4: Legacy to eFEX EM TOB $E_{\mathrm{T,TOB}}$ comparisons. Figure (a) shows the comparison of the transverse energies of the TOBs matched to the tag electron of the legacy and the eFEX system, whereas Figure (b) shows the same comparison only for the TOBs matched to the probe electron. The data from the EGZ L1Calo1 DAODs of run 438532 were used. In both cases, there is very good correlation between the transverse energies of the EM TOBs from both systems.

1 single electron trigger *L1_eEM26T* was adjusted in run 439798 to that of the already mentioned first unprescaled legacy single electron trigger L1_EM22VHI, thus allowing a valid comparison of the efficiencies of the two trigger items at same rates. The trigger rates before prescale were considered, as the Phase-1 trigger item was fully prescaled due to the ongoing commissioning process. The name of the L1_eEM26T trigger item can be divided into different components, similar to the L1_EM22VHI already explained in Section 9.3.2. *L1* again stands for Level-1, *e* describes the eFEX system, *EM* for the type of trigger, in this case the EM trigger for e/γ candidates, and the *26* indicates the TOB transverse energy $E_{\mathrm{T,TOB}}$ threshold of the trigger, which is constant in the case of the Phase-1 system. The *T* represents the tight isolation working point applied to all three isolation parameters of the e/γ algorithm, more details are explained in Section 4.2.1.1. For the determination of the efficiencies including isolation, it was required to introduce the isolation as a further test criterion, to the probe electron. This results in the TOB matched to the probe electron having to pass the electromagnetic and hadronic isolation of the CP system or the tight working point requirement of all three isolation parameters of the eFEX system, respectively. The comparisons of the efficiencies with and without isolation are shown in Figure 9.5 for the different regions.
In the two barrel sections, the comparison of the efficiencies including isolation shows the strength of the new single electron trigger of the eFEX system, which has a clear higher efficiency in the range of about $24\,\mathrm{GeV}$ to $50\,\mathrm{GeV}$ at the same trigger rate of both systems. This is also consistent with the previously performed simulation studies of the Phase-1

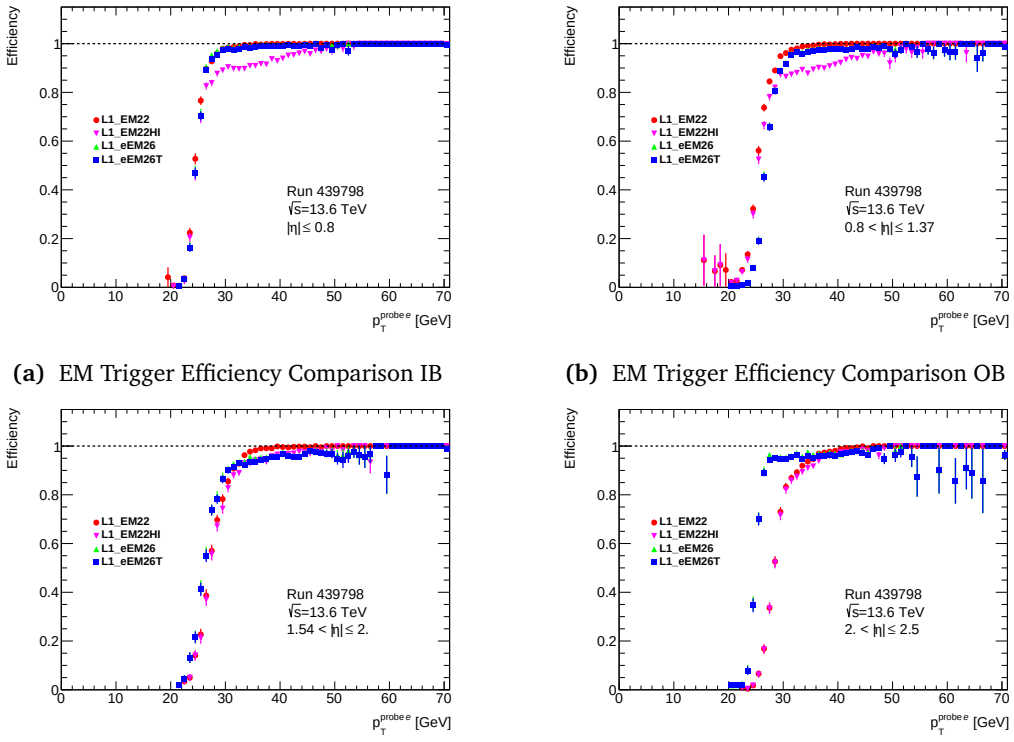

(a) EM Trigger Efficiency Comparison IB

(b) EM Trigger Efficiency Comparison OB

(c) EM Trigger Efficiency Comparison IEC

(d) EM Trigger Efficiency Comparison OEC

Figure 9.5: Legacy to eFEX EM trigger efficiency comparison including isolation. The figures show the single electron trigger efficiencies determined with the tag-and-probe method and the EGZ L1Calo1 DAODs from run 439798, in which the trigger rates of the eFEX L1_eEM26T trigger were matched with that of the L1_EM22VHI legacy trigger. In addition to the efficiencies without isolation, those with isolation are shown, which is applied as a further test criterion in addition to the $22\,\mathrm{GeV}$ $E_{\mathrm{T,TOB}}$ threshold of the EM TOB matched to the probe electron by the condition $\Delta R \leq 0.15$. Here, the strength of the higher efficiency of the eFEX system is particularly evident in the barrel region.

system described in Section 7.4. The OB region shows slightly worse efficiency than IB due to readout problems within two eFEX modules during the run, which also extended into the endcap. In addition, the two separated endcap regions suffered from the same issues explained in Section 9.3.2. Accordingly, the efficiencies of the eFEX system are affected by a large number of masked SCs of the Phase-1 LAr system in this region in particular, while the efficiencies of the legacy system are negatively influenced by the outdated pulser-to-physics corrections, especially in the OEC region.

Note that the constant TOB transverse energy $E_{\mathrm{T,TOB}}$ threshold of $22\,\mathrm{GeV}$ was still used as a test criterion for both systems in the analyses, as Dead Material Corrections (DMCs) have not yet been implemented for the eFEX system that introduce a correction for the different detector responses as a function of η for the eFEX system. For the legacy system,

the varying detector responses are compensated for via the variable $E_{\text{T,TOB}}$ threshold, which is indicated with a V in the name of the trigger item, which is why a fair comparison of the two systems with variable thresholds in the legacy system is only possible with the introduction of the DMCs. The efficiency analyses with DMCs and variable threshold of the legacy system are shown in the following section.

9.3.4 eFEX Efficiency Comparisons including Isolation & Dead Material Corrections

In the next step of the optimisation process of the eFEX EM trigger, the layer- and η-dependent DMCs were introduced in the eFEX system to correct for the different detector responses. Alongside this, additional studies, described in more detail in the following Chapter 10, were performed to further tune the isolation threshold parameters and energy thresholds of the eFEX e/γ algorithm. In addition, studies were carried out for layer- and η-dependent noise cuts, which were previously constant.
The determined results of the studies, including the newly defined $E_{\text{T,TOB}}$ threshold of $25\,\text{GeV}$ for the eFEX trigger, were applied to run 451094. This resulted in a first fully tuned and calibrated implemented version of the eFEX EM trigger L1_eEM26T, whose efficiencies were directly compared to the efficiencies of the legacy EM trigger L1_EM22VHI with variable $E_{\text{T,TOB}}$ thresholds, which is shown in Figure 9.6. This run reflects the status of both systems just before the deactivation of the legacy single electron trigger and the switch to the corresponding eFEX one. The newly determined parameters resulted in a rate of the eFEX L1_eEM26T trigger in run 451094 being about $5\,\text{kHz}$ lower compared to the legacy L1_EM22VHI. Note that the parameters of the L1_eEM26T were first tested and then transferred to the L1_eEM26M trigger item, which forms the first unprescaled single electron trigger of the Phase-1 system, prior to deactivation of the legacy trigger.
According to the adjusted $E_{\text{T,TOB}}$ thresholds for the legacy and eFEX system, the test criteria of the tag-and-probe method for the efficiency calculation had to be modified. For the legacy system, the TOB thresholds variable in η were introduced as test criteria for the TOB matched to the probe electron instead of the former constant $22\,\text{GeV}$ threshold. In the efficiency calculation of the eFEX system, this $22\,\text{GeV}$ TOB threshold for the probe TOBs was instead replaced by a constant $25\,\text{GeV}$ threshold.
The efficiency comparisons of the barrel region in Figure 9.6(a) and 9.6(b) still shows a significantly better efficiency of the eFEX trigger despite the L1 rate reduction.
For the two regions of the endcaps in Figures 9.6(c) and 9.6(d), the influence of a large

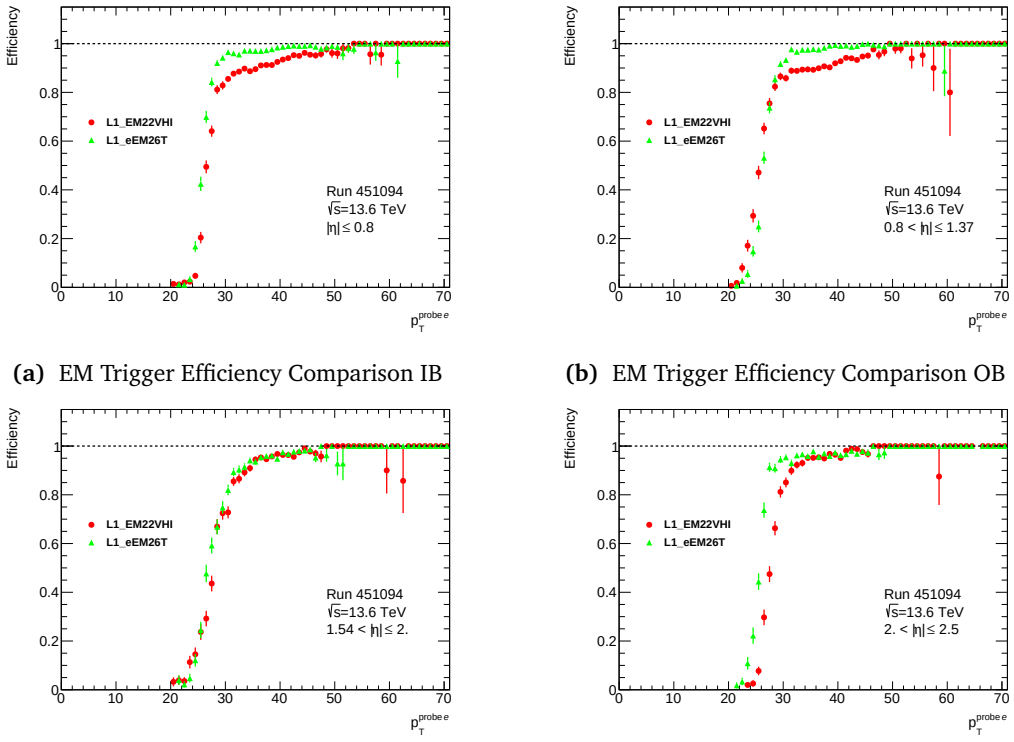

(a) EM Trigger Efficiency Comparison IB

(b) EM Trigger Efficiency Comparison OB

(c) EM Trigger Efficiency Comparison IEC

(d) EM Trigger Efficiency Comparison OEC

Figure 9.6: Legacy to eFEX EM trigger efficiency comparison with tuned eFEX parameters. The figures show the comparison of the single electron trigger efficiencies just before switching to the eFEX system as the main EM trigger. For these studies, various eFEX parameters, including implemented dead material corrections and noise cuts, were tuned and data from the EGZ L1Calo1 DAODs of run 451094 were used with the tag-and-probe method. The test criteria for the probe electron was that an EM TOB was found in the radius $\Delta R \leq 0.15$, which passes the isolation criteria and exceeds the variable $E_{\mathrm{T,TOB}}$ threshold in the case of the legacy system and a threshold of $25\,\mathrm{GeV}$ in the case of the eFEX system. The eFEX continues to show better efficiency, especially in the barrel region, at lower trigger rates than the legacy system.

number of masked SCs of the LAr system on the efficiency of the Phase-1 system is still visible. Nevertheless, the eFEX trigger shows a comparable or better efficiency with a lower L1 rate than the legacy system. Furthermore, it is evident that an attempt was made to update the outdated legacy pulser-to-physics corrections, which resulted in an increase in efficiency of the legacy system, especially in the area of the OEC.

The efficiencies at lower L1 rates generally showed the better performance of the eFEX single electron trigger in relation to the corresponding legacy one, which was a key factor in the decision to switch from the legacy L1_EM22VHI to the eFEX L1_eEM26M as the first unprescaled L1Calo single electron trigger.

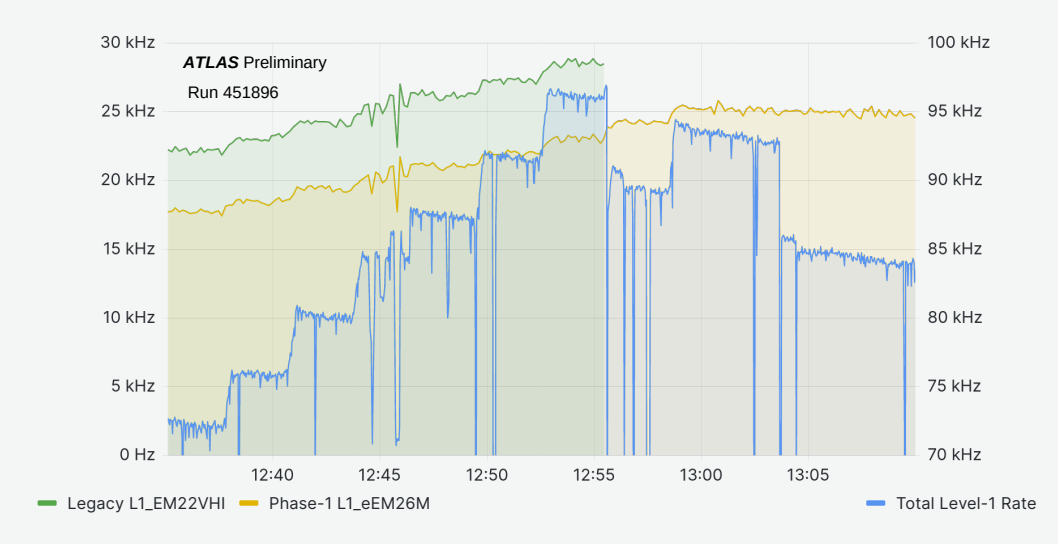

Figure 9.7: Comparison of the trigger rates of L1_EM22VHI, L1_eEM26M and the total L1 rate at the time of deactivation of the legacy L1_EM22VHI trigger. The deactivation of the L1_EM22VHI trigger and the associated change to the L1_eEM26M as the first unprescaled EM trigger of the L1Calo system led to a reduction of the total L1 rate of about $5\,\mathrm{kHz}$. The further steps in the L1 rate can be attributed to further trigger tuning and luminosity increase. Taken from [82].

9.3.5 First Phase-1 EM Trigger

The demonstrated better efficiency at lower L1 rate of the L1_eEM26M eFEX trigger as well as the very good robustness and stable readout of the eFEX system caused the ATLAS experiment to deactivate the legacy EM trigger on 11 May 2023 at 12.55pm [82], as shown in Figure 9.7, and thus completed the switch to the Phase-1 EM trigger as the main single electron trigger of the L1 system. The figure shows the rates of the legacy L1_EM22VHI, the eFEX L1_eEM26M as well as the total L1 rate and consequently the reduction of the L1 rate at the time of deactivation of the legacy EM trigger of about $5\,\mathrm{kHz}$. The other steps within the total L1 rate can be attributed to independent trigger tuning and luminosity increase during the LHC ramp-up.

10 eFEX Parameter Studies

The main goal of the eFEX parameter studies was to push the L1 rate of the eFEX trigger, prior to the deactivation of the first unprescaled single electron trigger L1_EM22VHI from the legacy system and the associated switch to the first unprescaled eFEX single electron trigger L1_eEM26M, further below the level of the legacy system. The aim was to create room for greater variety of the L1 triggers in the L1 trigger menu without exceeding the maximum L1A rate of $100\,\mathrm{kHz}$, while maintaining the higher efficiency, especially in the barrel region of the Phase-1 system. For this purpose, a number of studies have been carried out to tune the various eFEX parameters, which are discussed in more detail in the following.

10.1 eFEX Isolation Parameter and Threshold Studies

First, the isolation parameters and TOB thresholds of the L1_eEM26M trigger were investigated. Furthermore, the influence of the threshold $E_{\mathrm{T,max}}$ was examined, which indicates the $E_{\mathrm{T,TOB}}$ value at which the isolation criteria are no longer applied. This is the case for high-energy electrons and their associated TOBs, since part of the energy deposition takes place in the hadronic calorimeter. In addition, the showers tend to be broader and therefore would not pass the electromagnetic isolation criterion R_η.
For the studies run 440543 was analysed, which was recorded shortly before the end of the first data taking period, and it introduced an initial set of DMCs based on *Monte Carlo* (MC) generated data, which correspond to data simulated by generators according to the Monte Carlo method [96].
First, the efficiencies with different isolation threshold parameters were compared. For this purpose, the tag-and-probe analysis code was extended to include the possibility of redetermining whether a TOB passed the various newly defined isolation thresholds for the three working points. This made it possible to compare efficiencies with a variety of different isolation threshold parameters using only one dataset.
Figure 10.1 shows such a comparison of efficiencies with different isolation thresholds for the whole η coverage of the eFEX system excluding the overlap region from $1.37 < |\eta| \leq 1.54$. In this comparison, the maximum transverse energy $E_{\mathrm{T,max}}$ at which the isolation criteria were still applied was set to $60\,\mathrm{GeV}$ for the eFEX algorithm. The eFEX TOB transverse energy $E_{\mathrm{T,TOB}}$ threshold is set to $25\,\mathrm{GeV}$. As a reference efficiency,

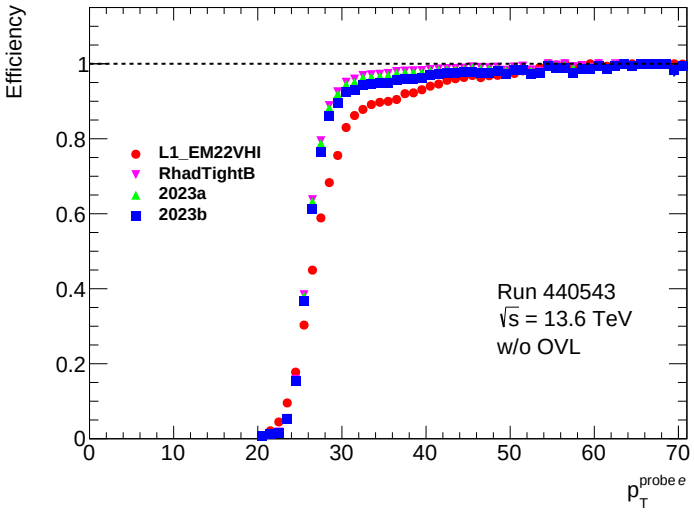

Figure 10.1: Efficiency Studies with different isolation threshold parameters. Shown are efficiencies with different eFEX isolation threshold parameters compared to the legacy L1_EM22VHI trigger using data from the EGZ L1Calo1 DAODS from run 440543 and the tag-and-probe method. For the eFEX EM trigger efficiencies, a matched TOB in radius $\Delta R \leq 0.15$ with $E_{\mathrm{T,TOB}} > 25\,\mathrm{GeV}$ and different isolation criteria were applied to the probe electron as test criteria. The overlap range of $1.37 < |\eta| \leq 1.54$ is excluded from the calculation. From the RhadTightB via the 2023a to the 2023b settings, the thresholds of the isolations become increasingly strict. Nevertheless, all studies show a better efficiency compared to the legacy trigger.

the single electron trigger efficiency of the legacy L1_EM22VHI trigger is shown.
The *RhadTightB* setting describes the isolation threshold parameters set for run 439798 as described in Section 9.3.3, where the trigger rates of the L1_eEM26T were equated to that of the L1_EM22VHI with adjustment of the R_{had} threshold not taking DMCs into account.
During the threshold parameter studies, many different settings were tested. These included the *2023a* setting, which was used for early collisions in 2023 and introduced tighter thresholds of the first unsprescaled Phase-1 single electron trigger L1_eEM26M for R_η, R_{had} and w_s in relation to the L1_eEM26T settings of RhadTightB. The efficiencies with the *2023b* settings that were finally used in the switch from the legacy to the Phase-1 EM trigger described in Sections 9.3.4 and 9.3.5 are also shown in the efficiency comparison. All three threshold parameters were tightened again compared to the 2023a settings. The increasingly tightened isolation thresholds from the RhadTightB via 2023a to 2023b result in a slight decrease in trigger efficiency visible in Figure 10.1. However, in comparison to the legacy L1_EM22VHI trigger, the eFEX triggers with different isolation settings have in general a higher trigger efficiency.
In addition to the isolation threshold parameter efficiency studies, efficiencies with dif-

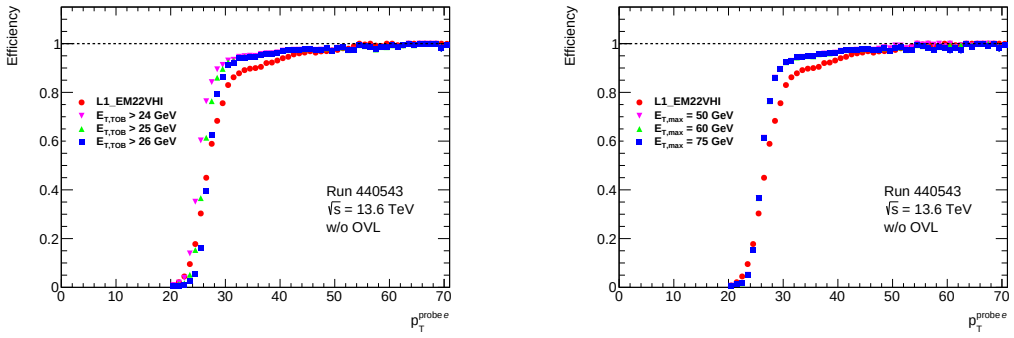

(a) $E_{\mathrm{T,TOB}}$ Threshold Studies

(b) $E_{\mathrm{T,max}}$ Threshold Studies

Figure 10.2: $E_{\mathrm{T,TOB}}$ and $E_{\mathrm{T,max}}$ threshold efficiency studies. In the efficiencies shown, which were generated using the tag-and-probe method and the EGZ L1Calo1 DAOD data from run 440543, the influence of the $E_{\mathrm{T,TOB}}$, indicated in Figure (a), and the $E_{\mathrm{T,max}}$, shown in Figure (b), thresholds on the efficiency was investigated. For the $E_{\mathrm{T,TOB}}$ studies, there is a shift in the efficiency curve depending on the $E_{\mathrm{T,TOB}}$ threshold. For the $E_{\mathrm{T,max}}$ efficiencies, there are only slight differences in the plateau of the curve.

ferent $E_{\mathrm{T,TOB}}$ and $E_{\mathrm{T,max}}$ thresholds were also compared, which are shown in Figure 10.2 for run 440543 and the 2023b isolation threshold settings. In Figure 10.2(a) the trigger efficiencies for various $E_{\mathrm{T,TOB}}$ thresholds are shown. The $E_{\mathrm{T,max}}$ value was kept constant at $60\,\mathrm{GeV}$. It is visible that the lower the $E_{\mathrm{T,TOB}}$ threshold, the earlier the turn-on of the trigger efficiency curve starts. However, different $E_{\mathrm{T,TOB}}$ thresholds tend to only influence the turn-on behaviour up to $30\,\mathrm{GeV}$, after which no significant difference between the efficiencies for the various settings is visible. In the efficiencies for different $E_{\mathrm{T,max}}$ values in Figure 10.2(b), the constant $E_{\mathrm{T,TOB}}$ threshold of $25\,\mathrm{GeV}$ was chosen. In contrast to the $E_{\mathrm{T,TOB}}$ threshold comparisons, there are only minor differences in the plateau of the efficiency curves.

The various efficiency studies have little validity for the performance of the trigger if the L1 rate is not taken into account, which is why a program code to determine various rates with different eFEX parameters was added to the analysis framework. The overall goal was to find an optimal setting of the parameters with the highest possible efficiency at a low L1 rate in order to create space for additional trigger items and thus to ensure a high variety of the L1 trigger menu.

The rate determination is based on data from the so-called *zero-bias* stream, which contains only events triggered by a trigger that fires exactly one LHC orbit after a high-energy L1 EM trigger. This ensures that only completely random events are triggered independent of any implemented trigger item, which is important for an unbiased determination of the rates. The rate of the zero-bias trigger is fixed at about $10\,\mathrm{Hz}$ via prescaling [97].

Table 10.1: Results of rate studies with different sets of eFEX parameters

$E_{\text{T,TOB}}$ [GeV]	24	24	24	25	25	25	26	26	26
$E_{\text{T,max}}$ [GeV]	50	60	75	50	60	75	50	60	75
RhadTightB T [kHz]	31.0	28.1	26.5	27.6	24.7	23.1	26.0	23.1	21.5
2023a M [kHz]	29.6	26.5	24.9	26.4	23.3	21.6	24.8	21.7	20.0
2023b M [kHz]	26.7	23.6	22.0	24.1	21.0	19.3	22.7	19.5	17.9

To speed up the rate determination, event picking was applied to the zero-bias data to filter out events that would not meet the different test criteria for the TOBs by far. This resulted in only selecting events that were triggered by the legacy L1_EM15 trigger before prescaling.
The L1_EM15 is additionally the reference trigger for the rate R determination, which is calculated according to

$$R = R_{\text{ref}} \frac{n}{n_{\text{ref}}}, \tag{10.1}$$

with R_{ref} the rate before prescale of the reference L1_EM15 trigger, which was in the case of run 440543 around $300\,\text{kHz}$, n_{ref} the number of events triggered by the L1_EM15 in the dataset under consideration and with n the number of events satisfying the respective test criterion in the dataset. The various parameters of the efficiency studies for the eFEX EM TOBs were chosen as test criteria and the calculated rates are listed in Table 10.1.
In general, higher $E_{\text{T,TOB}}$ and $E_{\text{T,max}}$ thresholds as well as tighter isolation parameter thresholds result in a lower trigger rate. Considering the determined efficiencies and rates, the $E_{\text{T,TOB}}$ threshold of $25\,\text{GeV}$, the $E_{\text{T,max}}$ of $60\,\text{GeV}$ and the isolation threshold parameters of the 2023b setting were chosen as the optimal setting for the switch to the L1_eEM26M trigger as the first unprescaled single electron trigger of the L1Calo system. The rate of $21\,\text{kHz}$ for the optimal settings is significantly lower than the rate of the legacy L1_EM22VHI, which was determined to be $30.8\,\text{kHz}$.
Note that the rate determination varies depending on the run and its LHC conditions. In addition, the issues with the eFEX readout in run 440543 and some masked SCs of the LAr calorimeter were fixed, resulting in a better efficiency but with higher rate in the Phase-1 system. Another smaller rate increase was caused by the introduction of η- and layer-dependent noise cuts, as described in the next section. All these points explain the described rate reduction of only $5\,\text{kHz}$ at the switch from the legacy EM trigger to the eFEX EM trigger described in Section 9.3.5, which still met the initial rate reduction requirement.

10.2 eFEX Noise Cut Studies

In addition to the studies with the parameters used in the previous section, rate and efficiency studies were also carried out with the eFEX noise cuts. If the transverse energy E_{T} of an input SC from LAr is below these, the E_{T} value is set to 0 in the eFEX system. In the previous analyses, the noise cuts were used as constant thresholds with a value of $800\,\mathrm{MeV}$ for the presampler SCs and with $600\,\mathrm{MeV}$ for the remaining layers, as shown in Figure 10.3. Furthermore, the calculated η- and layer-dependent noise cuts can be seen, whose influence on rate and efficiency of the L1_eEM26M trigger with the optimal settings has been investigated.

These η- and layer-dependent noise cuts were calculated with the data from the zero-bias stream of run 440407. The calculation was split for each η strip as well as layer, and a condition was set that only a certain percentage of the events exceed a threshold, namely the noise cut. This percentage is also called occupancy, whereby noise cuts with $0.5\,\%$ and $1\,\%$ occupancy were calculated for the rate and efficiency studies. Finally, the calculated noise cuts were symmetrised, whereby the lower noise cut value of the two η strips is applied to both them. As shown in Figure 10.3, the determined $0.5\,\%$ occupancy noise cuts are higher than the constant noise cuts only in the presampler and hadronic layer. Otherwise, similar or lower values were calculated. For the $1\,\%$ occupancy noise cuts, only the hadronic layer has higher values compared to the constant thresholds, all other layers show lower values.

To determine the efficiencies and rates with different noise cuts and using the EGZ dataset from run 440543, the TOBs first had to be resimulated with the L1Calo offline simulation for the different sets of noise cuts. The eFEX towers emulated from the LAr calorimeter SC readout, which correspond to the formatted eFEX input, served as the simulation input. Within the simulation, the new noise cuts were then applied to the input and TOBs were simulated.

The resimulated TOBs were used to determine the L1_eM26M efficiencies and rates using the procedures described in the previous section. For both analyses, the optimal parameters found for L1_eEM26M with $E_{\mathrm{T,max}} = 60\,\mathrm{GeV}$, $E_{\mathrm{T,TOB}} > 25\,\mathrm{GeV}$, and the 2023b isolation threshold parameters were used. Figure 10.4 shows the comparison of the determined efficiencies of TOBs with constant noise cuts and η- and layer-dependent noise cuts with $0.5\,\%$ as well as $1\,\%$ occupancy.

There are only slight differences in the turn-on range of the efficiency curve visible. This can mainly be attributed to the large difference of the noise cuts and the $E_{\mathrm{T,TOB}}$ threshold of the considered trigger, which leads to hardly any influence on the high-

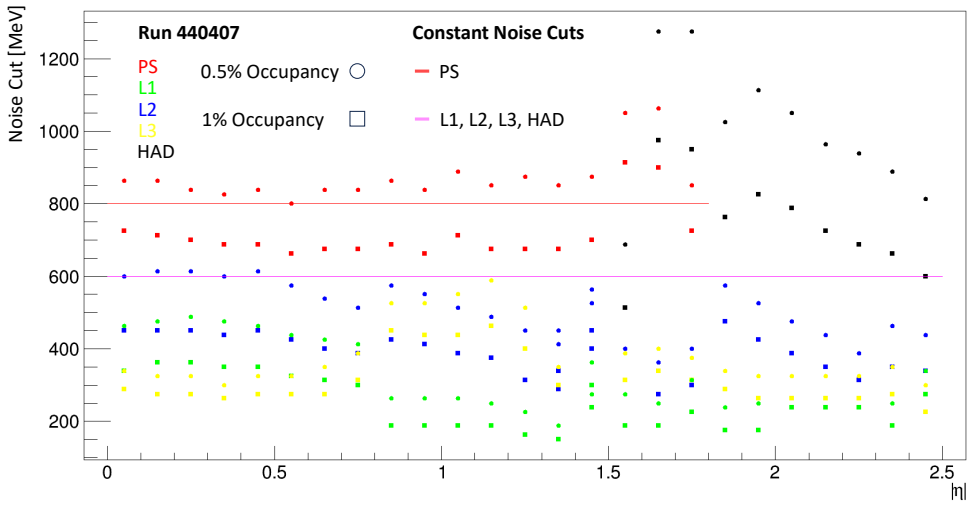

Figure 10.3: Comparison of eFEX noise cuts with constant values and for η- and layer-dependent $0.5\,\%$ and $1\,\%$ cuts. Three different sets of noise cuts of the eFEX system are shown. The constant values were chosen based on experience and previous noise cut studies. The η- and layer-dependent cuts were determined using data from the zero-bias stream of run 440407.

energy L1_eEM26M trigger efficiencies. Furthermore, there was no clear trend for higher or lower noise cuts, so in general the influence seems to balance out over the whole detector. Overall, the efficiencies of the L1_eEM26M trigger remain stable with changes to the noise cuts.

A similar effect can be observed as well in the rate studies, but with slightly higher trigger rates for the η- and layer-dependent noise cuts. For the L1_eEM26M trigger item with optimal parameters, a rate of $21\,\mathrm{kHz}$ is calculated for the constant noise cuts, a rate of $22.4\,\mathrm{kHz}$ for the $0.5\,\%$ occupancy cuts and a rate of $22.2\,\mathrm{kHz}$ for the $1\,\%$ occupancy thresholds. This effect can possibly be attributed to lower energies due to the noise cuts in the electromagnetic isolation environment of the TOBs and the resulting higher number of TOBs passing the isolation criteria.

Finally, the decision was made to use the $0.5\,\%$ occupancy noise cuts for the switch from legacy to Phase-1 EM triggers, since on the one hand the η- and layer-dependent noise cuts better represent the noise structure within the LAr calorimeter. On the other hand, a conservative approach was chosen in order to continue to filter out a large number of noisy SC signals and thus ensure low rates especially for trigger items with lower $E_{\mathrm{T,TOB}}$ thresholds.

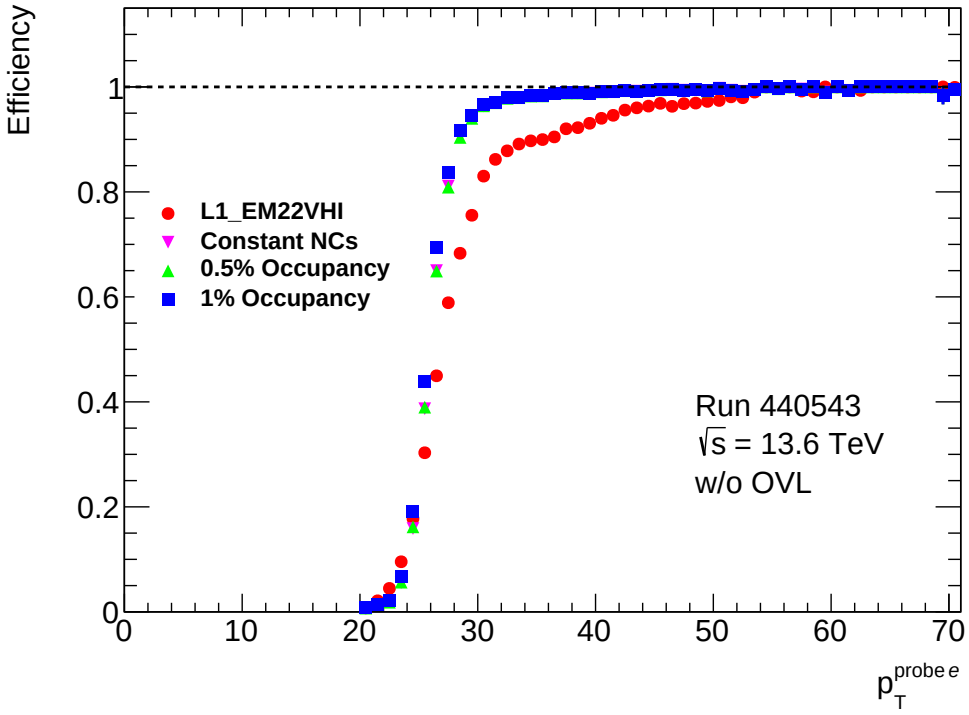

Figure 10.4: Efficiency studies with constant as well as η- and layer-dependent eFEX noise cuts. The efficiencies were obtained for the eFEX system with resimulated TOBs with different noise cuts using the tag-and-probe method and EGZ L1Calo1 DAODs from run 440543. Furthermore, the efficiency of the legacy L1_EM22VHI trigger is shown as a reference. The influence of the noise cuts on the efficiencies is minor and shows only a small change in the turn-on area of the curves.

11 Conclusion

With the start of Run 3 of the LHC and the accompanying harsher operational environment due to increased centre-of-mass energies and instantaneous luminosity, the Level-1 calorimeter trigger underwent a series of upgrades as part of the Phase-1 upgrade to continue delivering excellent performance with high trigger efficiencies at low E_{T} thresholds and Level-1 rates.
Among other things, new Feature Extractor (FEX) systems were introduced for the determination of events of interest. In addition, the Tile Rear Extension (TREX) module as a physical extension of the legacy PreProcessor Module (PPM) is needed to forward signals from the Tile calorimeter to the new FEXes, but also to maintain the functionality of the legacy system and thus ensure parallel operation of both systems. This was exploited to trigger the first data taking period of Run 3 entirely with the legacy system, while the Phase-1 system continued to be tested and commissioned.
Due to the different data taking conditions and various changes to the legacy system, such as the installation of the TREX modules, the legacy system had to be completely recalibrated and recommissioned in order to be optimally prepared for the first data taking period. For this purpose, the combined calibrations with the calorimeters were revived in order to achieve an initial energy calibration at the receiver level of the legacy system. Furthermore, various test runs, such as cosmic runs, splashes, pilot beams or the LHC ramp-up period for Run 3, were used for recommissioning, to calibrate the timing or to find and treat problematic as well as noisy trigger towers.
To ensure correct data taking with the legacy system, the TREX modules integrated into the legacy path also had to pass various tests before installation, such as checks with the specially implemented online simulation. In order to guarantee secure data taking, the TREX module also had to be implemented within the ATLAS Detector Control System (DCS) with a DCS project that was specially created for the TREX. With all these preparations, an optimally configured legacy system was provided, which showed a high performance and finally contributed to a total recorded integrated luminosity of $37.8\,\mathrm{fb}^{-1}$ [98] for the first data taking period of Run 3.
The recorded data were used for several comparisons between the legacy and the Phase-1 system and thus contributed significantly to the commissioning of the FEX systems. The existing software tools for data access and analysis had to be extended with Phase-1 information in order to allow comparisons between inputs, trigger objects (TOBs), trigger efficiencies, and trigger rates of the legacy and Phase-1 systems. Furthermore, parameter

studies of the Electron Feature Extractor (eFEX), which is responsible for the identification of e/γ and τ candidates, were performed to find optimal settings for a possible switch from the legacy to the Phase-1 system. Overall, the eFEX system showed comparable or better trigger efficiencies with lower Level-1 rates in comparisons to the legacy system. These studies ultimately led to the deactivation of the first unprescaled single electron trigger of the legacy system in May 2023 and the corresponding Phase-1 trigger of the eFEX system successfully starting to identify e/γ candidates.

Bibliography

[1] Oliver Sim Brüning, Paul Collier, P Lebrun, Stephen Myers, Ranko Ostojic, John Poole, and Paul Proudlock. *LHC Design Report*. CERN Yellow Reports: Monographs. CERN, Geneva, 2004. doi: 10.5170/CERN-2004-003-V-1. URL https://cds.cern.ch/record/782076.

[2] The ATLAS Collaboration et al. The ATLAS Experiment at the CERN Large Hadron Collider. *Journal of Instrumentation*, 3(08):S08003, aug 2008. doi: 10.1088/1748-0221/3/08/S08003. URL https://dx.doi.org/10.1088/1748-0221/3/08/S08003.

[3] The CMS Collaboration et al. The CMS experiment at the CERN LHC. *Journal of Instrumentation*, 3(08):S08004, aug 2008. doi: 10.1088/1748-0221/3/08/S08004. URL https://dx.doi.org/10.1088/1748-0221/3/08/S08004.

[4] The ALICE Collaboration et al. The ALICE experiment at the CERN LHC. *Journal of Instrumentation*, 3(08):S08002, aug 2008. doi: 10.1088/1748-0221/3/08/S08002. URL https://dx.doi.org/10.1088/1748-0221/3/08/S08002.

[5] The LHCb Collaboration et al. The LHCb Detector at the LHC. *Journal of Instrumentation*, 3(08):S08005, aug 2008. doi: 10.1088/1748-0221/3/08/S08005. URL https://dx.doi.org/10.1088/1748-0221/3/08/S08005.

[6] Maurizio Vretenar et al. *Linac4 design report*, volume 6 of *CERN Yellow Reports: Monographs*. CERN, Geneva, 2020. doi: 10.23731/CYRM-2020-006. URL https://cds.cern.ch/record/2736208.

[7] A Newborough et al. Upgrade of the CERN Proton Synchrotron Booster bending magnets for 2 GeV Operation. *IEEE Trans. Appl. Supercond.*, 24:500304, 2013. doi: 10.1109/TASC.2013.2282263. URL https://cds.cern.ch/record/1662556.

[8] Ewa Lopienska. The CERN accelerator complex, layout in 2022. Complexe des accélérateurs du CERN en janvier 2022. 2022. URL https://cds.cern.ch/record/2800984. General Photo.

[9] Lyndon Evans and Philip Bryant. LHC Machine. *Journal of Instrumentation*, 3 (08):S08001, aug 2008. doi: 10.1088/1748-0221/3/08/S08001. URL https://dx.doi.org/10.1088/1748-0221/3/08/S08001.

[10] Jan Jongmanns. *The Upgrade of the PreProcessor of the ATLAS Level-1 Calorimeter Trigger for LHC Run-2*. Phd thesis, Universität Heidelberg, 2017.

[11] Tigran Mkrtchyan. *Extension of the L1Calo PreProcessor System for the ATLAS Phase-I Calorimeter Trigger Upgrade*. PhD thesis, Universität Heidelberg, 2023.

[12] Werner Herr and B Muratori. Concept of luminosity. 2006. doi: 10.5170/CERN-2006-002.361. URL https://cds.cern.ch/record/941318.

[13] Georges Aad et al. Performance of pile-up mitigation techniques for jets in pp collisions at $\sqrt{s} = 8$ TeV using the ATLAS detector. Performance of pile-up mitigation techniques for jets in pp collisions at $\sqrt{s} = 8$ TeV using the ATLAS detector. *Eur. Phys. J. C*, 76:581, 2016. doi: 10.1140/epjc/s10052-016-4395-z. URL https://cds.cern.ch/record/2058295.

[14] Mike Lamont. The First Years of LHC Operation for Luminosity Production. page MOYAB101, 2013. URL https://cds.cern.ch/record/2010134.

[15] Jorg Wenninger. LHC status and performance. *PoS*, CHARGED2018:001, 2019. doi: 10.22323/1.339.0001. URL http://cds.cern.ch/record/2710042.

[16] Joao Pequenao. Computer generated image of the whole ATLAS detector. 2008. URL https://cds.cern.ch/record/1095924.

[17] *ATLAS inner detector: Technical Design Report, 1*. Technical design report. ATLAS. CERN, Geneva, 1997. URL https://cds.cern.ch/record/331063.

[18] Joao Pequenao. Computer generated image of the ATLAS inner detector. 2008. URL https://cds.cern.ch/record/1095926.

[19] G Aad et al. ATLAS pixel detector electronics and sensors. *JINST*, 3:P07007, 2008. doi: 10.1088/1748-0221/3/07/P07007. URL http://cds.cern.ch/record/1119279.

[20] Alessandro La Rosa and Alessandro La Rosa. The ATLAS Insertable B-Layer: from construction to operation. Technical Report 12, CERN, Geneva, 2016. URL https://cds.cern.ch/record/2221972.

[21] Georges Aad et al. Operation and performance of the ATLAS semiconductor tracker in LHC Run 2. *JINST*, 17:P01013, 2022. doi: 10.1088/1748-0221/17/01/P01013. URL https://cds.cern.ch/record/2780336.

[22] A Vogel. ATLAS Transition Radiation Tracker (TRT): Straw Tube Gaseous Detectors at High Rates. Technical report, CERN, Geneva, 2013. URL https://cds.cern.ch/record/1537991.

[23] G. Aad et. al. The ATLAS Inner Detector commissioning and calibration. The ATLAS Inner Detector commissioning and calibration. *Eur. Phys. J. C*, 70:787–821, 2010. doi: 10.1140/epjc/s10052-010-1366-7. URL https://cds.cern.ch/record/1262789. Comments: 34 pages, 25 figures.

[24] Joao Pequenao. Computer Generated image of the ATLAS calorimeter. 2008. URL https://cds.cern.ch/record/1095927.

[25] *ATLAS liquid-argon calorimeter: Technical Design Report*. Technical design report. ATLAS. CERN, Geneva, 1996. doi: 10.17181/CERN.FWRW.FOOQ. URL https://cds.cern.ch/record/331061.

[26] J del Peso. Design and Performance of the ATLAS LAr Calorimeter. Technical report, CERN, Geneva, 2011. URL http://cds.cern.ch/record/1385899.

[27] *ATLAS tile calorimeter: Technical Design Report*. Technical design report. ATLAS. CERN, Geneva, 1996. doi: 10.17181/CERN.JRBJ.7O28. URL https://cds.cern.ch/record/331062.

[28] T Davidek and (on behalf of the ATLAS Tilecal system). ATLAS Tile Calorimeter performance for single particles in beam tests. *Journal of Physics: Conference Series*, 160(1):012057, apr 2009. doi: 10.1088/1742-6596/160/1/012057. URL https://dx.doi.org/10.1088/1742-6596/160/1/012057.

[29] *ATLAS muon spectrometer: Technical Design Report*. Technical design report. ATLAS. CERN, Geneva, 1997. URL https://cds.cern.ch/record/331068.

[30] Joao Pequenao. Computer generated image of the ATLAS Muons subsystem. 2008. URL https://cds.cern.ch/record/1095929.

[31] P F Åkesson and E Moyse. Event Data Model in ATLAS. 2005. doi: 10.5170/CERN-2005-002.255. URL https://cds.cern.ch/record/865580.

[32] Rafal Bielski and on behalf of the ATLAS Collaboration. ATLAS High Level Trigger within the multi-threaded software framework AthenaMT. *Journal of Physics: Conference Series*, 1525(1):012031, apr 2020. doi: 10.1088/1742-6596/1525/1/012031. URL https://dx.doi.org/10.1088/1742-6596/1525/1/012031.

[33] ATLAS TDAQ Group. ATLAS DAQ Public Results, . URL https://twiki.cern.ch/twiki/bin/view/AtlasPublic/ApprovedPlotsDAQ.

[34] R Achenbach et al. The ATLAS Level-1 Calorimeter Trigger. Technical report, CERN, Geneva, 2008. URL http://cds.cern.ch/record/1080560.

[35] Georges Aad et al. Topological cell clustering in the ATLAS calorimeters and its performance in LHC Run 1. Topological cell clustering in the ATLAS calorimeters and its performance in LHC Run 1. *Eur. Phys. J. C*, 77:490, 2017. doi: 10.1140/epjc/s10052-017-5004-5. URL https://cds.cern.ch/record/2138166. Comments: 64 pages plus author list + cover page (87 pages in total), 41 figures, 3 tables, submitted to EPJC. All figures including auxiliary figures are available at http://atlas.web.cern.ch/Atlas/GROUPS/PHYSICS/PAPERS/PERF-2014-07/.

[36] Georges Aad et al. Technical Design Report for the Phase-I Upgrade of the ATLAS TDAQ System. Technical report, 2013. URL https://cds.cern.ch/record/1602235. Final version presented to December 2013 LHCC.

[37] George Victor Andrei. *The Data Path of the ATLAS Level-1 Calorimeter Trigger Pre-Processor*. PhD thesis, Universität Heidelberg, 2010.

[38] L1Calo Collaboration. Level-1 Calorimeter Trigger: Cable Mappings and Crate Layouts from Analogue Inputs to Processors. Technical report, 2007. URL https://edms.cern.ch/document/399348/2.2.

[39] Martin Wessels. Calibration and Performance of the ATLAS Level-1 Calorimeter Trigger with LHC Collision Data. *Physics Procedia*, 37:1841–1848, 2012. ISSN 1875-3892. doi: https://doi.org/10.1016/j.phpro.2012.02.505. URL https://www.sciencedirect.com/science/article/pii/S1875389212018962. Proceedings of the 2nd International Conference on Technology and Instrumentation in Particle Physics (TIPP 2011).

[40] ATLAS L1Calo Group. Level-1 Calorimeter Trigger: Receiver to PPM Patch Panel Specifications. Technical report, CERN, . URL http://pprc.qmul.ac.uk/l1calo/doc/out/PatchPanels.pdf.

[41] B Åsman et al. The ATLAS Level-1 Calorimeter Trigger: PreProcessor implementation and performance. *Journal of Instrumentation*, 7:P12008, 12 2012. doi: 10.1088/1748-0221/7/12/P12008.

[42] Georges Aad et al. Performance of the upgraded PreProcessor of the ATLAS Level-1 Calorimeter Trigger. *JINST*, 15(11):P11016, 2020. doi: 10.1088/1748-0221/15/11/P11016. URL https://cds.cern.ch/record/2717655. 49 pages in total, author list starting page 33, 19 figures, 1 table, submitted to JINST. All figures including auxiliary figures are available at https://atlas.web.cern.ch/Atlas/GROUPS/PHYSICS/PAPERS/TDAQ-2019-01.

[43] KIP Heidelberg. Tile Rear Extension (TREX) ATLAS TDAQ Phase-I Upgrade-PRR. Technical report, CERN. URL https://edms.cern.ch/ui/file/1533071/0.2/TREX_PRR.pdf.

[44] W.T. Fedorak and P.P. Plucinski. Cmx base function fpga firmware functionality, 2015. URL https://web.pa.msu.edu/hep/atlas/l1calo/cmx/specification/5_firmware_review/CMX_BaseFunction_Firmware_V1p0.pdf.

[45] T Kawamoto, S Vlachos, L Pontecorvo, J Dubbert, G Mikenberg, P Iengo, C Dallapiccola, C Amelung, L Levinson, R Richter, and D Lellouch. New Small Wheel Technical Design Report. Technical report, 2013. URL https://cds.cern.ch/record/1552862. ATLAS New Small Wheel Technical Design Report.

[46] Aaron James Armbruster et al. The ATLAS Muon to Central Trigger Processor Interface Upgrade for the Run 3 of the LHC. Technical report, CERN, Geneva, 2018. URL https://cds.cern.ch/record/2296209.

[47] Georges Aad et al. Performance of the ATLAS Level-1 topological trigger in Run 2. *Eur. Phys. J. C*, 82(1):7, 2022. doi: 10.1140/epjc/s10052-021-09807-0.

[48] Ralf Spiwoks, S Ask, Nick Ellis, P Farthouat, P Gällnö, J Haller, A Krasznahorkay, T Maeno, T Pauly, H Pessoa-Lima, I Resurreccion-Arcas, G Schuler, J M De Seixas, R Torga-Teixeira, and T Wengler. The ATLAS Level-1 Central Trigger Processor (CTP). Technical report, 2005. URL https://cds.cern.ch/record/889547.

[49] Carlo Alberto Gottardo. FELIX and SW ROD Commissioning of the New ATLAS Readout System. Technical report, CERN, Geneva, 2020. URL https://cds.cern.ch/record/2746729.

[50] M (CERN) Aleksa, W (Pittsburgh) Cleland, Y (Tokyo) Enari, M (Victoria) Fincke-Keeler, L (CERN) Hervas, F (BNL) Lanni, S (Oregon) Majewski, C (Victoria) Marino, and I (LAPP) Wingerter-Seez. ATLAS Liquid Argon Calorimeter Phase-I Upgrade: Technical Design Report. Technical report, 2013. URL https://cds.cern.ch/record/1602230. Final version presented to December 2013 LHCC.

[51] Weiming Qian, Francesco Gonnella, and Ian Brawn. Technical Specification ATLAS Level-1 Calorimeter Trigger Upgrade Electromagnetic Feature Extractor (eFEX). Technical report, CERN. URL https://edms.cern.ch/ui/file/1419789/1/eFEX_TechSpec_v0.91.pdf.

[52] Francesco Gonnella. Private Communication, 2023.

[53] Bruno Bauss, Volker Buescher, Reinold Degele, Holger Herr, Christian Kahra, Marek Palka, Stefan Rave, Elena Rocco, Uli Schaefer, Julio Vieira De Souza, Duc Bao Ta, Stefan Tapprogge, Renjie Wang, and Marcel Weirich. Project Specification and Hardware Tests of the jet Feature Extractor (jFEX) in ATLAS Level-1 Calorimeter Trigger for TDAQ Phase-I Upgrade (Report for Production Readiness Review). Technical report, CERN, Geneva, 2019. URL https://cds.cern.ch/record/2687132.

[54] Marcel Weirich. Firmware Algorithms of the jet Feature EXtractor (jFEX) in ATLAS Level-1 Calorimeter Trigger for TDAQ Phase-I Upgrade (Report for Production Readiness Review). Technical report, CERN, Geneva, 2019. URL https://cds.cern.ch/record/2688511.

[55] gFEX Team. Global Feature Extractor (gFEX) of the Level-1 Calorimeter Trigger. Technical report, CERN. URL https://edms.cern.ch/ui/file/1425502/1/ATL-COM-DAQ-2016-184.pdf.

[56] Katharina Bierwagen, Uli Schaefer, and Julio Vieira De Souza. Level-1 Topological Processor (L1Topo) ATLAS TDAQ Phase-I Upgrade - Hardware Specifications. Technical report, CERN, Geneva, 2019. URL https://cds.cern.ch/record/2654109.

[57] Foteini Trantou. A program to drive the ATLAS Local Trigger Interface (ALTI) at the ATLAS experiment. *Journal of Physics: Conference Series*, 2105(1):012024, nov 2021. doi: 10.1088/1742-6596/2105/1/012024. URL https://dx.doi.org/10.1088/1742-6596/2105/1/012024.

[58] Rhys Owen. Private Communication, 2023.

[59] OPC Unified Architecture (UA). https://opcfoundation.org/about/opc-technologies/opc-ua/. Accessed: 2023-07-04.

[60] A Barriuso Poy et al. The detector control system of the ATLAS experiment. *Journal of Instrumentation*, 3(05):P05006, may 2008. doi: 10.1088/1748-0221/3/05/P05006. URL https://dx.doi.org/10.1088/1748-0221/3/05/P05006.

[61] K Lantzsch et al. The ATLAS Detector Control System. *Journal of Physics: Conference Series*, 396(1):012028, dec 2012. doi: 10.1088/1742-6596/396/1/012028. URL https://dx.doi.org/10.1088/1742-6596/396/1/012028.

[62] S Schlenker et al. The ATLAS Detector Control System. *Conf. Proc.*, C111010: MOBAUST02, 2011. URL https://cds.cern.ch/record/1562594.

[63] Christopher J Curtis. Development of the detector control system for the ATLAS Level-1 trigger and measurement of the single top production cross section, 2010. URL https://cds.cern.ch/record/2138392.

[64] Hermann Fuchs. *Development of a temperature monitoring system for the ATLAS muon spectrometer*. 2010.

[65] SIMATIC WinCC Open Architecture Version 3.19 Documentation. https://www.winccoa.com/documentation/WinCCOA/latest/en_US/index.html. Accessed: 2023-06-25.

[66] J Maciejewski and S Schlenker. Visualization of historical data for the atlas detector controls - ddv. *Journal of Physics: Conference Series*, 898(3):032045, oct 2017. doi: 10.1088/1742-6596/898/3/032045. URL https://dx.doi.org/10.1088/1742-6596/898/3/032045.

[67] S. Schlenker A. Barriuso Poy. ATLAS DCS FSM Integration Guideline. Technical report, CERN. URL https://web.pa.msu.edu/hep/atlas/l1calo/hub/reference/dcs/FSM_Integration_Guideline_v3p0_2016_02_01.pdf.

[68] The Quick Opcua Server Generation Framework. https://quasar.docs.cern.ch/. Accessed: 2023-07-04.

[69] Stefan Schlenker, Damian Abalo Miron, Ben Farnham, Viatcheslav Filimonov, Piotr Nikiel, and Cristian-Valeriu Soare. quasar - A Generic Framework for Rapid Development of OPC UA Servers. page WEB3O02, 2015. doi: 10.18429/JACoW-ICALEPCS2015-WEB3O02. URL https://cds.cern.ch/record/2213489.

[70] C. N. P. Gee. Project Specification ATLAS Calorimeter First Level Trigger-Timing Control Module. Technical report, CERN. URL https://web.pa.msu.edu/hep/atlas/l1calo/reference/l1calo/tcm/TCM_V1_0_5.pdf.

[71] R Achenbach et al. Control, Test and Monitoring Software Framework for the ATLAS Level-1 Calorimeter Trigger. 2008. doi: 10.5170/CERN-2008-008.441. URL https://cds.cern.ch/record/1138902. this note was endorsed by the TDAQ project leader.

[72] Murrough Landon. L1Calo Database User Guide. Technical report, CERN, . URL http://pprc.qmul.ac.uk/l1calo/doc/out/DatabaseUserGuide.pdf.

[73] Murrough Landon. Configuration Database. Technical report, CERN, . URL http://pprc.qmul.ac.uk/l1calo/doc/out/ConfigDatabase.pdf.

[74] Murrough Landon. HDMC Changes. Technical report, CERN, . URL http://pprc.qmul.ac.uk/l1calo/doc/out/HdmcChanges.pdf.

[75] C. Larrea, K. Harder, D. Newbold, D. Sankey, Andrew Rose, Alessandro Thea, and Tw Williams. IPbus: a flexible Ethernet-based control system for xTCA hardware. *Journal of Instrumentation*, 10:C02019–C02019, 02 2015. doi: 10.1088/1748-0221/10/02/C02019.

[76] D Liko, Doris Burckhart-Chromek, J Flammer, M Dobson, R Jones, L Mapelli, I Alexandrov, S Korobov, V Kotov, M Mineev, A Amorim, N Fiuza de Barros, D Klose, L Pedro, E Badescu, M Caprini, S Kolos, A Kazarov, Yu Ryabov, and I Soloviev. Control in the ATLAS TDAQ System. Technical report, CERN, Geneva, 2005. URL https://cds.cern.ch/record/795915.

[77] ATLAS L1Calo Group. Overview of the Simulation Framework. Technical report, CERN, . URL http://pprc.qmul.ac.uk/l1calo/doc/out/Simulation.pdf.

[78] Adrian Mirea. ATLAS Online L1 Calorimeter Trigger Monitoring Framework. Technical report, CERN. URL http://pprc.qmul.ac.uk/l1calo/doc/pdf/MonitoringFramework.pdf.

[79] Murrough Landon. Calibration and Setup Procedures. Technical report, CERN, . URL http://pprc.qmul.ac.uk/l1calo/doc/out/Calibration.pdf.

[80] *ATLAS Computing: technical design report*. Technical design report. ATLAS. CERN, Geneva, 2005. URL https://cds.cern.ch/record/837738.

[81] The German ATLAS Groups. ATLAS Requirements for the National Analysis Facility. https://confluence.desy.de/download/attachments/107067545/A-NAF.pdf?version=1&modificationDate=1541420074310&api=v2. Accessed: 2023-07-20.

[82] ATLAS L1Calo Group. ATLAS Level-1 Calorimeter Trigger Public Results, . URL https://twiki.cern.ch/twiki/bin/view/AtlasPublic/L1CaloTriggerPublicResults.

[83] Florian Föhlisch. *Calibration for the ATLAS Level-1 Calorimeter-Trigger*. Phd thesis, Universität Heidelberg, 2007.

[84] B Åsman et al. The ATLAS Level-1 Calorimeter Trigger: PreProcessor implementation and performance. *Journal of Instrumentation*, 7(12):P12008, dec 2012. doi: 10.1088/1748-0221/7/12/P12008. URL https://dx.doi.org/10.1088/1748-0221/7/12/P12008.

[85] V Lang and R Stamen. Precision Synchronization of the ATLAS Level-1 Calorimeter Trigger with Collision Data in 2010 and 2011. Technical report, CERN, Geneva, 2012. URL https://cds.cern.ch/record/1454684.

[86] The ATLAS collaboration. Operation of the ATLAS trigger system in Run 2. *Journal of Instrumentation*, 15(10):P10004, oct 2020. doi: 10.1088/1748-0221/15/10/P10004. URL https://dx.doi.org/10.1088/1748-0221/15/10/P10004.

[87] G. Aad et al. ATLAS data quality operations and performance for 2015–2018 data-taking. *Journal of Instrumentation*, 15(04):P04003, apr 2020. doi: 10.1088/1748-0221/15/04/P04003. URL https://dx.doi.org/10.1088/1748-0221/15/04/P04003.

[88] Humphry Tlou and Bruce Mellado. Integration of the ALTI module in the ATLAS Tile Calorimeter system. Technical report, CERN. URL http://saip.org.za/Proceedings/Track%20F/81.pdf.

[89] Humphry Tlou. Integration and Commissioning of the ATLAS Tile Demonstrator Module for Run 3. Technical Report 11, CERN, Geneva, 2022. URL https://cds.cern.ch/record/2837280.

[90] Thomas Junkermann. Private Communication, 2023.

[91] Georges Aad, Alessandra Camplani, Nicolas Chevillot, Bernard Dinkespiler, Nicolas Dumont Dayot, Yuji Enari, Rainer Guenter Hentges, Kenneth Johns, Isabelle Wingerter-Seez, and Vladimir Zhulanov. ATLAS LAr Calorimeter trigger electronics phase I upgrade: LATOME Firmware Specifications. Technical report, CERN, Geneva, 2017. URL https://cds.cern.ch/record/2294187.

[92] M. Aaboud et al. Electron efficiency measurements with the ATLAS detector using 2012 LHC proton–proton collision data. *The European Physical Journal C*, 77(3), mar 2017. doi: 10.1140/epjc/s10052-017-4756-2. URL https://doi.org/10.1140%2Fepjc%2Fs10052-017-4756-2.

[93] M. Aaboud et al. Electron reconstruction and identification in the ATLAS experiment using the 2015 and 2016 LHC proton-proton collision data at $\sqrt{s} = 13$ TeV. *Eur. Phys. J. C*, 79(8):639, 2019. doi: 10.1140/epjc/s10052-019-7140-6. URL https://cds.cern.ch/record/2657964. 63 pages in total, author list starting page 47, 16 figures, 4 tables, final version published in EPJC. All figures including auxiliary figures are available at https://atlas.web.cern.ch/Atlas/GROUPS/PHYSICS/PAPERS/PERF-2017-01.

[94] ATLAS EGamma Group. Run3 Pre-Recommendation EGammaRecommendationsR22. https://twiki.cern.ch/twiki/bin/view/AtlasProtected/EGammaRecommendationsR22, . Accessed: 2023-09-24.

[95] ATLAS Inner Tracking Combined Performance Group. Impact parameters (z0, d0) definition and recommended usage. https://twiki.cern.ch/twiki/bin/view/AtlasProtected/InDetTrackingDC14#Impact_parameters_z0_d0_definiti, . Accessed: 2023-09-24.

[96] Torbjorn Sjostrand. Monte Carlo Generators. pages 51–74, 2007. doi: 10.5170/CERN-2007-005.51. URL https://cds.cern.ch/record/999717.

[97] Andrew Haas and on behalf of the ATLAS Collaboration. ATLAS Simulation using Real Data: Embedding and Overlay. *Journal of Physics: Conference Series*, 898 (4):042004, oct 2017. doi: 10.1088/1742-6596/898/4/042004. URL https://dx.doi.org/10.1088/1742-6596/898/4/042004.

[98] ATLAS. Internal Communication, 2022.

Acknowledgements

First of all, I would like to thank Prof. Dr. Hans-Christian Schultz-Coulon, who made it possible for me to do my PhD within the ATLAS collaboration at the Kirchhoff Institute for Physics in Heidelberg and gave me the opportunity to live and work in an incredible environment at CERN for almost 2 years.
Furthermore, I would like to thank Prof. Dr. Loredana Gastaldo, who agreed to read and evaluate my thesis as a second referee.
A special thank you goes to Martin Wessels, who supervised me during my PhD, always had an open ear for me, and was my contact in so many situations with his detailed knowledge of the L1Calo system.
During my time at CERN, I was able to gain incredible experience as part of the L1Calo team, to whom I would like to express my gratitude. I would especially like to thank Silvia Franchino and Rhys Owen, with whom I spent a lot of time in USA15, in our test rigs, and in our many test sessions in the control room. During this time I was able to learn so much, thank you.
I would like to thank the eFEX team for welcoming me and supporting me in my analyses. I would especially like to thank Stephen Hillier, Paul Thompson, and Juraj Bracinik.
Many thanks to all those who proofread my thesis, including Rainer Stamen, Martin Wessels, Tigran Mkrtchyan, Sebastian Weber, Philipp Ott, Thomas Junkermann, Lisa Baltes, Anke Ackermann, and Varsiha Sothilingam.
I would like to thank everyone in F8 and F11 who made my PhD time an unforgettable experience outside of working hours, be it with various activities, but also during several conferences and the sometimes all-night evenings associated with them.
Thanks to Petra Pfeifer, who supported me in all administrative questions, but also gave me advice apart from that. I will miss our chats, thank you for everything.
At the end, I would like to thank my loved ones. Firstly, my whole family, who have supported me throughout my entire journey. You always stood by me in ups and downs, and I am infinitely grateful for that.
Finally, I would like to thank my girlfriend Ha Mi. We met at the beginning of my PhD and you have completely accompanied me through this beautiful but also sometimes challenging experience. You always gave me the support I needed to get through difficult phases, like the CERN time during Corona, but also my moods while writing my thesis. I am so excited about our future with our little family. Thank you!